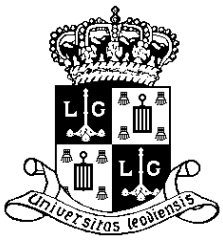

UNIVERSITÉ DE LIÈGE
Faculté des Sciences Appliquées

Source estimation in EEG

Combining anatomical and functional constraints

Thèse présentée par
Christophe L.M. Phillips
en vue de l'obtention du grade
de Docteur en Sciences Appliquées

Année Académique 2000–2001

Contents

List of Figures

List of Tables

Acknowledgements - Remerciements

Tout d'abord, je tiens à remercier le Professeur François-Xavier Litt et Monsieur André Luxen de m'avoir permis de réaliser cette thèse de doctorat dans les meilleures conditions. Je dois beaucoup au Docteur Pierre Maquet qui m'a entrainé sur la voie de la neuro-imagerie fonctionnelle. Ses idées, encouragements et conseils ont été d'une influence primordiale tout au long de ces quatre dernières années. Un grand merci aussi au personnel administratif, médical et chimique du Centre de Recherches du Cyclotron, et plus particulièrement à Christian Degueldre, Philippe Peigneux et Steve Laureys pour les nombreux et enrichissants échanges d'idées, ainsi qu'aux mémorants et doctorants chimistes pour l'ambiance avant, pendant et après les (longues) pauses de midi.

I should particularly thank Professors Karl Friston and Michael Rugg for accepting me as an Honorary Researcher at the Wellcome Department of Cognitive Neurology and the Institute of Cognitive Neuroscience of the University College London. My stay in London would not have been so successful and fulfilling without their support, guidance and encouragement. I owe a great deal of gratitude to a number of friends and colleagues at the WDoCN and ICN, particularly from the Methods Group and the Cognitive Electrophysiology Group. Those especially deserving of a mention include John Ashburner, Stefan Kiebel, Chloe Hutton and Jesper Andersson. I have learned a great deal from all of them, during the Method Meetings and our discussions at work, on the tube or at the pub – and from their books and papers that I was regularly borrowing.

Ma reconnaissance va enfin à mes parents, ma soeur et son mari, ma famille et mes amis qui m'ont fidèlement soutenu, réconforté et aidé en toute circonstance.

Cette thèse et mon séjour à Londres n'auraient pas été possibles sans le support financier de l'Université de Liège, la Communauté Française de Belgique, le Lions Club Liège Airport et le Wellcome Trust.

Chapter 1

Introduction

Contents

1.1 Motivation and aims

The aim of functional neuroimaging is to understand the functional organization of the brain. This aim incorporates several aspects of functional neuroanatomy : the location of processing areas, the time course or dynamics of their activities, and the nature of their interactions. Changes in neuronal activity induce variations in cerebral metabolism, blood flow, blood volume and blood oxygenation (Frackowiak *et al.*, 1997), and electromagnetic fields (Nunez, 1981; Hämäläinen *et al.*, 1993; Malmivuo & Plonsey, 1995). Changes in these hæmodynamic and electromagnetic signals can be measured by several noninvasive techniques, such as positron emission tomography (PET), functional magnetic resonance imaging (fMRI), electroencephalography (EEG) and magnetoencephalography (MEG).

Hæmodynamic responses in the brain are recorded by PET and fMRI with a good spatial resolution, of the order of millimetres. These indices of neuronal activity are temporally limited by the latency and slow time-constants of the hæmodynamic response of the vessels. One standard and popular way of analysing the cerebral metabolism images obtained by fMRI or PET is to treat these three-dimensional images with a voxel based approach to detect the area of (de-)activation between experimental conditions : In brief, images are spatially normalised into a standard space (Talairach & Tournoux, 1988; Friston *et al.*, 1995a; Ashburner & Friston, 1999), and smoothed. Parametric statistical models are assumed at each voxel, using the General Linear Model to describe the variability in the data in terms of experimental and confounding effects, and residual variability (Friston *et al.*, 1995b). Hypotheses expressed in terms of the model parameters are assessed at each voxel with univariate statistics. This gives an image whose voxel values are statistics, a Statistic Image, or Statistical Parametric Map (SPM_t, SPM_Z, SPM_F). Temporal

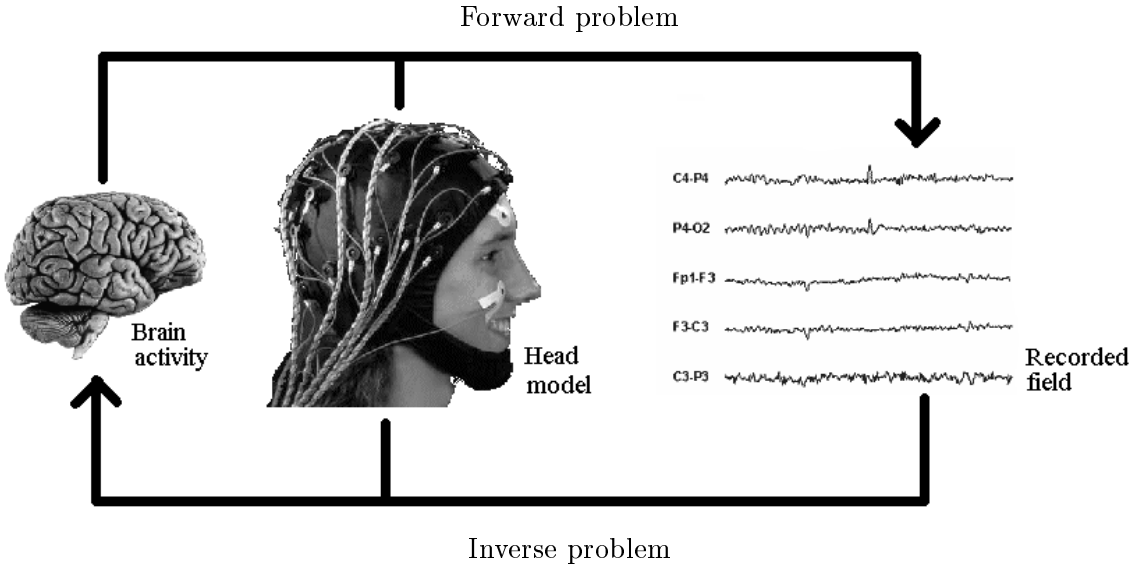

Figure 1.1: Forward problem: determine the electromagnetic field at the scalp from the known sources and volume conductor. Inverse problem: determine the sources from the known electromagnetic field at the scalp and volume conductor. (Picture taken and adapted from Neurosoft, Inc: http://www.neuro.com)

convolution of the General Linear Model for fMRI enables the application of results from serially correlated regression, permitting the construction of statistic images from fMRI time series[1] (Friston & Worsley, 1995).

By contrast, direct measurements of the electromagnetic field (EEG and MEG) produced by neuronal activity have a temporal resolution of less than 1 millisecond. But noninvasive measurements of the electromagnetic field can only be obtained from a limited number of sensors on the scalp. Event-related potentials (ERPs) are voltage fluctuations that are associated in time with some physical or mental occurrence. These potentials can be extracted from the ongoing EEG by means of filtering and averaging. The time series of ERP EEG (or MEG) measurements are statistically compared between conditions: the difference between conditions can be observed spatially, the field pattern on the scalp is modified in amplitude or shape, and/or temporally, the latency of the field pattern relative to the trigger onset is modified (Rugg & Coles, 1995; Picton *et al.*, 2000).

The **Forward Problem** consists in determining the electromagentic field at the scalp from a known source configuration and volume conductor. The **Inverse Problem** describes the opposite situation: given the volume conductor and the electromagnetic field at the scalp, the location and time course of the sources is sought. The Forward Problem and Inverse Problem are illustrated in figure 1.1. In order to solve the Inverse Problem, the solution of the Forward Problem, even if approximate, must be known.

[1] The multiple comparisons problem of simultaneously assessing all the voxel statistics is addressed using the theory of continuous random fields, assuming the statistic image to be a good lattice representation of an underlying continuous stationary random field. Results for the Euler characteristic lead to corrected p-values for each voxel hypothesis (Worsley, 1994). In addition, the theory permits the computation of corrected p-values for clusters of voxels exceeding a given threshold, and for entire sets of supra-threshold clusters, leading to more powerful statistical tests at the expense of some localising power.

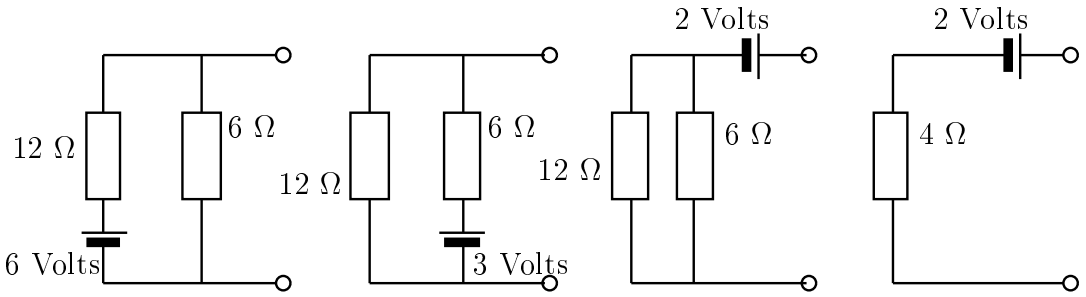

Figure 1.2: Lack of uniqueness in the inverse problem : In this simple model the source is represented by a single battery, and the conductor volume by one or two resistors. The four networks have the same Thevenin equivalent : an electromagnetic force of 2 Volts in series with a resistance of 4 Ω. Therefore one cannot distinguish among these different inverse candidates without measurements within the source region itself, or with prior information on the shape of the network. (Figure taken from Malmivuo & Plonsey (1995).)

The Forward Problem is a "simple electromagnetic problem" that can be expressed and solved with Maxwell's equations. Its difficulty lies in modelling the volume conductor, a human head, and the sources, the neuronal activity of the brain. It is thus necessary to understand cerebral anatomy and the nature of neuronal activity to solve the Forward Problem. Once the relationship between brain electrical activity and electromagnetic scalp fields has been established, the Inverse problem can be approached. Non-invasive measurements of the electromagnetic field can only be obtained from a limited number of sensors on the scalp, and therefore the spatial configuration of neuronal activity **cannot** be determined uniquely if based on EEG and/or MEG recordings alone (Nunez, 1981). The first theoretical paper, which stated that the inverse problem does not have a unique solution, was written by von Helmholtz (1853). The lack of uniqueness in the inverse problem is illustrated by a simple example in figure 1.2 : In this simple model the source is represented by a single battery, and the conductor volume by one or two resistors. The four networks have the same Thevenin equivalent : an electromagnetic force of 2 Volts in series with a resistance of 4 Ω. In order to make the inverse problem well posed, it is thus necessary to impose additional constraints on the solution.

1.1.1 Forward Problem

The brain consists of two hemispheres separated by the longitudinal fissure. The hemispheres are further divided into lobes by two deep fissures : the Rolandic fissure cuts vertically the outer part of both hemispheres and the Sylvian fissure is almost horizontal. There are four lobes in each half of the cortex : frontal, parietal, temporal and occipital, as depicted in figure 1.3. Each lobe assumes specific functions. The total surface of the cortex is about 1600 cm^2, highly folded (convoluted) to fit in the skull compartment.

The neurones and glial cells are the principal "building blocks" of the brain. There are about $10^{10} - 10^{11}$ neurones in the brain, and they are vastly outnumbered by the glial cells. The glial cells ensure the physical structure of the brain, the proper concentration of ions and the transport of the nutrients between blood vessels and brain tissue. Neurons are the

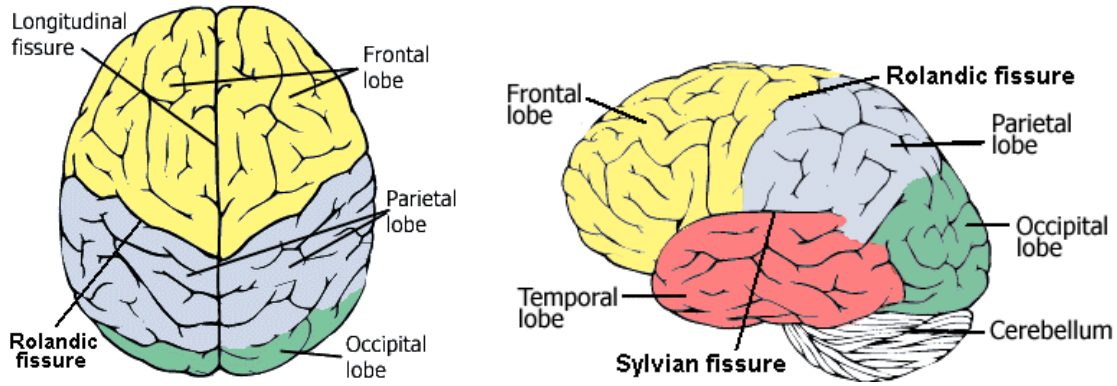

Figure 1.3: The brain consists of two hemispheres separated by the longitudinal fissure. The hemispheres are further divided into lobes by two deep fissures : the Rolandic fissure cuts vertically the outer part of both hemispheres and the Sylvian fissure is almost horizontal. There are four lobes in each half of the cortex : frontal, parietal, temporal and occipital. (Pictures taken from AMA Health Insight : http://www.ama-assn.org)

information-processing units of the brain. The cell bodies and dendrites of the neurones are found in the grey matter, which constitutes the thin outer layer of the cortex and the subcortical structures like the thalamus. The interior of the brain is largely occupied by nerve fibres, called white matter because of the mylenated appearance of the axons that constitute it, see figure 1.4. These axons connect different cortical areas, possibly in different hemispheres, and between the cortex and the subcortical structures. The study of the electrical activity of the brain depends strongly on cortical anatomy :

- cellular-level structures determine how neuronal electrical activity produces macroscopic current sources detectable outside the head;
- the local electrical conductivity influences the solution of the forward problem;
- the anatomy of the brain at the sulcal level can be used in the constraint of the inverse problem solution.

The general structure of the head is rather complicated. The brain is surrounded by thin membranes and it contains ventricles filled with cerebro-spinal fluid. The skull, scalp and other parts of the head (eyes, vessels, nerves, etc) present various types of tissues and cavities of different electrical conductivity, as can be seen in figure 1.4. Moreover the electrical conductivity of brain tissue is highly anisotropic : conduction is 10 times better along an axon fibre than in the transverse direction (Malmivuo & Plonsey, 1995). These complications are generally ignored as, at the present time, it is impossible to measure accurately *in vivo* the details of the conductivity and to take them properly into account in the solution of the forward problem (Marin *et al.*, 1998; Huiskamp *et al.*, 1999). The head is thus usually modelled as a set of concentric homogeneous volume conductors : the brain (comprising the white and grey matter), the skull and the scalp. Sometimes a fourth volume, the cerebro-spinal fluid layer, is added in the model between the brain and skull volume.

A neurone can be divided into three main parts, as shown in figure 1.5 : the cell body

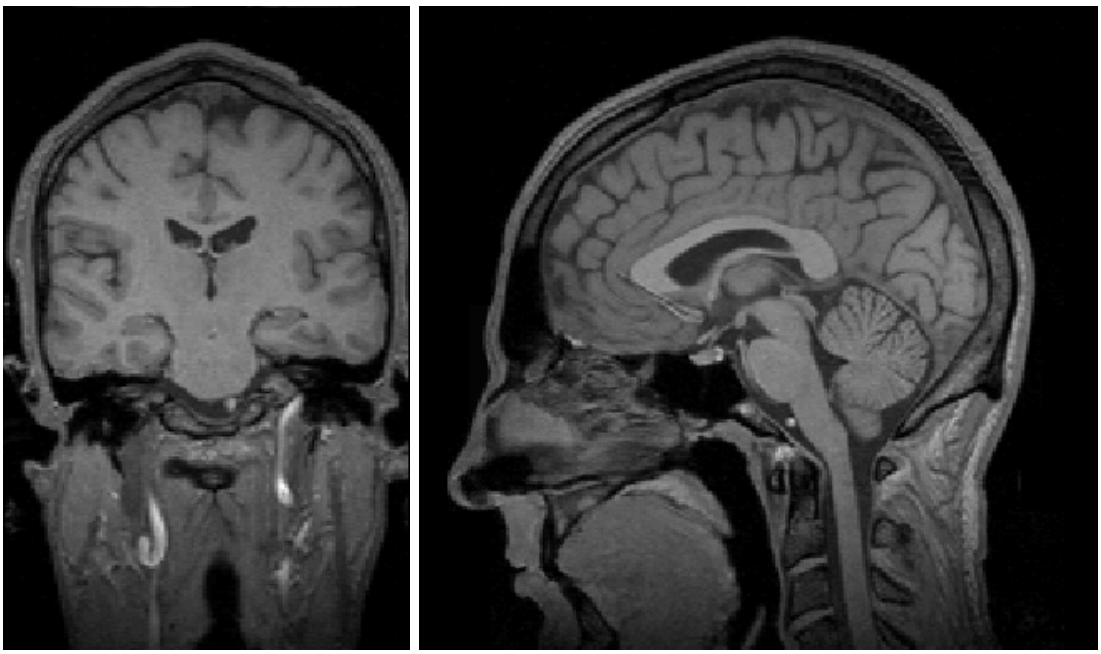

Figure 1.4: Coronal (left) section, at the level of the ears, and sagital (right) section, near the head midline, of my T1 weighted MR image. The grey-white matter distinction is clearly visible on the coronal section. The complexity of the head anatomy is evident on the sagital section.

(or soma), containing the nucleus, is the "processor"; the dendrites, threadlike extensions receiving stimuli from other neurones, are the "receivers"; the axon, a single long fibre carrying the impulse from the soma to other cells, is the "transmitter". In the grey matter, the neurones are organised in layers. Three principal types of neurones are found in the cortex : stellate, spindle and pyramidal cells. The later are important for the scalp electrophysiology because their apical dendrites run parallel to each other through the layers. Since the geometry of neurones dictates the orientation of the current flow, the resulting electrical current flowing through those regularly organised dendrites is perpendicular to the cortical sheet of grey matter. The dendrites and the soma have typically thousands of synapses (connections) from other neurones, forming a hugely complicated network.

At rest, the inside of the cell is negatively polarised relative to the outside, with an intracellular potential of about -70mV. When an action potential (AP) travels along the axon of the presynaptic cell and reaches a synaptic terminal, transmitter molecules are liberated from the synapse into the synaptic gap. These molecules attach themselves to receptors of the postsynaptic cell, opening specific ion channels through the membrane[2]. The resulting flow of ions (mainly Na^+, K^+ and Cl^-) changes the membrane potential in the postsynaptic cell. This event gives rise to the postsynaptic potential, or PSP.

The PSP is said to be excitatory (EPSP) if the cellular membrane is depolarised (the intracellular potential becomes less negative), or inhibitory (IPSP) if the membrane is hyperpolarised (the intracellular potential becomes more negative). Excitatory synapses

[2]The active behavior of the membrane is modelled by Hodgkin-Huxley equations (Malmivuo & Plonsey, 1995, chap. 4).

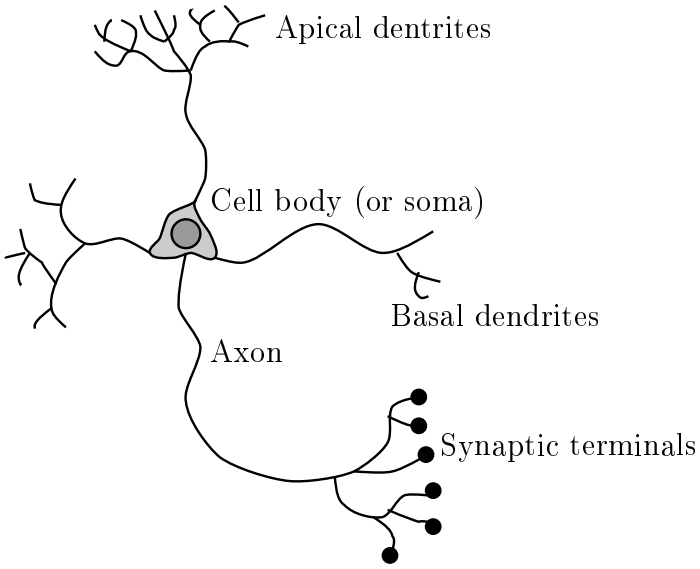

Figure 1.5: A neurone and its three principal parts: the cell body (or soma), containing the nucleus, is the "processor"; the dendrites, threadlike extensions receiving stimuli from other neurones, are the "receivers"; the axon, a single long fibre carrying the impulse from the soma to other cells, is the "transmitter".

are generally located on the dendrites, while the inhibitory synapses are often attached to the soma itself. When the intracellular potential reaches some threshold (typically around -40mV), the neurone fires an action potential. When the excitatory input becomes stronger, the amplitude of the action potential remains the same but the frequency of firing increases.

When an AP reaches a synapse and generates a PSP, the ions flow causes an electric field and a current along the interior of the postsynaptic cell. The strength of this current source decreases with the distance from the synapse but, from far away, it is perceived as a current dipole oriented along the dendrite. On the contrary, the AP travels along the axon with unattenuated amplitude because of active exchanges of ions through the axon membrane. The moving AP can be approximated by two oppositely oriented current dipoles, which is equivalent to a quadrupole. The three main differences between PSP and AP are: 1. their amplitude, an AP is approximately 10 times larger than a PSP, 2. their time course, 10-20 ms for a PSP and only about 1 ms for an AP (see figure 1.6), and 3. their equivalent current source model, a dipole for a PSP and a quadrupole for an AP.

The current source and electromagnetic field generated by a single PSP or AP is obviously not strong enough to be detected on the scalp. The electrodes used in scalp EEG are large (a few millimetres in diameter) and remote, they can only detect summed activities of a large number of neurones. The electromagnetic field generated by a dipolar source (like a PSP) decreases with distance approximately as $1/r^2$, more slowly than the $1/r^3$-dependent field of a quadrupolar source (like an AP). In order to be detectable, the neural activity must sum up efficiently, thus the time course of the current sources must be overlapping. Because of their very short time course, synchronous firing of APs is unlikely but the long time course of PSP allows them to superpose temporally. Therefore, even though APs are much larger in amplitude than PSPs, it is accepted that the PSP are the

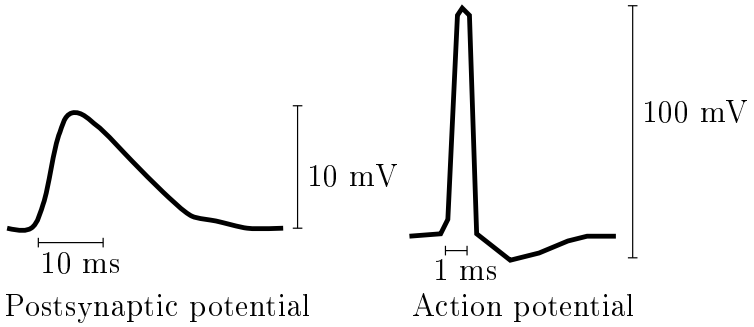

Figure 1.6: A postsynaptic potential (PSP), left, and an action potential (AP), right, as a function of time. There a three major differences between a PSP and an AP : 1. The amplitude of an AP is about 10 times larger than a PSP. 2. A PSP last about 10-20 ms, and an AP only about 1 ms. 3. A PSP can be modelled by a dipolar current source, and an AP by a quadrupolar current source.

generators of scalp fields usually recorded in EEG and MEG (Hämäläinen *et al.*, 1993). If the dendrites supporting PSPs are randomly oriented or radially oriented on a complete spherical surface (or small closed surface), no net electromagnetic field can be detected outside the immediate vicinity of the active neurones, this is called a "closed field" configuration. Because of the uniform spatial organisation of their dendrites (perpendicular to the cortical surface), the pyramidal cells are the only neurones that can generate a net current dipole over a piece of cortical surface, whose field is detectable on the scalp. This is named an "open field" configuration. These conditions of coherence, in space and time, of the neuronal activity imply that the subcortical grey matter nuclei may not be generating any net signal outside the head.

1.1.2 Inverse Problem

One common approach to solving the Inverse Problem is to consider that the EEG/MEG signals are generated by a relatively small number of focal sources (Miltner *et al.*, 1994; Scherg & Ebersole, 1994; Huang *et al.*, 1998; Scherg *et al.*, 1999; Aine *et al.*, 2000), each of which can be modelled as a single fixed or re-orientating dipole. The idea is to render the inverse problem overdetermined by considering fewer unknown parameters than the independent measurements available. The locations, orientations, and strengths of these "equivalent current dipoles" (ECD), six parameters in all, can be estimated by minimising the difference between the predicted and actual EEG/MEG measurements. An additional constraint can be derived from the assumption that the sources are temporally independent (Mosher *et al.*, 1992). The fitting procedure involves a multidimensional, non linear optimisation procedure. As the time required to solve the optimisation problem grows exponentially with the number of ECDs, the global optimum can be found only for models involving very few ECDs. For models with a large number of ECDs, approximate techniques have to be used, where the solution depends upon the initial estimate of the dipoles locations and orientations. In all ECD-based methods, the solution depends **heavily** on the number of dipoles assumed but, in general, the actual number of ECD cannot be determined *a priori*.

Another approach is to consider *a priori* all possible fixed source locations. The problem of determining the strength of each dipole (or dipole components: orientation and strength) then becomes a linear one. This continuous current source model is more biologically plausible (for sufficiently dense source distributions) than the ECD model. But, because the number of possible source locations considered simultaneously is, in general, much larger than the number of sensors, this is an underdetermined problem. In order to ensure the uniqueness and stability of the solution, constraints must be applied. For example, existing methods use one of the following constraints: probabilistic (Greenblatt, 1993; Baillet & Garnero, 1997; Baillet, 1998), maximum entropy (Huang *et al.*, 1997), minimum L1-norm (Uutela *et al.*, 1999), (weighted) minimum L2-norm (Sarvas, 1987; Hämäläinen & Ilmoniemi, 1994; Brooks *et al.*, 1999), maximum smoothness ("Loreta", i.e. "low resolution electromagnetic tomography") (Pascual-Marqui *et al.*, 1994; Pascual-Marqui, 1995, 1999), optimal resolution (Backus & Gilbert, 1970; Grave de Peralta Menendez *et al.*, 1997; Grave de Peralta Menendez & Gonzalez Andino, 1999). Although mathematically convenient, not all the above constraints are based on actual brain physiology and anatomy, and thus can lead to relatively poor spatial resolution or biased solutions.

The weighted minimum L2-norm (WMN) constraint has one great advantage: the method provides a linear analytical solution that can be easily and directly computed. In this thesis I introduce an approach based on the WMN method that imposes constraints using anatomical and physiological information derived from other imaging modalities. Three assumptions, based on neuroanatomy, can be made about the sources of brain electromagnetic activity (Nunez, 1981; Hämäläinen *et al.*, 1993; Dale & Sereno, 1993): the sources are located in grey matter; they are oriented orthogonally to the cortical sheet; and, for a sufficiently dense dipole distribution, they possess locally coherent activity (or smooth activity along the cortical sheet). Further constraints can be introduced in the weighting of the WMN solution by making use of information derived from hæmodynamic measures of brain activity (Rugg, 1998; Liu *et al.*, 1998; Dale *et al.*, 2000). These constraints are predicated on the hypothesis that the synaptic currents generating the EEG/MEG signals also impose metabolic demands, which lead to a hæmodynamic response measurable by PET or fMRI. There are however reasons to consider that the coupling between electromagnetic (EEG/MEG) and hæmodynamic (PET/fMRI) signals is not necessarily well behaved or deterministic (Rugg, 1999), and therefore the prior location information derived from hæmodynamic measurements should be regarded as probabilistically.

Although the methods described in this thesis apply to both electroencephalographic (EEG) and magnetoencephalographic (MEG) data, only EEG data will be used to illustrate the approach in this work. The results obtained are directly and easily transferable to MEG data. When both EEG and MEG data are available simultaneously, they should be used simultaneously to solve the source localisation problem (Fuchs *et al.*, 1998; Baillet *et al.*, 1999) as the two kinds of data contain complementary information.

1.2 Overview of chapters

The thesis is divided into two main parts: firstly, the solution of the Forward Problem and secondly, the solution of the Inverse Problem. The first part of the thesis is a general and extensive introduction to the Forward Problem as solved by the Boundary Element Method (BEM). This problem has been studied, solved and the results applied in differ-

ent fields of science, e.g. electrical engineering and geology, for more than a century, but it only recently has been applied in domains such as EEG, MEG, electro- and magnetocardiography (ECG and MCG) or "transcranial magnetic stimulation" (TMS). Apart from some minor technical details, there is no major original contribution to the source localisation problem in chapters 2, 3 and 4.

Within the first part of the thesis, the Boundary Element Method (BEM) is presented in chapter 2. The BEM equation is an integral form of Maxwell's equations, obtained using Green's theorem (presented in appendix A). In order to obtain the analytical BEM equation, two main assumptions are made about the electric activity of the brain and the conductivity of the head: first, a quasistatic approximation of Maxwell's equations is adopted and, secondly, the head volume is divided into sub-volumes of homogeneous and isotropic conductivity. The BEM allows the estimation of the electric potential only on the surfaces separating those sub-volumes.

The BEM equation can be analytically solved for particular layouts, such as concentric spheres, e.g. the three sphere shell model as presented in appendix B. In order to solve the BEM equation for irregular surfaces, i.e. for a realistic head model, a general but numerically approximate solution is introduced in chapter 3. The surfaces on which the potential is computed are tessellated into flat triangles and the sources of the brain electric activity are modelled by current dipoles. On each flat triangle, the potential is then approximated by a simple function: a constant or linear function evaluated at the centre of gravity or the vertices of the triangle. With these potential approximations, the BEM equation can be rewritten in a matrix form. As non-invasive EEG measurements can only be obtained from a limited number of electrodes on the scalp, the matrix BEM equation is only partially solved using standard algebra techniques.

In chapter 4, the validity of the numerical solution of the BEM equation is assessed by comparing both analytical and numerical solutions of the BEM equation in a three sphere shell model. The two solutions are compared for different approximations of the potential over the triangles and various densities of triangles on the three surfaces. The simulations showed that a linear approximation of the potential over each triangle should be preferred, as well as a denser meshing of the inner surface, i.e. the interface between the brain and skull volume. The best set of parameters is then applied onto a realistic head model obtained from a MR image to generate the "lead field" between the 61 approximately equidistant electrodes on the scalp surface and the 12300 dipoles spread inside the brain volume. This "lead field", the approximate solution of the Forward Problem for the head and source model chosen, will be used in the second part of the thesis.

The second part of the thesis is dedicated to the solution of the Inverse Problem. The general and theoretical approach to the constrained solution is introduced in chapter 5. Spatial constraints on the sources – location, orientation and coherence – are used to reduce the solution space *a priori* by modelling the spatial source distribution with a set of **spatial** basis functions. These spatial basis functions are chosen in a principled way using information theory. Similarly, temporal constraints – window of activity and temporal coherence –, are used to generate a set of **temporal** basis functions. The reduced problem is then solved with a classical WMN method; the solution using basis functions sets being named the "Informed Basis Functions" (IBF) solution. When the IBF solution is calculated, other "soft" constraints ("soft" in the sense that only "hard" anatomical constraints are used to *a priori* restrict the solution space) can be included to

further influence the source reconstruction. When noise is contained in the data, noise-regularisation is necessary to carefully balance, through an hyperparameter λ, the influence of the model versus the priors according to the level of noise. An iterative but systematic procedure, "Restricted Maximum Likelihood" solution (ReML solution), is presented. This "Expectation-Maximisation" (EM) algorithm allows the joint estimations of the solution of the problem and the hyperparameter (controlling the influence of the noise) that determines this solution.

In chapter 6, the approach proposed in the previous chapter is applied with a realistic head model, extracted from a structural MR image, and real EEG data: the anatomical and temporal constraints are extracted and the basis function sets established in a user-independent way. The soft constraints are motivated probabilistically. Deep and shallow sources are rendered more likely to influence the electric potential equally at the electrodes irrespective of depth. A second important constraint may be derived from fMRI indices of activation: the prior probability of whether a source is active or not is modified according to the fMRI activation map (or any other location prior). Two commonly employed alternative solutions, a direct WMN solution and a Maximum Smoothness (MS) solution, are presented. The WMN solution uses only partial anatomical constraints (location and orientation of the sources but not their spatial coherence), and allows the inclusion of location priors. With the MS solution, the sources are located in the grey matter and the smoothest solution in three dimensions is obtained irrespective of the actual anatomical orientation and correlation of the sources. Moreover no location priors can be employed.

Simulated data were used in chapter 7 to explore a range of values of the hyperparameters involved. The IBF solution as well as the direct WMN and MS solutions were tested with various types of data: single or double simultaneously active sources, with or without location priors, and with noise-free or realistically noisy data. The location priors employed could be either accurate or mislocated (i.e. centred or not on the location of the active source), and for different levels, weak or strong. For the simulations with noisy data, two levels of signal-to-noise ratio were employed, low or high. The results of the simulations showed clearly the advantage of combining anatomical and functional constraints, in an approach such as the IBF solution, in terms of both accuracy and robustness of the solutions obtained. The ReML algorithm also proved to be an efficient way to estimate the hyperparameter λ as the level of noise regularisation was automatically adapted to the level of noise in the data.

The second part of the thesis introduces some original ideas into the domain of the EEG source localisation problem, for example: The extraction of the anatomical constraints (source location, orientation and coherence), based on a fully automated and user-independent procedure, does not require the complete reconstruction of the cortical surface, contrary to most procedures published so far. The *a priori* reduction of the solution space by the spatial IBF allows a 2-step approach and a better control of the spatial constraints imposed. The noise influence is controlled using temporal IBF and the ReML algorithm. Finally the thesis contains a fairly exhaustive testing of the proposed IBF solution and two other classical solutions under various conditions and different parameters values.

1.3 Notation conventions

Here are the notation conventions adopted for the rest of this work.

$\mathbf{A}$	matrix of size $m \times n$.
$\mathbf{a}$	vector of size $m \times 1$: $\mathbf{a} = [a_1\ a_2\ \ldots\ a_m]^t$.
$\mathbf{A}^t$, $\mathbf{a}^t$	transpose of matrix $\mathbf{A}$ and vector $\mathbf{a}$.
$\vec{a}$	vector of size 3×1: $\vec{a} = [a_x\ a_y\ a_z]^t = a_x\,\vec{e}_x + a_y\,\vec{e}_y + a_z\,\vec{e}_z$.
a, A	scalar values.
$\|\mathbf{a}\|$	2-norm of vector $\mathbf{a}$: $\|\mathbf{a}\| = \sqrt{\sum_{i=1}^{m} a_i^2}$
$\|\mathbf{A}\|$	Frobenius norm of matrix $\mathbf{A}$: $\|\mathbf{A}\| = \sqrt{\sum_{i=1}^{m}\sum_{j=1}^{n} A_{ij}^2}$.
$\|\mathbf{A}\|$	determinant of matrix $\mathbf{A}$.
$\|\mathbf{a}\|$	vector defined by the absolute value of the elements a_i of vector $\mathbf{a}$.
$\|\vec{a}\|$	length (or 2-norm) of vector $\vec{a}$: $\|\vec{a}\| = \sqrt{a_x^2 + a_y^2 + a_z^2}$.
$\|a\|$	absolute value of scalar a.
$\max(\mathbf{a})$	value of the maximum element of $\mathbf{a}$.
$\mathrm{diag}(\mathbf{A})$	vector containing the elements of the leading diagonal of $\mathbf{A}$.
$\mathrm{diag}(\mathbf{a})$	leading diagonal matrix with elements defined by the elements of $\mathbf{a}$.
$\mathrm{trace}(\mathbf{A})$	trace of the $m \times m$ square matrix $\mathbf{A}$: $\mathrm{trace}(\mathbf{A}) = \sum_{i=1}^{m} A_{ii}$
$\mathrm{svd}(\mathbf{A})$	singular value decomposition of matrix $\mathbf{A}$: $\mathbf{A} = \mathbf{USW}^t$
$\vec{a}\,\vec{b}$	scalar product of $\vec{a}$ and $\vec{b}$.
$\vec{a} \times \vec{b}$	vectorial product of $\vec{a}$ and $\vec{b}$.
$\vec{\nabla} a$	gradient of a: $\vec{\nabla} a = \frac{\delta a}{\delta x}\,\vec{e}_x + \frac{\delta a}{\delta y}\,\vec{e}_y + \frac{\delta a}{\delta z}\,\vec{e}_z$.
$\vec{\nabla}\vec{a}$	divergence of $\vec{a}$: $\vec{\nabla}\vec{a} = \frac{\delta a_x}{\delta x} + \frac{\delta a_y}{\delta y} + \frac{\delta a_z}{\delta z}$.
$\vec{\nabla} \times \vec{a}$	rotational of $\vec{a}$: $\vec{\nabla} \times \vec{a} = \left(\frac{\delta a_z}{\delta y} - \frac{\delta a_y}{\delta z}\right)\vec{e}_x + \left(\frac{\delta a_x}{\delta z} - \frac{\delta a_z}{\delta x}\right)\vec{e}_y + \left(\frac{\delta a_y}{\delta x} - \frac{\delta a_x}{\delta y}\right)\vec{e}_z$.
$\nabla^2 a$	Laplacian of a: $\nabla^2 a = \vec{\nabla}(\vec{\nabla} a) = \frac{\delta^2 a}{\delta x^2} + \frac{\delta^2 a}{\delta y^2} + \frac{\delta^2 a}{\delta z^2}$.
$\otimes$	Kronecker product.
$\mathbf{I}_m$	identity matrix of size $m \times m$.
$\mathbf{1}_m$	vector of ones $\mathbf{1}_m = [1\ 1\ \ldots\ 1]^t$ of size $m \times 1$.

Part I

Forward Problem

Chapter 2

The Boundary Element Method

Contents

2.1 Maxwell's equations

In the forward problem, the conductivity of the head (or at least in its simplified model) and the location of the electric current generators in the brain are assumed to be known, and Maxwell's equations can be used to calculate the electric (and magnetic) field on the surface of the scalp. In differential equation form, Maxwell's equations can be stated like this (Ramo *et al.*, 1984) :

$$\vec{\nabla}\vec{E} = \frac{\rho}{\epsilon} \tag{2.1a}$$

$$\vec{\nabla}\vec{B} = 0 \tag{2.1b}$$

$$\vec{\nabla} \times \vec{E} = -\frac{\partial \vec{B}}{\partial t} \tag{2.1c}$$

$$\vec{\nabla} \times \vec{B} = \mu\vec{j} + \mu\epsilon\frac{\partial \vec{E}}{\partial t} \tag{2.1d}$$

where :

- $\vec{E}$ is the electric field
- $\vec{B}$ is the magnetic field
- $\vec{j}$ is the current density
- ρ is the charge density

- ϵ is the electric permitivity
- μ is the magnetic permeability

This set of equations, together with certain auxiliary relations and definitions (like Ohm's law and the continuity equation), is the basic set of equations of classical electricity and magnetism, governing all electromagnetic phenomena. In the case of bioelectric phenomenon such as the electro- and magnetoencephalography (EEG and MEG), we are only interested in the electric (and magnetic) field $\vec{E}$ (and $\vec{B}$). The treatment of Maxwell's equations can be significantly simplified from the outset by noting that the media involved have no significant capacitance : they are either purely resistive or the frequency of the activity is sufficiently low to neglect the capacitance (even sharp pulse with small rise time are not disturbed). So there is no electromagnetic wave propagation phenomenon (Hämäläinen *et al.*, 1993; He, 1998).

This assumption allows us to adopt a quasistatic approximation of Maxwell's equations, which means that, in the calculation of $\vec{E}$ (and $\vec{B}$), $\partial\vec{E}/\partial t$ and $\partial\vec{B}/\partial t$ can be ignored as source terms. Physically, these assumptions mean that the instantaneous current density depends only on the instantaneous current sources and follow the superposition theorem. Equation 2.1c then becomes $\vec{\nabla} \times \vec{E} = 0$ and therefore the electric field $\vec{E}$ can be expressed as the negative gradient of a scalar field, the electric potential V :

$$\vec{E} = -\vec{\nabla}V \tag{2.2}$$

By the definition of conduction current (Ohm's law) and the continuity equation, we also have these relations :

$$\vec{j} = \sigma\vec{E} \tag{2.3}$$

$$\vec{\nabla}\vec{j} = \frac{\partial\rho}{\partial t} \tag{2.4}$$

"Current sources" are by definition a distribution of forced current density $\vec{j}_f$. The current sources $\vec{j}_f$ can be seen as the summed coherent electric activity of the activated cell membranes, i.e. the current density directly produced by the neural activity, the sink and the source current terms being arbitrarily close. The total current density $\vec{j}_{tot}$ flowing through the media is equal to the sum of the imposed sources $\vec{j}_f$ and the return current $\vec{j}_r$. The later is the result of the macroscopic electric field on charge carriers in the conducting medium : $\vec{j}_r = \sigma\vec{E}$. With equations 2.3 and 2.2, we have :

$$\vec{j}_{tot} = \sigma\vec{E} + \vec{j}_f \tag{2.5a}$$

$$= -\sigma\vec{\nabla}V + \vec{j}_f \tag{2.5b}$$

By neglecting the capacitance of the head tissues, there is no charge accumulation in the volume or on the interfaces, i.e. the charges are redistributed in a negligible time. This translates mathematically by setting the divergence of the current density to zero and 2.4 becomes :

$$\vec{\nabla}\vec{j}_{tot} = 0 \tag{2.6}$$

By combining 2.5b and 2.6, we obtain the simplified Maxwell's equation linking the current sources $\vec{j}_f$ and the electric potential V :

$$\vec{\nabla}(\sigma\vec{\nabla}V) = \vec{\nabla}\vec{j}_f \tag{2.7}$$

Equation 2.7 can be solved for V in various ways depending on the geometry of the model, the form of the conductivity σ and the location of the sources $\vec{j}_f$. An analytical solution is possible only for particular cases : highly symmetrical geometry (e.g. concentric spheres or cubes) and homogeneous isotropic conductivity, see appendix B. For the other more general and useful cases, numerical methods are required. Common methods are the Finite Element Method (FEM) (Chari & Silvester, 1980; van den Broek *et al.*, 1996; Klepfer *et al.*, 1997; Buchner *et al.*, 1997; Awada *et al.*, 1997), the Finite Difference Method (FDM) (Rosenfeld *et al.*, 1996; Saleheen & Ng, 1997, 1998) and the Boundary Element Method (BEM) (Becker, 1992; Ferguson & Stroink, 1997; Mosher *et al.*, 1999).

The FEM and FDM make no assumption about the shape of the volume conductivity and allow the estimation of V at any location in the volume. The volume is tessellated into small volume elements in which Maxwell's equations are solved locally. As each volume element is characterised by its own conductivity (isotropic or not), any type of conductive volume layout can be modelled. With the FEM, the volume elements are of arbitrary shape (usually tetrahedron or regular polyhedron), while the volume elements are kept cubic for the FDM. By contrast, the BEM is based on the hypothesis that the volume is divided into sub-volumes of homogeneous and isotropic conductivity, and the potential V is only estimated on the surfaces separating those sub-volumes.

The FEM and FDM offer thus a more general solution of the forward problem but the complexity of the numerical problem and the computing time needed to solve it are greatly increased compared to the BEM. Moreover, the conductivity throughout the volume, necessary to make full use of the FEM and FDM power, cannot be directly estimated for individual patients. Therefore a simple "three sphere shell" model with an analytical solution is generally used in the field of EEG source localisation problem. A more anatomically realistic but still tractable approach can be achieved using the BEM to solve the forward problem. The FEM and FDM will not be further discussed in this work.

2.2 Boundary conditions and Green's theorem

2.2.1 Boundary conditions

Consider S_l the surface separating 2 volumes, vol^- and vol^+, of respective conductivity σ^- and σ^+. Let's define dS_l an infinitesimal element of this surface and $\vec{n}$ the unit vector normal to the surface oriented from the inside towards the outside of the surface, or by convention from vol^- to vol^+, as shown in figure 2.1.

There are no sources located on the surfaces between homogeneous volumes and the normal current through the surfaces is continuous, so on surface S_l, we have $\vec{j}_{tot} = -\sigma\vec{\nabla}V$ and

$$\sigma^-\vec{\nabla}V^-d\vec{S}_l = \sigma^+\vec{\nabla}V^+d\vec{S}_l \tag{2.8}$$

where $d\vec{S}_l = \vec{n}\,dS_l$ is the **oriented** infinitesimal element of this surface. Moreover the potential V must also be continuous on S_l :

$$V^-(S_l) = V^+(S_l) \tag{2.9}$$

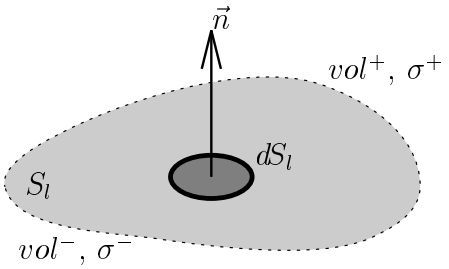

Figure 2.1: The surface S_l separates the two homogeneous volumes vol^- and vol^+ of isotropic conductivity σ^- and σ^+. dS_l is an infinitesimal element of the surface S_l and $\vec{n}$ is the unit vector normal to S_l, oriented from vol^- to vol^+.

The relations 2.8 and 2.9 provides the two boundary conditions necessary to solve the quasistatic form of Maxwell's equations as expressed in 2.7.

2.2.2 Green's theorem

Let dv_k be an element of the homogeneous regional volume vol_k (where $k = 1, \ldots, N_v$ and N_v is the number of homogeneous volumes) and $d\vec{S}_l$ be an oriented element, $d\vec{S}_l = \vec{n}\, dS_l$, of the surface S_l separating two regions of homogeneous conductivity (where $l = 1, \ldots, N_S$ and N_S is the number of such surfaces). Take now ψ and ϕ two well behaved functions in each region vol_k, then Green's theorem states (Smythe, 1950, chap. 3, pp. 48–58) :

$$\sum_{l}^{N_S} \int_{S_l} \left[\sigma_l^-(\psi^-\vec{\nabla}\phi^- - \phi^-\vec{\nabla}\psi^-) - [\sigma_l^+(\psi^+\vec{\nabla}\phi^+ - \phi^+\vec{\nabla}\psi^+)\right] d\vec{S}_l$$

$$= \sum_{k}^{N_v} \int_{vol_k} \left[\psi\vec{\nabla}(\sigma_k\vec{\nabla}\phi) - \phi\vec{\nabla}(\sigma_k\vec{\nabla}\psi)\right] dv_k \qquad (2.10)$$

where the sums run over the N_v volumes and the N_S surfaces, and the symbols $-$ and $+$ refer to the volumes inside and outside surface S_l.

The forward problem consists in determining the electric potential V from the current sources distribution $\vec{j}_f$ knowing the quasistatic form of Maxwell's equation 2.7 and the boundary conditions 2.8 and 2.9 using a BEM approach. This can be achieved by using the Green's theorem 2.10. Many expressions can be derived from 2.10 with an appropriate choice for the functions ϕ and ψ.

2.3 Analytical BEM equation

In 2.10, if we take $\psi = 1/r$ where r is the distance between an arbitrary point $\vec{r}$ and the origin $\vec{o}$ of space, then for smooth surfaces 2.10 becomes, as shown in appendix A and (Geselowitz, 1967) :

$$\sum_{l}^{N_S} \int_{S_l} \left[(\sigma_l^- \vec{\nabla}\phi^- - \sigma_l^+ \vec{\nabla}\phi^+)\frac{1}{r} - (\sigma_l^- \phi^- - \sigma_l^+ \phi^+)\vec{\nabla}\left(\frac{1}{r}\right) \right] d\vec{S}_l$$
$$= 4\pi\sigma\phi + \sum_{k}^{N_v} \int_{vol_k} \frac{1}{r}\, \vec{\nabla}\left(\sigma_k \vec{\nabla}\phi\right)\, dv_k \qquad (2.11)$$

where, in the first term of the right hand side, σ and ϕ are evaluated at the origin $\vec{o}$ of space, i.e. for $r = 0$.

Consider $\phi = V$ and suppose that $\vec{j}_f$ is distributed in only one homogeneous volume, the brain volume vol_{br}, then thanks to the simplified Maxwell's equation 2.7 and the boundary conditions 2.8 and 2.9, equation 2.11 becomes:

$$-\sum_{l}^{N_S}(\sigma_l^- - \sigma_l^+) \int_{S_l} V\, \vec{\nabla}\left(\frac{1}{r}\right) d\vec{S}_l = 4\pi\sigma V + \int_{vol_{br}} \frac{1}{r}\, \vec{\nabla}\vec{j}_f\, dv_{br} \qquad (2.12)$$

By the divergence theorem and the definition of the divergence operator $\vec{\nabla}$, we have:

$$\int_{vol} \vec{\nabla}\left(\frac{\vec{j}_f}{r}\right)\, dv = \int_S \frac{\vec{j}_f}{r} d\vec{S} = \int_{vol} \left[\vec{j}_f \vec{\nabla}\left(\frac{1}{r}\right) + \frac{1}{r}\vec{\nabla}\vec{j}_f \right]\, dv \qquad (2.13)$$

As there are no sources $\vec{j}_f$ on any surface S_l: $\vec{j}_f(S_l) = 0$, thus:

$$\int_{vol} \frac{1}{r}\vec{\nabla}\vec{j}_f\, dv = -\int_{vol} \vec{j}_f \vec{\nabla}\left(\frac{1}{r}\right)\, dv \qquad (2.14)$$

With relation 2.14, equation 2.12 becomes:

$$4\pi\sigma V = \int_{vol_{br}} \vec{j}_f \vec{\nabla}\left(\frac{1}{r}\right)\, dv_{br} - \sum_{l}^{N_S}(\sigma_l^- - \sigma_l^+) \int_{S_l} V\, \vec{\nabla}\left(\frac{1}{r}\right) d\vec{S}_l \qquad (2.15)$$

On the left hand side of 2.15, V is still evaluated at the origin $\vec{o}$ of space (an arbitrary point) and r is the distance from that origin to a point on the surface S_l (in the surface integrals) or in the volume vol_{br} (in the volume integral).

Let's consider $\vec{x}$ the point where V is evaluated, $\vec{s}\,'$ a point on the surface S_l and $\vec{r}\,'$ a point in the volume vol_{br}. The distance r between the point $\vec{x}$ where V is evaluated and any point $\vec{s}\,'$ on the surface S_l' (or $\vec{r}\,'$ in the volume vol_{br}) will the be expressed by $|\vec{x} - \vec{s}\,'|$ (or $|\vec{x} - \vec{r}\,'|$). Thus equation 2.15 is rewritten (Sarvas, 1987) like this:

$$\begin{aligned} 4\pi\sigma(\vec{x})V(\vec{x}) \;=\; & \int_{Vol_{br}} \vec{j}_f(\vec{r}\,')\vec{\nabla}'\left(\frac{1}{|\vec{x} - \vec{r}\,'|}\right)\, dv_{br} \\ & - \sum_{l}^{N_S}(\sigma_l^- - \sigma_l^+) \int_{S_l'} V(\vec{s}\,')\vec{\nabla}'\left(\frac{1}{|\vec{x} - \vec{s}\,'|}\right) d\vec{S}_l' \end{aligned} \qquad (2.16)$$

where $\vec{\nabla}'$ means that the gradient is applied on the primed variable: $\vec{r}\,'$ or $\vec{s}\,'$. The potential V should be evaluated on the surfaces S_l but, if $\vec{x}$ approaches the point $\vec{s}$ on a surface S_k, the k^{th} surface integral becomes singular in 2.16.

Consider now $F_k(\vec{x})$ the integral on the smooth surface S_k in 2.16,

$$F_k(\vec{x}) = \int_{S'_k} V(\vec{s}\,')\vec{\nabla}'\Big(\frac{1}{|\vec{x}-\vec{s}\,'|}\Big)\, d\vec{S}'_k \tag{2.17}$$

then it follows from Vladimirov (1971, chap. 5, p. 302) :

$$\lim_{\vec{x}\to\vec{s}} F_k(\vec{x}) = -2\pi V(\vec{s}) + F_k(\vec{s}) \tag{2.18}$$

where $\vec{x}$ approaches the point $\vec{s}$ on the surface S_k from the inside, so in the volume of conductivity σ_k^-.

With 2.18, the point $\vec{x}$ can be placed on any surface S_k and, with $\vec{x} \to \vec{s}$, equation 2.16 becomes :

$$\begin{aligned} 4\pi\sigma_k^- V(\vec{s}) \;=\; & \int_{Vol_{br}} \vec{j}_f(\vec{r}\,')\vec{\nabla}'\Big(\frac{1}{|\vec{s}-\vec{r}\,'|}\Big)\, dv_{br} \\ & -\sum_l^{N_S}(\sigma_l^- - \sigma_l^+)\int_{S'_l} V(\vec{s}\,')\vec{\nabla}'\Big(\frac{1}{|\vec{s}-\vec{s}\,'|}\Big)\, d\vec{S}'_l \\ & +2\pi(\sigma_k^- - \sigma_k^+)V(\vec{s}) \end{aligned} \tag{2.19}$$

and eventually

$$\begin{aligned} \frac{\sigma_k^- + \sigma_k^+}{2} V(\vec{s}) \;=\; & \frac{1}{4\pi}\int_{Vol_{br}} \vec{j}_f(\vec{r}\,')\vec{\nabla}'\Big(\frac{1}{|\vec{s}-\vec{r}\,'|}\Big)\, dv_{br} \\ & -\sum_l^{N_S}\frac{(\sigma_l^- - \sigma_l^+)}{4\pi}\int_{S'_l} V(\vec{s}\,')\vec{\nabla}'\Big(\frac{1}{|\vec{s}-\vec{s}\,'|}\Big)\, d\vec{S}'_l \end{aligned} \tag{2.20}$$

This is an explicit relationship between the current sources $\vec{j}_f$ and the surface potential V. The first term (on the right hand side of 2.20) is the direct contribution of $\vec{j}_f$ to the potential V and is similar to what would be obtained in an infinite homogeneous conductor. The second term is the "correction" for the inhomogeneities in the volume, it uses the potential on all the surfaces separating homogeneous volumes. It is important to remember that the surfaces are assumed to be smooth, i.e. do not have sharp edges or corners like in a cube. As V is present on both side of this integral equation, V cannot be directly and analytically evaluated (except for particular and highly symmetrical layouts) and numerical methods are required to solve this integral equation.

Chapter 3

Solving the BEM equation

Contents

3.1 Approximation of the BEM equation

3.1.1 Original formulation

The previous chapter demonstrated how to express, equation 2.20, the forward problem as an integral form of Maxwell's equations:

$$V(\vec{s}) = V_\infty(\vec{s}) - \frac{1}{2\pi}\sum_{l}^{N_S}\frac{\sigma_l^- - \sigma_l^+}{\sigma_k^- + \sigma_k^+}\int_{S_l'} V(\vec{s}\,')\vec{\nabla}'\left(\frac{1}{|\vec{s}-\vec{s}\,'|}\right)\vec{n}(\vec{s}\,')\,dS_l' \tag{3.1}$$

where $V_\infty(\vec{s})$ is the potential due to $\vec{j}_f$ in a conductor of infinite extent and homogeneous conductivity $(\sigma_k^- + \sigma_k^+)/2$:

$$V_\infty(\vec{s}) = \frac{1}{2\pi(\sigma_k^- + \sigma_k^+)} \int_v \vec{j}_f(\vec{r}\,') \vec{\nabla}' \left(\frac{1}{|\vec{s} - \vec{r}\,'|} \right) dv \tag{3.2}$$

and

- the sum $\sum_l^{N_S}$ runs over all the surfaces separating volumes of homogeneous isotropic conductivity.
- σ_l^- and σ_l^+ are the conductivity inside and outside[1] the surface S_l.
- $\vec{s}$ and $\vec{s}\,'$ are points on the surfaces S_k and S_l respectively.
- $\vec{n}(\vec{s}\,')$ is a unit vector normal to the surface S_l at the point $\vec{s}\,'$ and oriented from the inside towards the outside of S_l.

Solving equation 3.1 for V would provide us with a way to estimate the potential at any location on any surface given any source $\vec{j}_f$ in the brain volume.

3.1.2 General approach

The main task of solving the forward problem is to evaluate accurately the integrals on the right hand side of equation 3.1. The volume integral over the continuous sources distribution $\vec{j}_f$ can be easily calculated by approximating $\vec{j}_f$ as a superposition of independent point sources of known location and orientation. This reduces the volume integral into a sum of independent contributions for each location and orientation of the sources.

On the other hand the surface integrals are more difficult to calculate: they run on different and irregular surfaces and, moreover, they involve the potential $V(\vec{s})$ that is sought after. Therefore it will be necessary to express the surface integrals in terms of the value of the unknown function V at some discrete set of points on the surfaces, and to tessellate the surfaces into sets of regular patches.

The most obvious approximation for the surfaces is to model each of them by a set of plane triangles. With this surface tessellation, the surface integrals of 3.1 can be expressed as a sum of integrals over triangles:

$$V(\vec{s}) = V_\infty(\vec{s}) - \frac{1}{2\pi} \sum_{l=1}^{N_S} \frac{\sigma_l^- - \sigma_l^+}{\sigma_k^- + \sigma_k^+} \sum_{m=1}^{N_{tr}^{(l)}} \int_{\triangle_m^{(l)}} V(\vec{s}\,') \vec{\nabla}' \left(\frac{1}{|\vec{s} - \vec{s}\,'|} \right) \vec{n}(\vec{s}\,')\, dS' \tag{3.3}$$

where the surface S_l has been modelled by a set of $N_{tr}^{(l)}$ triangles $\triangle_m^{(l)}$.

The function V is rendered discrete by choosing on which nodal points V is evaluated and how the function V behaves on each individual plane triangle. This would allow an explicit calculation of the integrals over the triangles and equation 3.3 could eventually be simplified into a sum of known or, at least, easily evaluated analytical functions.

[1] The notion of "inside" and "outside" depends on the orientation of the normal $\vec{n}(\vec{s}\,')$ to the surface.

Three different approximations of V over a triangle are usually considered. First, one could choose to evaluate V at the centre of gravity of each triangle and consider this value constant over the triangle: one value is thus obtained for each triangle. This approximation shall be referred as the "Centre of Gravity" (or "CoG") method (Hämäläinen & Sarvas, 1989; Meijs *et al.*, 1989). The function V could also be evaluated on the vertices of the triangles, this is generally called a "vertex" approximation (one value per vertex). If the potential over the triangle is supposed to be constant and equal to the mean of the potential at its vertices, this approximation will be called the "Constant Potential at Vertices" (or "CPV") method. On the other hand, if the potential is considered to be varying linearly over the triangle, this approximation will be named the "Linear Potential at Vertices" (or "LPV") method (Schlitt *et al.*, 1995).

The CoG and vertices (CPV and LPV) methods differ mainly on the choice of the nodal points where the unknown potential function V is calculated. It is important to note that for a closed tessellated surface there are about twice as many triangles as vertices. The number and arrangement of the triangles determine how well the true surface is spatially approximated. The choice of the potential approximation method determines the number of equations to be solved (one per triangle or vertex) and how well the true potential is modelled over each triangle (constant or linear approximation).

3.1.3 Current source model

In equation 3.2, the source function $\vec{j}_f(\vec{r})$ is a continuous function throughout the volume. To be able to solve numerically the BEM equation 3.1, a discrete approximation of the source function has to be adopted. The source function $\vec{j}_f(\vec{r})$ can be approximated by a distribution of N_j independent dipole sources of known location $\vec{r}_i$:

$$\vec{j}_f(\vec{r}) = \sum_{i=1}^{N_j} \left[\int_{v_i} \vec{j}_f(\vec{r}\,')\, dv_i \right] \delta(\vec{r} - \vec{r}_i) \tag{3.4a}$$

$$= \sum_{i=1}^{N_j} \vec{j}_f(\vec{r}_i)\ \delta(\vec{r} - \vec{r}_i) \tag{3.4b}$$

where $\vec{j}_f(\vec{r}_i) = \int_{v_i} \vec{j}_f(\vec{r}\,')\, dv_i$ is the summed activity in the volume v_i around the location $\vec{r}_i$ and $\delta(\vec{r})$ is the discrete Dirac delta function[2].

Now with relation 3.4, equation 3.2 becomes:

$$V_\infty(\vec{s}) = \frac{1}{2\pi(\sigma_k^- + \sigma_k^+)} \int_v \vec{j}_f(\vec{r}\,')\vec{\nabla}'\!\left(\frac{1}{|\vec{s} - \vec{r}\,'|}\right) dv \tag{3.5a}$$

$$= \frac{1}{2\pi(\sigma_k^- + \sigma_k^+)} \int_v \frac{\vec{s} - \vec{r}\,'}{|\vec{s} - \vec{r}\,'|^3} \sum_{i=1}^{N_j} \vec{j}_f(\vec{r}_i)\ \delta(\vec{r}\,' - \vec{r}_i)\ dv \tag{3.5b}$$

$$= \frac{1}{2\pi(\sigma_k^- + \sigma_k^+)} \sum_{i=1}^{N_j} \vec{j}_f(\vec{r}_i) \int_v \frac{\vec{s} - \vec{r}\,'}{|\vec{s} - \vec{r}\,'|^3}\ \delta(\vec{r}\,' - \vec{r}_i)\ dv \tag{3.5c}$$

[2] $\delta(\vec{r})$ equals 1 if $\vec{r} = \vec{o}$ and 0 for $\vec{r} \neq \vec{o}$

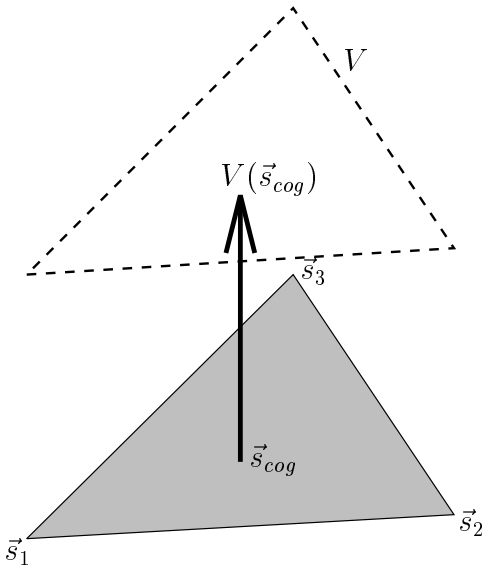

Figure 3.1: The Centre of Gravity (CoG) potential approximation : the potential V over the triangle is assumed to be constant and equal to the potential at the centre of gravity $\vec{s}_{cog}$ of the triangle, $V = V(\vec{s}_{cog})$.

and eventually we obtain :

$$V_\infty(\vec{s}) = \frac{1}{2\pi(\sigma_k^- + \sigma_k^+)} \sum_{i=1}^{N_j} \frac{\vec{s} - \vec{r}_i}{|\vec{s} - \vec{r}_i|^3} \, \vec{\jmath}_f(\vec{r}_i) \tag{3.6}$$

3.1.4 Potential function model

The "Centre of Gravity" approximation

With this approximation, the unknown function V is calculated on nodal points located at the centre of gravity of each triangle. The potential over the triangle is supposed to be constant and equal to the potential at the centre of gravity $V = V(\vec{s}_{cog})$, as shown in figure 3.1.

With this approximation of the potential, the integral over each triangle in 3.3 can be simplified :

$$\begin{aligned} \int_{\triangle_m^{(l)}} V(\vec{s}\,') \vec{\nabla}' \Big(\frac{1}{|\vec{s} - \vec{s}\,'|} \Big) \, \vec{n}(\vec{s}\,') \, dS' &= V(\vec{s}\,'_{cog}) \int_{\triangle_m^{(l)}} \vec{\nabla}' \Big(\frac{1}{|\vec{s} - \vec{s}\,'|} \Big) \, \vec{n}(\vec{s}\,') \, dS' && \text{(3.7a)} \\ &= -V(\vec{s}\,'_{cog}) \, \Omega^{(l,m)}(\vec{s}) && \text{(3.7b)} \end{aligned}$$

where $\Omega^{(l,m)}(\vec{s})$ is the solid angle at $\vec{s}$ subtended by the triangle $\triangle_m^{(l)}$:

$$\begin{aligned} \Omega^{(l,m)}(\vec{s}) &= -\int_{\triangle_m^{(l)}} \vec{\nabla}' \Big(\frac{1}{|\vec{s} - \vec{s}\,'|} \Big) \, \vec{n}(\vec{s}\,') \, dS' && \text{(3.8a)} \\ &= \int_{\triangle_m^{(l)}} \frac{\vec{s}\,' - \vec{s}}{|\vec{s}\,' - \vec{s}\,|^3} \vec{n}(\vec{s}\,') \, dS' && \text{(3.8b)} \end{aligned}$$

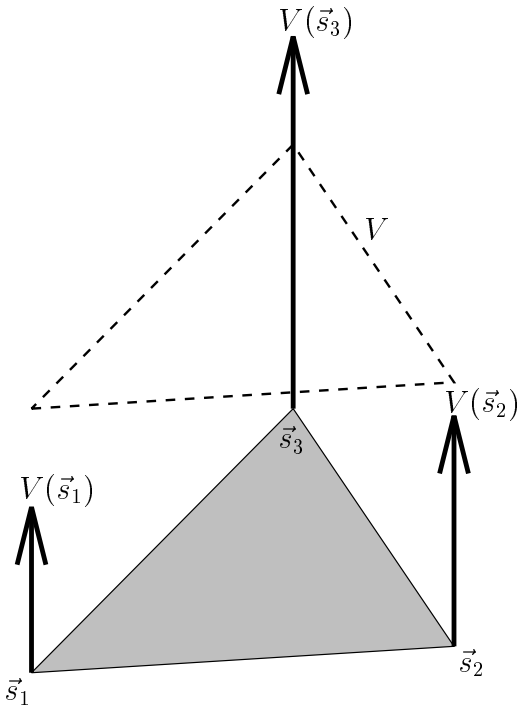

Figure 3.2: The Constant Potential at Vertices (CPV) potential approximation: The potential V over the triangle is assumed to be constant and equal to the mean of the potential at each vertex $\vec{s}_1$, $\vec{s}_2$ and $\vec{s}_3$ of the triangle, $V = (V(\vec{s}_1) + V(\vec{s}_2) + V(\vec{s}_3))/3$.

This last integral depends only on the three vector differences between $\vec{s}$ (the "point of view") and the three vertices $\vec{s}\,'_1$, $\vec{s}\,'_2$ and $\vec{s}\,'_3$ (the "points of support") determining the triangle $\triangle_m^{(l)}$. There exists an explicit analytic formula to calculate $\Omega^{(l,m)}(\vec{s})$, it will be presented in section 3.2.1.

The BEM equation 3.3 eventually becomes a "simple sum of known analytical functions" :

$$V(\vec{s}_{cog,p}) = V_\infty(\vec{s}_{cog,p}) + \frac{1}{2\pi} \sum_{l=1}^{N_S} \frac{\sigma_l^- - \sigma_l^+}{\sigma_k^- + \sigma_k^+} \sum_{m=1}^{N_{tr}^{(l)}} V(\vec{s}_{cog,m})\ \Omega^{(l,m)}(\vec{s}_{cog,p}) \tag{3.9}$$

where $\vec{s}_{cog,m}$ (resp. $\vec{s}_{cog,p}$) is the "centre of gravity" of the m^{th} (resp. p^{th}) triangle $\triangle_m^{(l)}$ (resp. $\triangle_p^{(k)}$) of the l^{th} (resp. k^{th}) surface S_l (resp. S_k). The BEM problem has now the form of a set of linear equations. Its solution is presented in section 3.3.

The "Constant Potential at Vertices" approximation

Here the potential is evaluated on the vertices of the triangles and the potential over each triangle is assumed to be constant and equal to the mean of the potential at its vertices $V = (V(\vec{s}_1) + V(\vec{s}_2) + V(\vec{s}_3))/3$, as shown in figure 3.2.

With this approximation of the potential, the integral over each triangle in 3.3 can be

simplified like this:

$$\int_{\triangle_m^{(l)}} V(\vec{s}\,')\vec{\nabla}'\Big(\frac{1}{|\vec{s}-\vec{s}\,'|}\Big)\,\vec{n}(\vec{s}\,')\,dS'$$

$$= \frac{V(\vec{s}\,'_1)+V(\vec{s}\,'_2)+V(\vec{s}\,'_3)}{3}\int_{\triangle_m^{(l)}}\vec{\nabla}'\Big(\frac{1}{|\vec{s}-\vec{s}\,'|}\Big)\,\vec{n}(\vec{s}\,')\,dS' \quad (3.10a)$$

$$= -\frac{V(\vec{s}\,'_1)+V(\vec{s}\,'_2)+V(\vec{s}\,'_3)}{3}\,\Omega^{(l,m)}(\vec{s}) \quad (3.10b)$$

where $\Omega^{(l,m)}(\vec{s})$ is the solid angle at $\vec{s}$ subtended by the triangle $\triangle_m^{(l)}$, expressed like in equation 3.8. An analytical formula to calculate it is provided in section 3.2.1.

The BEM equation 3.3 also becomes a "simple sum of known analytical functions":

$$V(\vec{s}_\bullet) = V_\infty(\vec{s}_\bullet) + \frac{1}{2\pi}\sum_{l=1}^{N_S}\frac{\sigma_l^- - \sigma_l^+}{\sigma_k^- + \sigma_k^+}\sum_{m=1}^{N_{tr}^{(l)}}\frac{V(\vec{s}\,'_{1,m})+V(\vec{s}\,'_{2,m})+V(\vec{s}\,'_{3,m})}{3}\,\Omega^{(l,m)}(\vec{s}_\bullet) \quad (3.11)$$

where $\vec{s}_\bullet$ is one of the three vertices of a triangle of the k^{th} surface S_k and $\vec{s}_{i,m}{}'$ is the i^{th} vertex of the m^{th} triangle $\triangle_m^{(l)}$ of the l^{th} surface S_l. The BEM problem is now also expressed as a set of linear equations, and its solution is presented in section 3.3.

The "Linear Potential at Vertices" approximation

Here the potential is also evaluated on the vertices of the triangles but a better approximation of the potential over the triangles is used: The potential is assumed to be varying linearly over each triangle, as shown in figure 3.3.

As only three values are needed to specify a linear function on a plane surface, the value of the potential V at the three vertices of the triangle can be used. Moreover this ensures that the potential varies continuously from one triangle to the next which was not the case with the two previous approximations.

As for the CPV approximation, the integral over each triangle in equation 3.3 can be simplified into a weighted sum of the potential at the vertices:

$$\int_{\triangle_m^{(l)}} V(\vec{s}\,')\vec{\nabla}'\Big(\frac{1}{|\vec{s}-\vec{s}\,'|}\Big)\,\vec{n}(\vec{s}\,')\,dS'$$

$$= -\Big(V(\vec{s}\,'_1)\,\Omega_1^{(l,m)}(\vec{s}) + V(\vec{s}\,'_2)\,\Omega_2^{(l,m)}(\vec{s}) + V(\vec{s}\,'_3)\,\Omega_3^{(l,m)}(\vec{s})\Big) \quad (3.12)$$

The three $\Omega_\bullet^{(l,m)}(\vec{s})$ are also purely geometric quantities depending on the vector differences between the "point of view" $\vec{s}$ and the vertices $\vec{s}\,'_\bullet$ of the triangle. An explicit analytical formula to calculate the $\Omega_\bullet^{(l,m)}(\vec{s})$ from $\vec{s}$ and $\vec{s}\,'_\bullet$ is presented in section 3.2.2.

With this approximation the BEM equation 3.3 also becomes a "simple sum of known analytical functions":

$$V(\vec{s}_\bullet) = V_\infty(\vec{s}_\bullet) + \quad (3.13)$$

$$\frac{1}{2\pi}\sum_{l=1}^{N_S}\frac{\sigma_l^- - \sigma_l^+}{\sigma_k^- + \sigma_k^+}\sum_{m=1}^{N_{tr}^{(l)}}\Big(V(\vec{s}\,'_{1,m})\,\Omega_1^{(l,m)}(\vec{s}_\bullet) + V(\vec{s}\,'_{2,m})\,\Omega_2^{(l,m)}(\vec{s}_\bullet) + V(\vec{s}\,'_{3,m})\,\Omega_3^{(l,m)}(\vec{s}_\bullet)\Big)$$

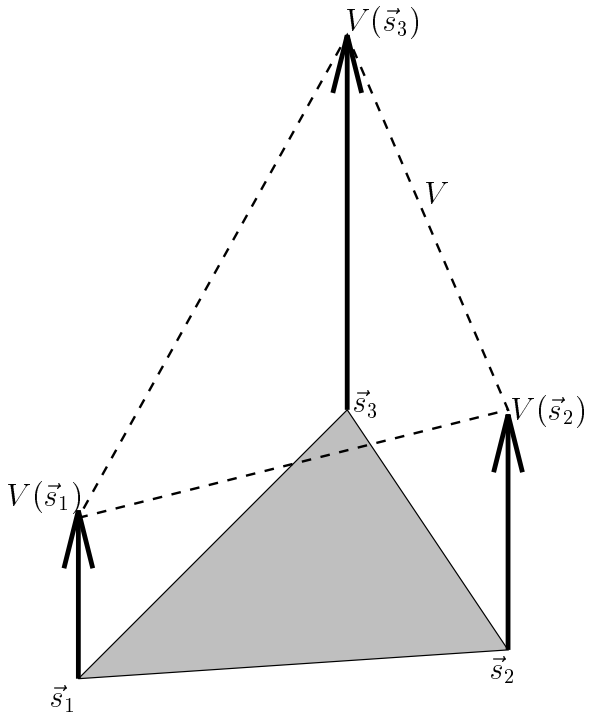

Figure 3.3: The Linear Potential at Vertices (LPV) potential approximation: The potential V over the triangle is assumed to be varying linearly between the potential calculated at each vertex $\vec{s}_1$, $\vec{s}_2$ and $\vec{s}_3$ of the triangle, $V = f(V(\vec{s}_1), V(\vec{s}_2), V(\vec{s}_3))$.

where $\vec{s}_\bullet$ is one of the three vertices of a triangle of the k^{th} surface S_k and $\vec{s}_{i,m}{}'$ is the i^{th} vertex of the m^{th} triangle $\triangle_m^{(l)}$ of the l^{th} surface S_l. The BEM problem is also reduced to a set of linear equations, and its solution is presented in section 3.3.

3.2 Solid angle calculation

3.2.1 Constant potential approximation

For both CoG and CPV approximations presented in section 3.1.4, the solid angle $\Omega^{(l,m)}(\vec{s})$ subtended by a plane triangle $\triangle_m^{(l)}$ at some point $\vec{s}$ has to be calculated.

Without loss of generality, the observation point $\vec{s}$ can be placed at the origin $\vec{o}^*$. The three vertices $\vec{s}_1$, $\vec{s}_2$ and $\vec{s}_3$ of the plane triangle are then specified by the vectors $\vec{v}_1 = \vec{s}_1 - \vec{o}^*$, $\vec{v}_2 = \vec{s}_2 - \vec{o}^*$ and $\vec{v}_3 = \vec{s}_3 - \vec{o}^*$ relative to this origin $\vec{o}^*$, as shown in figure 3.4. The solid angle Ω can be analytically expressed with $\vec{v}_1$, $\vec{v}_2$ and $\vec{v}_3$ by the formula taken from van Oosterom & Strackee (1983):

$$\tan\left(\frac{1}{2}\Omega\right) = \frac{\vec{v}_1(\vec{v}_2 \times \vec{v}_3)}{|\vec{v}_1|\,|\vec{v}_2|\,|\vec{v}_3| + (\vec{v}_1\vec{v}_2)|\vec{v}_3| + (\vec{v}_1\vec{v}_3)|\vec{v}_2| + (\vec{v}_2\vec{v}_3)|\vec{v}_1|} \tag{3.14}$$

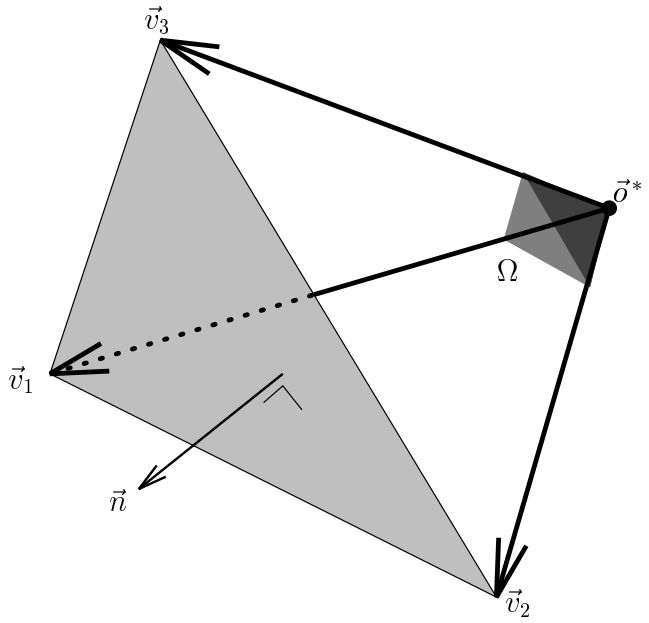

Figure 3.4: Solid angle supported by a plane triangle: The solid angle Ω supported at the point $\vec{o}^*$ by the plane triangle (grey shade) depends only on the three vectors $\vec{v}_1$, $\vec{v}_2$ and $\vec{v}_3$ and can be easily calculated by equation 3.14.

For the case where the point of view $\vec{s}$ is located on the same plane as the triangle $\triangle_m^{(l)}$, e.g. when $\vec{s}$ is at the centre of gravity of the triangle in the CoG approximation or when $\vec{s}$ is at a vertex of the triangle in the CPV approximation, the solid angle $\Omega^{(l,m)}(\vec{s})$ is zero. The consequences of this feature are presented in section 3.2.3.

3.2.2 Linear potential approximation

For the LPV approximation presented in section 3.1.4, three geometric quantities Ω_i ($i = 1, 2, 3$) have to be calculated for each triangle, under the assumption that the potential V varies linearly over this triangle. As for the previous section, the observation point $\vec{s}$ can again be placed at the origin $\vec{o}^*$ without loss of generality. The three vertices $\vec{s}_1$, $\vec{s}_2$ and $\vec{s}_3$ of the plane triangle are then specified by the vectors $\vec{v}_1 = \vec{s}_1 - \vec{o}^*$, $\vec{v}_2 = \vec{s}_2 - \vec{o}^*$ and $\vec{v}_3 = \vec{s}_3 - \vec{o}^*$ relative to this origin $\vec{o}^*$, as shown in figure 3.4. There also exists an analytical formula for the Ω_i (de Munck, 1992; Schlitt *et al.*, 1995):

$$\Omega_i = \frac{1}{2A}\left(\vec{z}_i\vec{n}\,\Omega + \beta(\vec{v}_j - \vec{v}_k)\vec{\Omega}\right) \tag{3.15}$$

where

- A is the surface of the plane triangle,
- $\vec{z}_i = \vec{v}_j \times \vec{v}_k$ with (i, j, k) a cyclic permutation of $(1, 2, 3)$,
- $\vec{n}$ is a unit vector normal to the triangle,

- Ω is the solid angle subtended by the plane triangle at the origin as expressed in formula 3.14,
- $\beta = \vec{n}\vec{v}_i$ is equal to the perpendicular distance from the origin to the triangle,
- $\vec{\Omega}$ is a vector defined by $\vec{\Omega} = \sum_{i=1}^{3} (\gamma_j - \gamma_i)\vec{v}_j$ with

$$\gamma_i = \frac{1}{|\vec{v}_j - \vec{v}_i|} \ln \left(\frac{|\vec{v}_j - \vec{v}_i|\,|\vec{v}_j| + (\vec{v}_j - \vec{v}_i)\vec{v}_j}{|\vec{v}_j - \vec{v}_i|\,|\vec{v}_i| + (\vec{v}_j - \vec{v}_i)\vec{v}_i} \right) \tag{3.16}$$

The Ω_i also satisfy the equality: $\Omega_1 + \Omega_2 + \Omega_3 = \Omega$. When the triangle $\triangle_m^{(l)}$ and the point of view $\vec{s}$ are coplanar, for example when $\vec{s}$ is at one of the vertices of the triangle, Ω and β are equal to zero, so $\Omega_1 = \Omega_2 = \Omega_3 = 0$. This problem is tackled in section 3.2.3.

3.2.3 The auto-solid angle problem

An important property of solid angle concerns its integral over a single closed surface. We know from equation 3.8 that the infinitesimal solid angle $d\Omega'$ subtended by the infinitesimal surface dS' around the point $\vec{s}\,'$ at the point of view $\vec{s}$ is expressed by:

$$d\Omega'(\vec{s}, \vec{s}\,') = \vec{n}(\vec{s}\,') \frac{\vec{s}\,' - \vec{s}}{|\vec{s}\,' - \vec{s}\,|^3}\, dS' \tag{3.17}$$

Then the integral of $d\Omega'(\vec{s}, \vec{s}\,')$ over a smooth closed surface is equal to:

$$\Omega_S(\vec{s}) = \int_S d\Omega'(\vec{s}, \vec{s}\,') = \left[\begin{array}{c} 0 \\ 2\pi \\ 4\pi \end{array} \right] \text{, for } \vec{s} \left[\begin{array}{c} \text{outside} \\ \text{on} \\ \text{inside} \end{array} \right] \text{the surface.} \tag{3.18}$$

The BEM equation 3.1 contains an integral of the form:

$$\int_S d\Omega'(\vec{s}, \vec{s}\,') V(\vec{s}\,') \tag{3.19}$$

then this integral is converted into a discrete sum, by equation 3.9, 3.11 or 3.14, of the form:

$$\sum_{m=1}^{M} \Omega_{nm}\, V_m \tag{3.20}$$

where:

- m and n are indices of nodal points (possibly on different surfaces) where the potential V is calculated.
- V_m is the potential at the point m.
- Ω_{nm} is the solid angle associated with the point m for the point of view n.
- M is the number of nodal points on the surface, i.e. the number of triangles for the CoG approximation or the number of vertices for the CPV and LPV approximations.

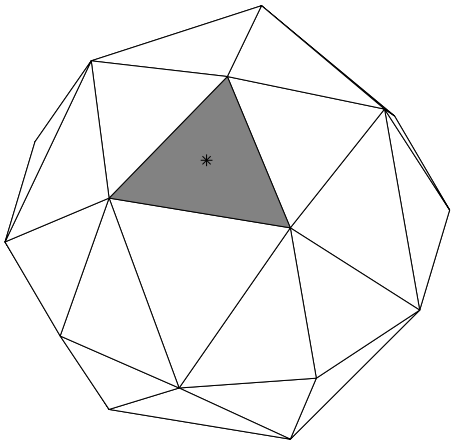

Figure 3.5: The auto-solid angle problem for the CoG approximation: The solid angle subtended by the grey triangle from its centre of gravity (the black dot) is zero but the total solid angle subtended by the rest of the surface (white triangles) is equal to 2π.

It is therefore important that the Ω_{nm} satisfy the relation 3.18:

$$\Omega_{n,S} = \sum_{m=1}^{M} \Omega_{nm} = \begin{bmatrix} 0 \\ 2\pi \\ 4\pi \end{bmatrix} \text{, for } \vec{s} \begin{bmatrix} \text{outside} \\ \text{on} \\ \text{inside} \end{bmatrix} \text{ the surface.} \tag{3.21}$$

In the case of $\vec{s}$ being outside or inside the surface, there is no problem to satisfy these equalities: All the Ω_{nm} can be unambiguously calculated with equation 3.14 or 3.15. But when $\vec{s}$ is on the surface itself then we meet the "auto-solid angle problem": the solid angle subtended by a triangle which contains the point of view is zero and the second equality of relation 3.21 may not be satisfied automatically.

The auto-solid angle problem for the CoG approximation

In the CoG approximation, as the potential is evaluated on the "centre of gravity" of each triangle, there will be only one null solid angle: $\Omega_{mm} = 0$, as can be seen in figure 3.5. Since the rest of the solid angle subtended by the closed surface is already 2π, there is no missing angle and the second equality of the relations 3.21 is satisfied.

Nevertheless, in reality the surface modelled by the triangle is not plane, and it should thus support some non-zero solid angle. There is no way to improve the solution, but to use a finer meshing of the surface.

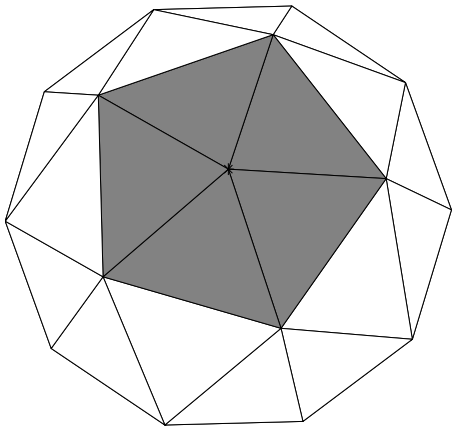

Figure 3.6: The auto-solid angle problem for the CPV and LPV approximations : The solid angle supported by the "central" point and the adjacent grey triangles is zero, therefore the total solid angle supported by the remaining white triangles is less than 2π.

The auto-solid angle problem for the CPV approximation

In the "vertices" approximations (CPV and LPV), all the adjacent triangles (grey triangles in figure 3.6) containing the "point of view" are supporting a null solid angle. The solid angle Ω_r subtended by the rest of the surface will **not** be equal to 2π because the adjacent triangles do not represent a flat surface.

$$\Omega_{miss} = 2\pi - \Omega_r = 2\pi - \sum_{m=1}^{M} \Omega_{nm} \tag{3.22}$$

It is necessary to distribute this "missing solid angle" Ω_{miss} over the triangles adjacent to the "point of view".

In the case of the CPV approximation, the easiest way to proceed is to share uniformly this "missing solid angle" between the adjacent triangles and their vertices. The central "point of view" should be attributed one third of the missing solid angle $\Omega_{miss}/3$, and the other vertices should receive $2\Omega_{miss}/(3N_{adj})$ where N_{adj} is the number of triangles adjacent to the central "point of view".

There exists a more elaborate way to split the missing solid angle between the adjacent triangles. The approach is based on a local spherical approximation of the surface surrounding the central vertex and is presented in the next section, in relation with the LPV approximation.

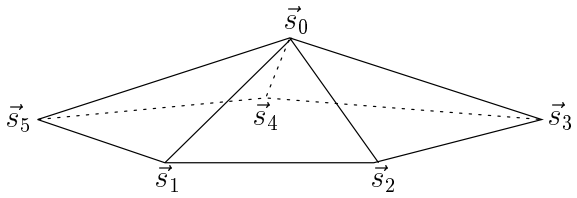

Figure 3.7: Adjacent triangles supporting a non-zero solid angle: The surface defined by $\vec{s}_1$, $\vec{s}_2$, ...,$\vec{s}_5$ around $\vec{s}_0$ support a non-zero solid angle. Each triangle, defined by a triplet of vertices ($[\vec{s}_0\vec{s}_1\vec{s}_2]$, $[\vec{s}_0\vec{s}_2\vec{s}_3]$, ..., $[\vec{s}_0\vec{s}_5\vec{s}_1]$), supports a part of the missing solid angle which in turn must be shared between its vertices. Each triangle can be locally approximated by a portion of sphere.

The auto-solid angle problem for the LPV approximation

The case of the LPV approximation is more complicated because the potential V is varying linearly over each triangle. There are two main problems: how to divide up the missing the solid angle Ω_{miss} between the adjacent triangles and, within each of them, how to share its part between its vertices. This is illustrated in figure 3.7. There exists an analytical formula to solve these problems (Heller, 1990) but it requires that each triangle around the point of view $\vec{s}_0$ be approximated by a portion of sphere of centre $\vec{r}_c$ and radius R. If the surface is regular and smooth compared to the density of the mesh, this local spherical approximation will hold as R will be much larger than the length of the edges of the triangles.

Since three points do not determine a sphere, a fourth point must be chosen. A suitable point would be the next adjacent vertex, e.g. the sphere that passes through the triplet $[\vec{s}_0\vec{s}_1\vec{s}_2]$ could be required to pass through $\vec{s}_3$ as well. A better and more anatomically correct approximation can be obtained, if, at the tessellation stage, the centre of gravity $\vec{s}_{cog}$ of each triangle is projected perpendicular to the triangular plane onto the actual surface of the volume $\vec{s}^{\perp}_{cog}$. Then a sphere can easily be fitted through these four points: the three vertices defining the triangle and its projected centre of gravity, as shown in figure 3.8. This approach was used in the implementation of the BEM solution.

Once the spheres have been fitted for $\vec{s}_0$ and its adjacent vertices $\vec{s}_1$, $\vec{s}_2$, ..., $\vec{s}_{N_{adj}}$, an approximate value for the solid angle subtended by each triplet $[\vec{s}_0\vec{s}_1\vec{s}_2]$, $[\vec{s}_0\vec{s}_2\vec{s}_3]$, ..., $[\vec{s}_0\vec{s}_{N_{adj}}\vec{s}_1]$ at $\vec{s}_0$ can be calculated. Using spherical coordinates for the vertices, as shown in figure 3.9, the solid angle $\Omega_{[\vec{s}_0\vec{s}_1\vec{s}_2]}$ subtended at $\vec{s}_0$ by the spherical region bounded by $\vec{s}_0$, $\vec{s}_1$ and $\vec{s}_2$, is approximated by:

$$\Omega_{[\vec{s}_0\vec{s}_1\vec{s}_2]} = \frac{\psi_1 + \psi_2}{4}\phi_{12} \tag{3.23}$$

where ψ_1 and ψ_2 are easily obtained and

$$\sin\frac{\phi_{12}}{2} = \frac{|\vec{s}_b - \vec{s}_2|}{2R\sin\psi_2} \tag{3.24}$$

with

$$\vec{s}_b = \vec{r}_c + \frac{1}{\sin\psi_1}\left[\sin(\psi_1 - \psi_2)(\vec{s}_0 - \vec{r}_c) + \sin\psi_2(\vec{s}_1 - \vec{r}_c)\right] \tag{3.25}$$

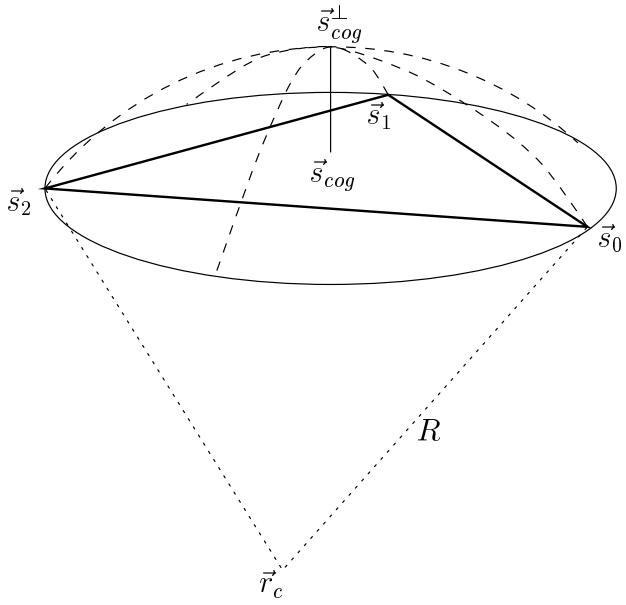

Figure 3.8: Spherical approximation of an adjacent plane triangle: The triplet of vertices $[\vec{s}_0\vec{s}_1\vec{s}_2]$ and the projection $\vec{s}^{\perp}_{cog}$ of the centre of gravity $\vec{s}_{cog}$ of the triangle on the actual surface determine a sphere, centre $\vec{r}_c$ and radius R, that approximates the actual surface.

After calculation of the solid angle for all the other triplets and summation, the total solid angle $\Omega_{\vec{s}_0}$ supported by $\vec{s}_1$, $\vec{s}_2$, ..., $\vec{s}_{N_{adj}}$ at $\vec{s}_0$ is approximated by:

$$\Omega_{\vec{s}_0} = \Omega_{[\vec{s}_0\vec{s}_1\vec{s}_2]} + \Omega_{[\vec{s}_0\vec{s}_2\vec{s}_3]} + \ldots + \Omega_{[\vec{s}_0\vec{s}_{N_{adj}}\vec{s}_1]} \tag{3.26}$$

The fraction of missing solid angle Ω_{miss} to be assigned to each triangle, e.g., $[\vec{s}_0\vec{s}_1\vec{s}_2]$, is obtained by:

$$f_{[\vec{s}_0\vec{s}_1\vec{s}_2]} = \frac{\Omega_{\vec{s}_0}}{\Omega_{[\vec{s}_0\vec{s}_1\vec{s}_2]}} \tag{3.27}$$

Note that, even though approximations are made in these calculations, since they only involve ratios, the total solid angle subtended by the region around $\vec{s}_0$ will sum to Ω_{miss}, and the total solid angle subtended by the entire surface at $\vec{s}_0$ will be exactly 2π. For the CPV approximation, the portion $f_{[\vec{s}_0\vec{s}_1\vec{s}_2]}\Omega_{miss}$ of missing solid angle is simply equally distributed between the three vertices of the triangle. For the LPV approximation, it is necessary to further share this portion of missing solid angle between the vertices of the adjacent triangles.

Assuming that ψ_1, ψ_2 and ϕ_{12} are small and that the potential V varies linearly with the distance on the sphere, Heller (1990) showed that it is possible to share the solid angle $f_{[\vec{s}_0\vec{s}_1\vec{s}_2]}\Omega_{miss}$ between the three vertices $\vec{s}_0$, $\vec{s}_1$ and $\vec{s}_2$ such that:

$$\Omega_{\vec{s}_0,[\vec{s}_0\vec{s}_1\vec{s}_2]} + \Omega_{\vec{s}_1,[\vec{s}_0\vec{s}_1\vec{s}_2]} + \Omega_{\vec{s}_2,[\vec{s}_0\vec{s}_1\vec{s}_2]} = f_{[\vec{s}_0\vec{s}_1\vec{s}_2]}\Omega_{miss} \tag{3.28}$$

where

$$\Omega_{\vec{s}_0,[\vec{s}_0\vec{s}_1\vec{s}_2]} = \frac{\phi_{12}}{48}\left(7\psi_1 + 7\psi_2 - \frac{\psi_1^2}{\psi_2} - \frac{\psi_2^2}{\psi_1}\right)\frac{\Omega_{miss}}{\Omega_{\vec{s}_0}} \tag{3.29a}$$

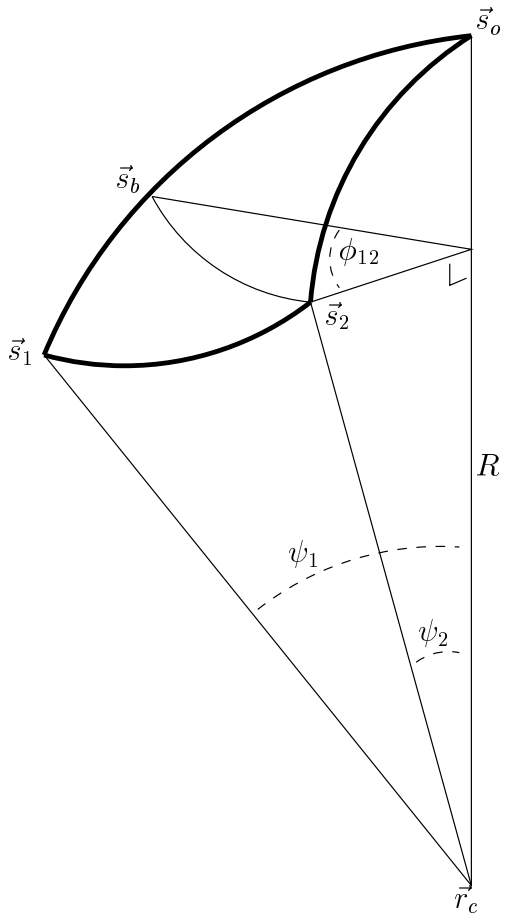

Figure 3.9: Autosolid angle approximation: The triangle defined by the triplet $[\vec{s}_0\vec{s}_1\vec{s}_2]$ is approximated by a portion of a sphere. The solid angle subtended at $\vec{s}_0$ by the curved surface (bold line) can be calculated using the spherical coordinates of $\vec{s}_1$ and $\vec{s}_2$: ψ_1, ψ_2 and ϕ_{12}.

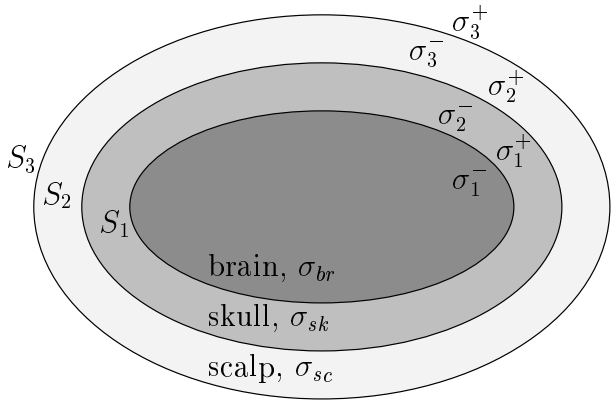

Figure 3.10: Simplified realistic head model : Three concentric volumes of homogeneous conductivity, brain (σ_{br}), skull (σ_{sk}) and scalp (σ_{sc}), separated by the three surfaces S_1, S_2 and S_3, are used as head model.

$$\Omega_{\vec{s}_1,[\vec{s}_0\vec{s}_1\vec{s}_2]} = \frac{\phi_{12}}{48}\left(3\psi_1 + 2\psi_2 + \frac{\psi_2^2}{\psi_1}\right)\frac{\Omega_{miss}}{\Omega_{\vec{s}_0}} \tag{3.29b}$$

$$\Omega_{\vec{s}_2,[\vec{s}_0\vec{s}_1\vec{s}_2]} = \frac{\phi_{12}}{48}\left(2\psi_1 + 3\psi_2 + \frac{\psi_1^2}{\psi_2}\right)\frac{\Omega_{miss}}{\Omega_{\vec{s}_0}} \tag{3.29c}$$

These approximations for the CPV and LPV auto-solid angle were employed in the implementation of the BEM solution.

3.3 Matrix form of the BEM equation

3.3.1 Simple realistic head model

For the simplified head model, three concentric volumes of homogeneous conductivity are considered : the brain, skull and scalp volumes, of respective conductivity σ_{br}, σ_{sk} and σ_{sc}, as depicted in figure 3.10. The three interfaces : "brain-skull", "skull-scalp" and "scalp-air" separating the three volumes are numbered respectively 1, 2 and 3. With this numbering convention, the conductivity inside and outside each surface is defined by :

$$\begin{array}{rcccc} & & \sigma_1^- & = & \sigma_{br} \\ \sigma_1^+ & = & \sigma_2^- & = & \sigma_{sk} \\ \sigma_2^+ & = & \sigma_3^- & = & \sigma_{sc} \\ \sigma_3^+ & = & & & 0 \end{array} \tag{3.30}$$

3.3.2 Matrix form

With the discrete approximation of the source term (equation 3.6) and the approximation of the boundary element equation : CoG approximation (equation 3.9), CPV approximation (equation 3.11) or LPV approximation (equation 3.14) adopted in section 3.2, the

BEM problem can be expressed under a matrix form:

$$\begin{bmatrix} \mathbf{v}_1 \\ \mathbf{v}_2 \\ \mathbf{v}_3 \end{bmatrix} = \begin{bmatrix} \mathbf{B}_{11} & \mathbf{B}_{12} & \mathbf{B}_{13} \\ \mathbf{B}_{21} & \mathbf{B}_{22} & \mathbf{B}_{23} \\ \mathbf{B}_{31} & \mathbf{B}_{32} & \mathbf{B}_{33} \end{bmatrix} \begin{bmatrix} \mathbf{v}_1 \\ \mathbf{v}_2 \\ \mathbf{v}_3 \end{bmatrix} + \begin{bmatrix} \mathbf{G}_1 \\ \mathbf{G}_2 \\ \mathbf{G}_3 \end{bmatrix} [\,\mathbf{j}\,] \tag{3.31}$$

or, in a reduced version,

$$\mathbf{v} = \mathbf{B}\,\mathbf{v} + \mathbf{G}\,\mathbf{j} \tag{3.32}$$

where:

- $\mathbf{v}_k$, a $N_{v_k} \times 1$ vector, contains the value of the potential at the N_{v_k} nodal points of surface S_k: centre of gravity of each triangle for the CoG approximation or vertices of the triangles for the CPV and LPV approximations.
- $\mathbf{B}_{kl}$, a $N_{v_k} \times N_{v_l}$ matrix, represents the influence of the potential of surface S_l on the potential of surface S_k. Its elements depend on the conductivity inside and outside the surfaces S_k and S_l, and on the solid angles used in the BEM approximations 3.9. $\mathbf{B}$ is a $N_v \times N_v$ matrix with $N_v = N_{v_1} + N_{v_2} + N_{v_3}$.
- $\mathbf{j} = [\,\vec{j}_1{}^t\ \vec{j}_2{}^t\ \dots\ \vec{j}_{N_j}{}^t\,]^t$, a $3N_j \times 1$ vector, is the source distribution vector where each $\vec{j}_n = [\,j_{n,x}\ j_{n,y}\ j_{n,z}\,]^t$ is an orientation-free source vector.
- $\mathbf{G}_k$, a $N_{v_k} \times 3N_j$ matrix, is the free space potential matrix depending on the location $\vec{r}_n$ of the sources $\vec{j}_n$, the nodal points on surface S_k and the conductivity inside and outside surface S_k (σ_k^- and σ_k^+). $\mathbf{G}$ is a $N_v \times 3N_j$ matrix.

Self influence matrix B

For the CoG approximation, the element (p,q) of the matrix $\mathbf{B}_{kl}$ is calculated by:

$$\mathbf{B}_{kl}^{(p,q)} = \frac{1}{2\pi}\left(\frac{\sigma_l^- - \sigma_l^+}{\sigma_k^- + \sigma_k^+}\right)\Omega_{pq} \tag{3.33}$$

where

- p (resp. q) is the index of the nodal point on the surface S_k (resp. S_l).
- Ω_{pq} is the solid angle at the centre of gravity of the p^{th} triangle of S_k subtended by the q^{th} triangle of S_l.

For the CPV approximation, the element (p,q) of the matrix $\mathbf{B}_{kl}$ is calculated by:

$$\mathbf{B}_{kl}^{(p,q)} = \frac{1}{2\pi}\left(\frac{\sigma_l^- - \sigma_l^+}{\sigma_k^- + \sigma_k^+}\right)\sum_n^{N_q}\frac{\Omega_{pn}}{3} \tag{3.34}$$

where

- p (resp. q) is the index of the nodal point on the surface S_k (resp. S_l).
- N_q is the number of triangles comprising the q^{th} vertex.
- Ω_{pn} is the solid angle at the p^{th} vertex of the surface S_k subtended by the n^{th} triangle (containing the q^{th}vertex) of S_l.

For the LPV approximation, the element (p, q) of the matrix $\mathbf{B}_{kl}$ is calculated by :

$$\mathbf{B}_{kl}^{(p,q)} = \frac{1}{2\pi}\left(\frac{\sigma_l^- - \sigma_l^+}{\sigma_k^- + \sigma_k^+}\right)\sum_n^{N_q}\Omega_{pn}^q \tag{3.35}$$

where

- p (resp. q) is the index of the nodal point on the surface S_k (resp. S_l).
- N_q is the number of triangles comprising the q^{th} vertex.
- Ω_{pn}^q is the portion of solid angle attributed to the q^{th} vertex, and subtended by the n^{th} triangle (containing the q^{th} vertex) of S_l at the p^{th} vertex of the surface S_k.

Note that the correction for the auto-solid angle problem can only be performed **after** calculating all the solid angles relative to one nodal point because the missing solid angle Ω_{miss} is estimated by equation 3.22. When Ω_{miss} is calculated, then the procedure presented in section 3.2.3 can easily be applied for the CPV and LPV approximations.

Free potential matrix $\mathbf{G}_k$

The elements $(p, 3q-2)$, $(p, 3q-1)$ and $(p, 3q)$ of the matrix $\mathbf{G}_k$ can be calculated with :

$$\left[\mathbf{G}_k^{(p,3q-2)}\ \mathbf{G}_k^{(p,3q-1)}\ \mathbf{G}_k^{(p,3q)}\right] = \frac{(\vec{s}_p - \vec{r}_q)^t}{2\pi(\sigma_k^- + \sigma_k^+)|\vec{s}_p - \vec{r}_q|^3} \tag{3.36}$$

where

- $\vec{s}_p$ is the p^{th} nodal point of the surface S_k.
- $\vec{r}_q$ is the location of the q^{th} current source $\vec{j}_q$.

Interpretation

The $N_v \times N_v$ matrix $\mathbf{B}$ can be interpreted as a "self influence" matrix : the potential at any nodal point on any surface is influenced by the potential at all the other nodal points on all the surfaces. The $N_v \times 3N_j$ matrix $\mathbf{G}$ is, on the contrary, the "direct influence" matrix : in free space, the potential at any nodal point on any surface depends only on the source distribution $\mathbf{j}$. The matrices $\mathbf{B}$ and $\mathbf{G}$ can be calculated separately and they depend solely on the geometry of the problem and the conductivity adopted for each volume. Any change in the geometry or the conductivity implies the recalculation of these matrices.

The number and placement of triangles determines how well the true surface is approximated by the set of plane triangles. The choice of the potential approximation on each triangle determines how well the real potential is approximated but also how the matrices $\mathbf{B}$ and $\mathbf{G}$ are calculated and therefore the number of equations to be solved. For a tessellated closed surface there are about twice as many triangles than vertices. Thus with the

same head model, there will be twice as many equations to solve if the CoG approximation is used than with the CPV or LPV approximation. The LPV approximation is also the only one that ensures a continuous variation of the electric potential from one triangle to the next on the surfaces.

3.4 Solving the matrix BEM equation

The solution of the forward problem consists now in establishing a linear relationship between the source distribution $\mathbf{j}$ and the potential on the surfaces $\mathbf{v}$ (or at least on the scalp $\mathbf{v}_3$) of the form:

$$\mathbf{v} = \mathbf{L}\,\mathbf{j} \tag{3.37}$$

An obvious solution of equation 3.32 would be to simply solve the system of equations:

$$(\mathbf{I}_{N_v} - \mathbf{B})\ \mathbf{v} = \mathbf{G}\ \mathbf{j} \tag{3.38}$$

by inverting the matrix $(\mathbf{I}_{N_v} - \mathbf{B})$. However we are dealing here with a problem of electric potential and a potential function can only be measured relative to some reference point, i.e. calculated to within a constant. The systems of equations 3.38 is therefore rank deficient and the matrix $(\mathbf{I}_{N_v} - \mathbf{B})$ **cannot** be inverted, as explained below.

As $\mathbf{v}_a = \mathbf{v}$ and $\mathbf{v}_b = \mathbf{v} + c\,\mathbf{1}_{N_v}$ (with $c \neq 0$) must both satisfy 3.32 and 3.38, it follows:

$$\left.\begin{array}{rcl} \mathbf{v} & = & \mathbf{B}\,\mathbf{v} + \mathbf{G}\,\mathbf{j} \\ (\mathbf{v} + c\,\mathbf{1}_{N_v}) & = & \mathbf{B}\,(\mathbf{v} + c\,\mathbf{1}_{N_v}) + \mathbf{G}\,\mathbf{j}, \quad c \neq 0 \end{array}\right\} \Rightarrow \quad c\,\mathbf{1}_{N_v} = \mathbf{B}\,c\,\mathbf{1}_{N_v}, \quad c \neq 0$$

$$\Rightarrow \quad \mathbf{B}\,\mathbf{1}_{N_v} = \mathbf{1}_{N_v}$$

$$\Rightarrow \quad (\mathbf{I}_{N_v} - \mathbf{B})\,\mathbf{1}_{N_v} = 0$$

The matrix $(\mathbf{I}_{N_v} - \mathbf{B})$ has a **null** eigenvalue associated with the eigenvector $\mathbf{1}_{N_v}$, i.e $\mathbf{B}$ has a **unit** eigenvalue associated with the eigenvector $\mathbf{1}_{N_v}$. The only way to solve 3.38 is to use a "deflation technique" (Lynn & Timlake, 1968a,b; Chan, 1984).

3.4.1 Deflation technique

By assuming that the unit eigenvalue of $\mathbf{B}$ is simple, it can easily be shown that any other solution will only differ by an additive constant, that is, a scalar multiple of $\mathbf{1}_{N_v}$. Let $\mathbf{p}$ be any vector such that $\mathbf{1}_{N_v}^t\ \mathbf{p} = 1$ and suppose that we seek the solution of 3.32 such that $\mathbf{p}^t\,\mathbf{v} = 0$. Then looking for this particular solution, equation 3.32 becomes:

$$\mathbf{v} = (\mathbf{B} - \mathbf{1}_{N_v}\,\mathbf{p}^t)\,\mathbf{v} + \mathbf{G}\,\mathbf{j} \tag{3.39}$$

Under the assumption that $\mathbf{p}^t\,\mathbf{v} = 0$, the matrix $\mathbf{C} = (\mathbf{B} - \mathbf{1}_{N_v}\,\mathbf{p}^t)$ is a deflation of $\mathbf{B}$ and has no unit eigenvalue, so that $(\mathbf{I}_{N_v} - \mathbf{C})^{-1} = (\mathbf{I}_{N_v} - \mathbf{B} - \mathbf{1}_{N_v}\,\mathbf{p}^t)^{-1}$ exists. Equation 3.31 can be rewritten like

$$\begin{bmatrix} \mathbf{v}_1 \\ \mathbf{v}_2 \\ \mathbf{v}_3 \end{bmatrix} = \begin{bmatrix} \mathbf{C}_{11} & \mathbf{C}_{12} & \mathbf{C}_{13} \\ \mathbf{C}_{21} & \mathbf{C}_{22} & \mathbf{C}_{23} \\ \mathbf{C}_{31} & \mathbf{C}_{32} & \mathbf{C}_{33} \end{bmatrix} \begin{bmatrix} \mathbf{v}_1 \\ \mathbf{v}_2 \\ \mathbf{v}_3 \end{bmatrix} + \begin{bmatrix} \mathbf{G}_1 \\ \mathbf{G}_2 \\ \mathbf{G}_3 \end{bmatrix} [\mathbf{j}] \tag{3.40}$$

and this system of equations can be solved by calculating:

$$\mathbf{v} = (\mathbf{I}_{N_v} - \mathbf{C})^{-1}\,\mathbf{G}\,\mathbf{j} \tag{3.41a}$$
$$= (\mathbf{I}_{N_v} - \mathbf{B} - \mathbf{1}_{N_v}\,\mathbf{p}^t)^{-1}\,\mathbf{G}\,\mathbf{j} \tag{3.41b}$$

where $\mathbf{v}$ will satisfy $\mathbf{p}^t\,\mathbf{v} = 0$.

Each vector $\mathbf{v}_\bullet$ is of size $N_{v_\bullet} \times 1$, so if, for example, $\mathbf{p}$ is defined by:

$$\mathbf{p} = [\underbrace{0\,0\,\ldots\,0}_{N_{v_1}}\ \underbrace{0\,0\,\ldots\,0}_{N_{v_2}}\ \underbrace{p\,p\,\ldots\,p}_{N_{v_3}}]^t \tag{3.42}$$

with $p = 1/N_{v3}$, then $\mathbf{p}^t\,\mathbf{v} = 0$ simply means that the mean of $\mathbf{v}_3$ is zero. Therefore equation 3.41 provides us with the solution that is mean corrected over the scalp surface.

3.4.2 Partial solution for the scalp

The number of equations (N_v) to solve in 3.40 is rather large, but only the direct relationship between the source distribution $\mathbf{j}$ and the potential on the scalp $\mathbf{v}_3$ is of interest in the EEG problem. After some algebraic manipulations, equation 3.40 can be rewritten like this:

$$\mathbf{\Gamma}_1\,\mathbf{v}_3 = \mathbf{\Gamma}_2\,\mathbf{j} \tag{3.43}$$

where

$$\begin{aligned}\mathbf{\Gamma}_1 = {} & -(\mathbf{C}_{33} - \mathbf{I}_{N_{v_3}}) \\ & -\mathbf{C}_{31}\left[(\mathbf{C}_{11} - \mathbf{I}_{N_{v_1}}) - \mathbf{C}_{12}(\mathbf{C}_{22} - \mathbf{I}_{N_{v_2}})^{-1}\mathbf{C}_{21}\right]^{-1}\left[\mathbf{C}_{12}(\mathbf{C}_{22} - \mathbf{I}_{N_{v_2}})^{-1}\mathbf{C}_{23} - \mathbf{C}_{13}\right] \\ & -\mathbf{C}_{32}\left[(\mathbf{C}_{22} - \mathbf{I}_{N_{v_2}}) - \mathbf{C}_{21}(\mathbf{C}_{11} - \mathbf{I}_{N_{v_1}})^{-1}\mathbf{C}_{12}\right]^{-1}\left[\mathbf{C}_{21}(\mathbf{C}_{11} - \mathbf{I}_{N_{v_1}})^{-1}\mathbf{C}_{13} - \mathbf{C}_{23}\right]\end{aligned} \tag{3.44}$$

and

$$\begin{aligned}\mathbf{\Gamma}_2 = {} & \mathbf{G}_3 \\ & +\mathbf{C}_{31}\left[(\mathbf{C}_{11} - \mathbf{I}_{N_{v_1}}) - \mathbf{C}_{12}(\mathbf{C}_{22} - \mathbf{I}_{N_{v_2}})^{-1}\mathbf{C}_{21}\right]^{-1}\left[\mathbf{C}_{12}(\mathbf{C}_{22} - \mathbf{I}_{N_{v_2}})^{-1}\mathbf{G}_2 - \mathbf{G}_1\right] \\ & +\mathbf{C}_{32}\left[(\mathbf{C}_{22} - \mathbf{I}_{N_{v_2}}) - \mathbf{C}_{21}(\mathbf{C}_{11} - \mathbf{I}_{N_{v_1}})^{-1}\mathbf{C}_{12}\right]^{-1}\left[\mathbf{C}_{21}(\mathbf{C}_{11} - \mathbf{I}_{N_{v_1}})^{-1}\mathbf{G}_1 - \mathbf{G}_2\right]\end{aligned} \tag{3.45}$$

In order to reduce the number of operations required to calculate $\mathbf{\Gamma}_1$ and $\mathbf{\Gamma}_2$ in 3.44 and 3.45, these relations can be expressed using some common "intermediate matrices" $\mathbf{\Upsilon}_i$:

$$\mathbf{\Gamma}_1 = -\left((\mathbf{C}_{33} - \mathbf{I}_{N_{v_3}}) + \mathbf{\Upsilon}_5\,\mathbf{C}_{13} + \mathbf{\Upsilon}_6\,\mathbf{C}_{23}\right) \tag{3.46a}$$
$$\mathbf{\Gamma}_2 = \mathbf{G}_3 + \mathbf{\Upsilon}_5\,\mathbf{G}_1 + \mathbf{\Upsilon}_6\,\mathbf{G}_2 \tag{3.46b}$$

where

$$\mathbf{\Upsilon}_6 = \mathbf{\Upsilon}_4\,\mathbf{\Upsilon}_2 - \mathbf{\Upsilon}_3 \tag{3.47a}$$
$$\mathbf{\Upsilon}_5 = \mathbf{\Upsilon}_3\,\mathbf{\Upsilon}_1 - \mathbf{\Upsilon}_4 \tag{3.47b}$$
$$\mathbf{\Upsilon}_4 = \mathbf{C}_{31}\left(-\mathbf{\Upsilon}_2\,\mathbf{C}_{21} + (\mathbf{C}_{11} - \mathbf{I}_{N_{v_1}})\right)^{-1} \tag{3.47c}$$
$$\mathbf{\Upsilon}_3 = \mathbf{C}_{32}\left(-\mathbf{\Upsilon}_1\,\mathbf{C}_{12} + (\mathbf{C}_{22} - \mathbf{I}_{N_{v_2}})\right)^{-1} \tag{3.47d}$$
$$\mathbf{\Upsilon}_2 = \mathbf{C}_{12}\left(\mathbf{C}_{22} - \mathbf{I}_{N_{v_2}}\right)^{-1} \tag{3.47e}$$
$$\mathbf{\Upsilon}_1 = \mathbf{C}_{21}\left(\mathbf{C}_{11} - \mathbf{I}_{N_{v_1}}\right)^{-1} \tag{3.47f}$$

By proceeding carefully, one has only to solve 4 systems of equations (3.47f, 3.47e, 3.47d and 3.47c) to obtain $\mathbf{\Gamma}_1$ and $\mathbf{\Gamma}_2$. The matrices to invert are only of size N_{v_1} and N_{v_2}, thus the calculation of $\mathbf{\Gamma}_1$ and $\mathbf{\Gamma}_2$ require much less computational effort than inverting directly $\mathbf{C}$, which is of size $N_v = N_{v_1} + N_{v_2} + N_{v_3}$.

The explicit solution for all nodal points on the scalp surface may then be obtained from 3.43 by calculating:

$$\begin{aligned} \mathbf{v}_3 &= \mathbf{\Gamma}_1^{-1}\,\mathbf{\Gamma}_2\,\mathbf{j} && \text{(3.48a)} \\ &= \mathbf{L}\,\mathbf{j} && \text{(3.48b)} \end{aligned}$$

Where $\mathbf{\Gamma}_1$ is only of size N_{v_3}. It would of course be possible to obtain a relation such as 3.43 for the other two surfaces.

It is important to note that $\mathbf{\Gamma}_1$ depends **only** on the matrix $\mathbf{C}$, i.e. on the geometry and the conductivity of the volumes, but not on the source distribution $\mathbf{j}$. By pre-calculating and saving $\mathbf{\Gamma}_1^{-1}$, $\mathbf{\Upsilon}_5$ and $\mathbf{\Upsilon}_6$, the lead field matrix $\mathbf{L}$ can be obtained very easily for any source distribution, using equations 3.46b and 3.48.

3.4.3 Partial solution for the electrode sites

In general it is not necessary to calculate the potential V over the entire scalp surface as, in practical cases, EEG is recorded from a limited number of electrodes. Therefore the lead field for the electrode sites should only be calculated:

$$\mathbf{v}_{3,el} = \mathbf{L}_{el}\,\mathbf{j} \tag{3.49}$$

In a realistic head model, the location of the electrodes is defined relative to the triangular mesh of the scalp. As the electrodes have typically a diameter of a few millimetres, the location of the electrodes can be approximated to the triangle directly underneath. If the CoG approximation was used to model the potential over each triangle, the nodal points for which the lead field should be calculated, are simply the centre of gravity of the triangles under the electrodes. If the CPV or LPV approximation was used, the potential is estimated at the vertices of each triangle. Therefore the lead field for the three vertices of the electrode triangles has to be calculated, and should be combined afterwards to provide a single lead field per electrode. If the electrodes are about the same size as the triangles on the scalp, then a single mean can be used. But, if the electrodes are smaller than the triangles, a linear interpolation between the vertices of the triangle should be preferred.

A partial solution of equation 3.43 for a few nodal points is possible thanks to the Frobenius-Schur formula that allows the partial calculation of the inverse of a matrix:

$$\begin{bmatrix} \mathbf{M} & \mathbf{N} \\ \mathbf{P} & \mathbf{Q} \end{bmatrix}^{-1} = \begin{bmatrix} \mathbf{M}^{-1} + \mathbf{M}^{-1}\mathbf{N}\,\mathbf{F}^{-1}\mathbf{P}\,\mathbf{M}^{-1} & -\mathbf{M}^{-1}\mathbf{N}\,\mathbf{F}^{-1} \\ -\mathbf{F}^{-1}\mathbf{P}\,\mathbf{M}^{-1} & \mathbf{F}^{-1} \end{bmatrix} \tag{3.50}$$

where: $\begin{cases} \mathbf{M} \text{ and } \mathbf{Q} \text{ must be square.} \\ \mathbf{M} \text{ and } \mathbf{F} = \mathbf{Q} - \mathbf{P}\,\mathbf{M}^{-1}\mathbf{N} \text{ must be invertible.} \end{cases}$

Considering that the N_{el} interesting (respectively, N_{ot} other) nodal points are the last N_{el} (respectively, first N_{ot}) elements of $\mathbf{v}_3$: $\mathbf{v}_3 = [\mathbf{v}_{3,ot}^t \; \mathbf{v}_{3,el}^t]^t$, then equation 3.43 can be rewritten like this :

$$\underbrace{\left[\begin{array}{c|c} \mathbf{M} & \mathbf{N} \\ \hline \mathbf{P} & \mathbf{Q} \end{array}\right]}_{\mathbf{\Gamma}_1} \underbrace{\left[\begin{array}{c} \mathbf{v}_{3,ot} \\ \hline \mathbf{v}_{3,el} \end{array}\right]}_{\mathbf{v}_3} = \underbrace{\left[\begin{array}{c} \mathbf{R} \\ \hline \mathbf{S} \end{array}\right]}_{\mathbf{\Gamma}_2} \left[\begin{array}{c} \mathbf{j} \end{array}\right] \tag{3.51}$$

$$\Rightarrow \underbrace{\left[\begin{array}{c} \mathbf{v}_{3,ot} \\ \hline \mathbf{v}_{3,el} \end{array}\right]}_{\mathbf{v}_3} = \underbrace{\left[\begin{array}{c|c} \mathbf{M}^{-1} + \mathbf{M}^{-1}\mathbf{N}\,\mathbf{F}^{-1}\mathbf{P}\,\mathbf{M}^{-1} & -\mathbf{M}^{-1}\mathbf{N}\,\mathbf{F}^{-1} \\ \hline -\mathbf{F}^{-1}\mathbf{P}\,\mathbf{M}^{-1} & \mathbf{F}^{-1} \end{array}\right]}_{\mathbf{\Gamma}_1^{-1}} \underbrace{\left[\begin{array}{c} \mathbf{R} \\ \hline \mathbf{S} \end{array}\right]}_{\mathbf{\Gamma}_2} \left[\begin{array}{c} \mathbf{j} \end{array}\right] \tag{3.52}$$

This partitioning of the vertices is not natural (as the electrodes are spread over the scalp surface) but such ordering may be easily obtained by adequately permuting the rows and columns in $\mathbf{\Gamma}_1$ and $\mathbf{\Gamma}_2$.

As only the bottom part of equation 3.52 is of interest, the lead field for the electrode sites can be obtained from the submatrices of $\mathbf{\Gamma}_1$ and $\mathbf{\Gamma}_2$ by :

$$\mathbf{L}_{el} = \left[\begin{array}{cc} -\mathbf{F}^{-1}\mathbf{P}\,\mathbf{M}^{-1} & \mathbf{F}^{-1} \end{array}\right] \left[\begin{array}{c} \mathbf{R} \\ \mathbf{S} \end{array}\right] \tag{3.53}$$

and only the two matrices $\mathbf{F}$ and $\mathbf{M}$ have to be inverted. The number N_{el} of electrode sites being much smaller than the number of nodal points on the scalp surface N_{v_3}, the time spent to calculate $\mathbf{F}^{-1}$ is negligible compared to $\mathbf{M}^{-1}$.

By using the simplified expression 3.46b for $\mathbf{\Gamma}_2$, equation 3.53 becomes :

$$\begin{aligned} \mathbf{L}_{el} &= \left[\begin{array}{cc} -\mathbf{F}^{-1}\mathbf{P}\,\mathbf{M}^{-1} & \mathbf{F}^{-1} \end{array}\right] (\mathbf{\Upsilon}_5\,\mathbf{G}_1 + \mathbf{\Upsilon}_6\,\mathbf{G}_2 + \mathbf{G}_3) && \text{(3.54a)} \\ &= \mathbf{\Xi}_1\,\mathbf{G}_1 + \mathbf{\Xi}_2\,\mathbf{G}_2 + \mathbf{\Xi}_3\,\mathbf{G}_3 && \text{(3.54b)} \end{aligned}$$

where

$$\begin{aligned} \mathbf{\Xi}_1 &= \left[\begin{array}{cc} -\mathbf{F}^{-1}\mathbf{P}\,\mathbf{M}^{-1} & \mathbf{F}^{-1} \end{array}\right] \mathbf{\Upsilon}_5 && \text{(3.55a)} \\ \mathbf{\Xi}_2 &= \left[\begin{array}{cc} -\mathbf{F}^{-1}\mathbf{P}\,\mathbf{M}^{-1} & \mathbf{F}^{-1} \end{array}\right] \mathbf{\Upsilon}_6 && \text{(3.55b)} \\ \mathbf{\Xi}_3 &= \left[\begin{array}{cc} -\mathbf{F}^{-1}\mathbf{P}\,\mathbf{M}^{-1} & \mathbf{F}^{-1} \end{array}\right] && \text{(3.55c)} \end{aligned}$$

The three matrices $\mathbf{\Xi}_1$, $\mathbf{\Xi}_2$ and $\mathbf{\Xi}_3$ depend **only** on the geometry and conductivity of the head model. If they are pre-calculated (and saved), the lead field $\mathbf{L}_{el}$ can be rapidly calculated for any source distribution $\mathbf{j}$ using equation 3.54. This is of particular interest if the location of the dipoles has to be modified, for example, if a denser mesh of dipoles is required in a linear distributed solution, or if an iterative procedure is used to optimise the location of the ECDs in a ECD-based solution.

Chapter 4

Validation and application of the BEM solution

Contents

4.1 Model for validation

The only way to validate the BEM solution, which is a numerical approximate solution of Maxwell's equations, is to compare it with an exact analytical solution. As previously noted an analytical solution of equation 2.7 can only be calculated for particular geometries and conductivity layouts. One such model is the "three sphere shell" model, consisting of three concentric spheres of homogeneous and isotropic conductivity. The explicit analytical solution can be obtained by the formula presented in appendix B.

To render the three sphere shell model more realistic, i.e. more like a real head, the three radii and conductivity constants were chosen such that: The "brain" is an homogeneous sphere of radius $r_1 = 0.8$ and conductivity $\sigma_1 = 1$, the "skull" is a thin layer volume (between radii $r_1 = 0.8$ and $r_2 = 0.9$) of poor conductivity $\sigma_2 = 0.01$ (100 times smaller than the conductivity of the "brain" and "scalp" volumes), and the "scalp" is the outer layer volume (between radii $r_2 = 0.9$ and $r_3 = 1.0$) with the same conductivity as the "brain" volume ($\sigma_3 = 1$). The three sphere shell model is pictured in figure 4.1. The analytical solution $\mathbf{L}_{\text{ana}}$ of the forward problem for the three sphere shell model was calculated for a fixed set of dipoles. Within the brain volume, dipoles oriented according to the three main axes ($\vec{e}_x$, $\vec{e}_y$ and $\vec{e}_z$) were spread on a uniform three-dimensional grid at 2983 locations, providing with 8949 independent current sources of various orientation and eccentricity.

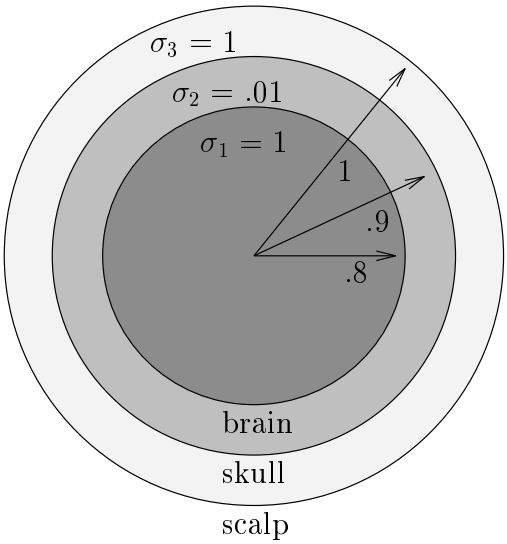

Figure 4.1: The "three sphere shell" model is defined for the "brain", "skull" and "scalp" volumes by the constants: radii $r_1 = .8$, $r_2 = .9$ and $r_3 = 1.0$, and conductivity $\sigma_1 = 1$, $\sigma_2 = 0.01$ and $\sigma_3 = 1$.

Table 4.1: Number of triangles, vertices and mean length of the edges of the triangles on the three tessellated surfaces of radius $r_1 = 0.8$, $r_2 = 0.9$ and $r_3 = 1.0$.

number of		mean length of an edge		
triangles	vertices	on S_1	on S_2	on S_3
640	322	0.1731	0.1948	0.2164
1210	607	0.1263	0.1420	0.1578
2560	1282	0.0870	0.0978	0.1087

In order to calculate the lead fields $\mathbf{L}_{\text{num}}$ with the BEM, the three surfaces used in the spherical head model were tessellated into triangles. As stated in section 3.1.2, for the same tessellation, the CoG potential approximation requires twice as many equations as for the CPV and LPV approximations. Three levels of tessellation were used for the simulations: the number of triangles, vertices and the mean length of the triangle edges on the three surfaces (at radius $r_1 = 0.8$, $r_2 = 0.9$ and $r_3 = 1.0$) are summarised in table 4.1.

Two BEM solutions for the CoG method were calculated with the first two densities (640 and 1210 triangles) while the last two densities (607 and 1282 vertices) were used to compute the solutions with the CPV and LPV methods. With these choices of densities, solutions requiring approximately the same computational load (about 5 times 600 or 1200 linear equations to solve, as it can be noticed in equations 3.46 to 3.48) could be compared objectively. The BEM and analytical solutions were calculated for all the nodal points on the "scalp" surface (centre of gravity of the triangles or vertices of the mesh) and for the whole dipole set.

4.2 Validation of BEM

With this choice of parameters the influence on the accuracy of the BEM solution of the density of the tessellation and the approximation used to model the potential on each triangle (CoG, CPV or LPV) could be assessed. Two criteria (Meijs *et al.*, 1989) were employed to validate the BEM solutions:

- the Relative Difference Measure (RDM):

$$\mathrm{RDM} = \sqrt{\frac{\sum_i^N (v_{\mathrm{ana},i} - v_{\mathrm{num},i})^2}{\sum_i^N v_{\mathrm{ana},i}^2}} \tag{4.1}$$

- the Magnification factor (MAG):

$$\mathrm{MAG} = \sqrt{\frac{\sum_i^N v_{\mathrm{num},i}^2}{\sum_i^N v_{\mathrm{ana},i}^2}} \tag{4.2}$$

where $v_{\mathrm{ana},i}$ (resp. $v_{\mathrm{num},i}$) is the potential at the i^{th} nodal point of the scalp surface, calculated analytically (resp. numerically with the BEM). The RDM measures the level of error in the BEM solution compared to the exact analytical solution. It should be as small as possible. The MAG factor measures the relative power of the potential distribution on the scalp between the BEM and analytical solution. It should be equal to 1, but a MAG factor different from 1 is alright as long as it remains constant for all the dipoles.

4.2.1 Simple model

The RDM and MAG were calculated for all the dipole locations and orientations. The results obtained for the CoG, CPV and LPV methods with (about) 600 and 1200 nodal points are summarised in figure 4.2, the mean RDM and MAG is plotted versus the eccentricity of the dipoles.

For the three approximations, the increase in nodal points per surface (from about 600 to 1200) showed a clear improvement in the accuracy of the solution, more triangles ensure a better model. In general the level of error remained stable for sources with small eccentricity but, when the distance between the dipole and the surface is similar to the length of the triangle edges modelling the brain surface (as indicated in table 4.1), the error suddenly increases dramatically. In all cases, the CPV method had the largest error and seemed to be the less efficient solution.

For deep sources, the CoG method gives better results than the LPV method but for shallow sources CoG errors increased much more than LPV error. The potential distribution on the surfaces cannot be approximated accurately any more because the triangles are proportionaly too large compared to the rapid variation of the potential on the surfaces. A linear approximation (LPV method) is still more accurate than a constant approximation (CoG method) and there are more triangles to model the surface (thus the triangles are smaller) for the LPV approximation than for the CoG approximation.

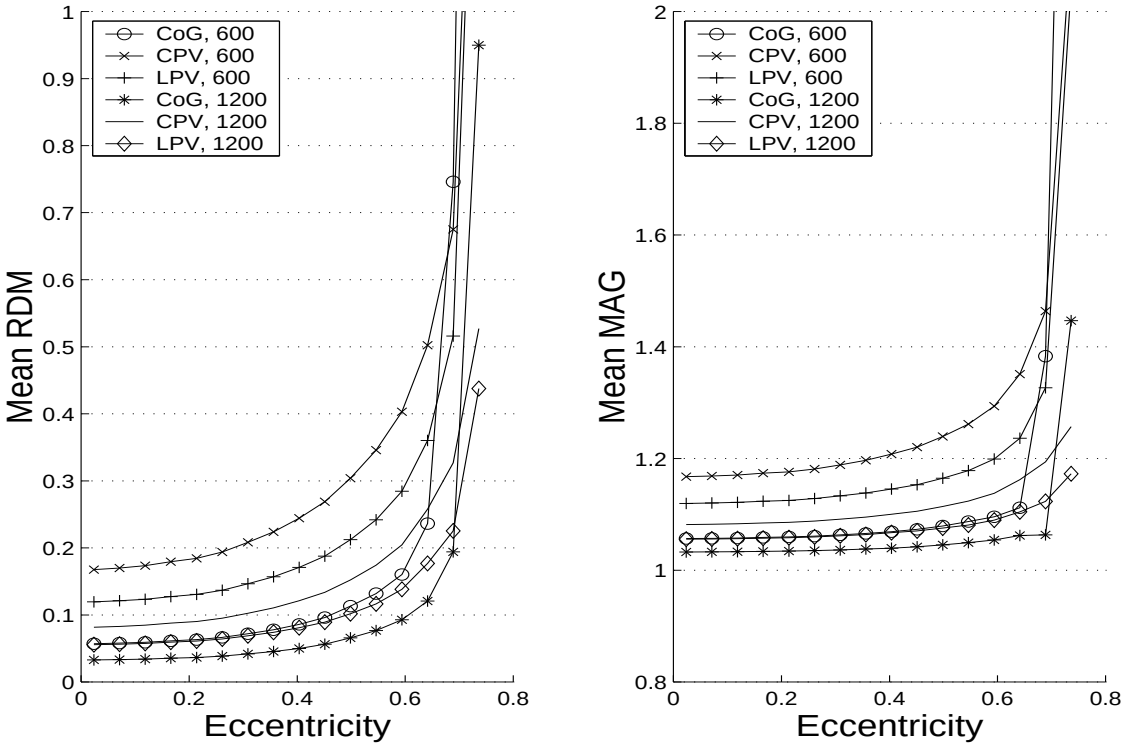

Figure 4.2: Mean Relative Difference Measure (RDM), left, and mean Magnification factor (MAG), right, versus the eccentricity of the dipoles: The three potential approximations, CoG, CPV and LPV, are compared for two levels of computational load, about 600 or 1200 nodal points per surface.

4.2.2 Refined model

Because of the low conductivity of the skull volume (100 times smaller than the brain and the scalp volumes), the potential distribution on the brain surface is mostly dictated by the underneath sources but, as the sources can be close to the brain surface, the error committed at that level can be large. For computational reasons, the number of triangles on each surface (dictating the number of equations to solve) is limited and cannot be increased indefinitely to reduce the numerical errors of the BEM solutions. Nonetheless, as the brain surface is closer to the sources than to the 2 other surfaces, a refined tessellation of the brain surface was used to further improve the BEM solution : While the potential distribution was calculated on (about) 600 or 1200 nodal points for the skull and scalp surfaces, (about) 1200 or 2400 nodal points were used for the brain surface. The results obtained with these "refined 600 (or 1200) nodes models" for the CoG and LPV approximations are presented in figure 4.3.

The finer tessellation of the brain surface reduced significantly the RDM. For the CoG approximation, the refined 600 nodes model gives results almost as good as the non-refined 1200 nodes model and the error for eccentric sources is greatly reduced with the refined 1200 nodes model. For the LPV approximation, the refined 600 nodes model is even better than the non-refined 1200 nodes model. With the refined 1200 nodes model, the MAG factor for both CoG and LPV approximations is closer to 1 and more stable through all the eccentricities. The refined and non-refined 1200 nodes model for the CoG and LPV approximations are compared in figure 4.4.

For the refined head model, both CoG and LPV approximations have very similar degrees of error. The RDM still increased for shallow sources but much less than that of any other model and/or approximation tested. The MAG factor was very close to 1 and almost constant for all eccentricities.

4.3 Conclusion

From the results obtained in the previous section, a few conclusions can be drawn. Obviously the tessellation of the surfaces should be as dense as possible, within the limits of a realistic computational load. For example, to divide, on average, by two the length of the triangle edges, it is necessary to multiply the number of triangles (and vertices) by four, therefore increasing the computational load by a factor 64! As shown in section 4.2.2, it is usually sufficient to increase the number of vertices on the brain surface to achieve a significant improvement of the solution accuracy.

The CPV approximation of potential over the triangles has proved to be the less efficient approximation and should not be used. On the contrary the CoG and LPV methods have both similar performance better than the CPV; nevertheless the LPV should be preferred to the CoG for realistic head model for three reasons : 1. There are about twice as many triangles than vertices on a closed tessellated surface, the LPV approximation allows a finer model of the head geometry for the same computational load, i.e. the same number of nodal points where the potential is evaluated. 2. The LPV approximation models the potential continuously on the surfaces, while there are "potential steps" from one triangle

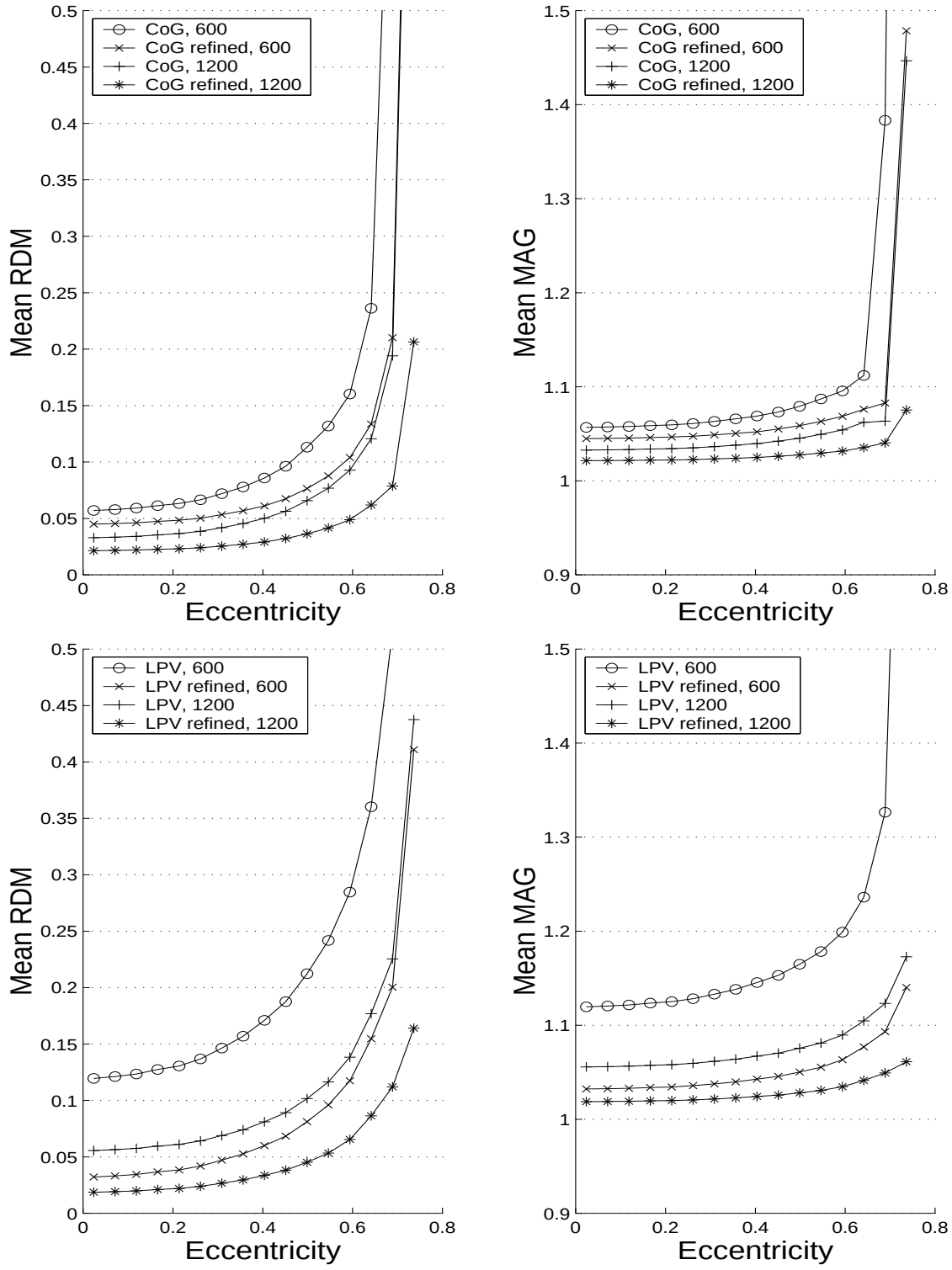

Figure 4.3: Mean RDM (left) and mean MAG (right) versus the eccentricity of the dipoles for the CoG (top) and LPV (bottom) approximations. Four head models are compared : a non-refined model with 600 (or 1200) nodal points on each surface, and a refined model with 1200 (or 2400) nodal points on the brain surface and only 600 (or 1200) for the other 2 surfaces.

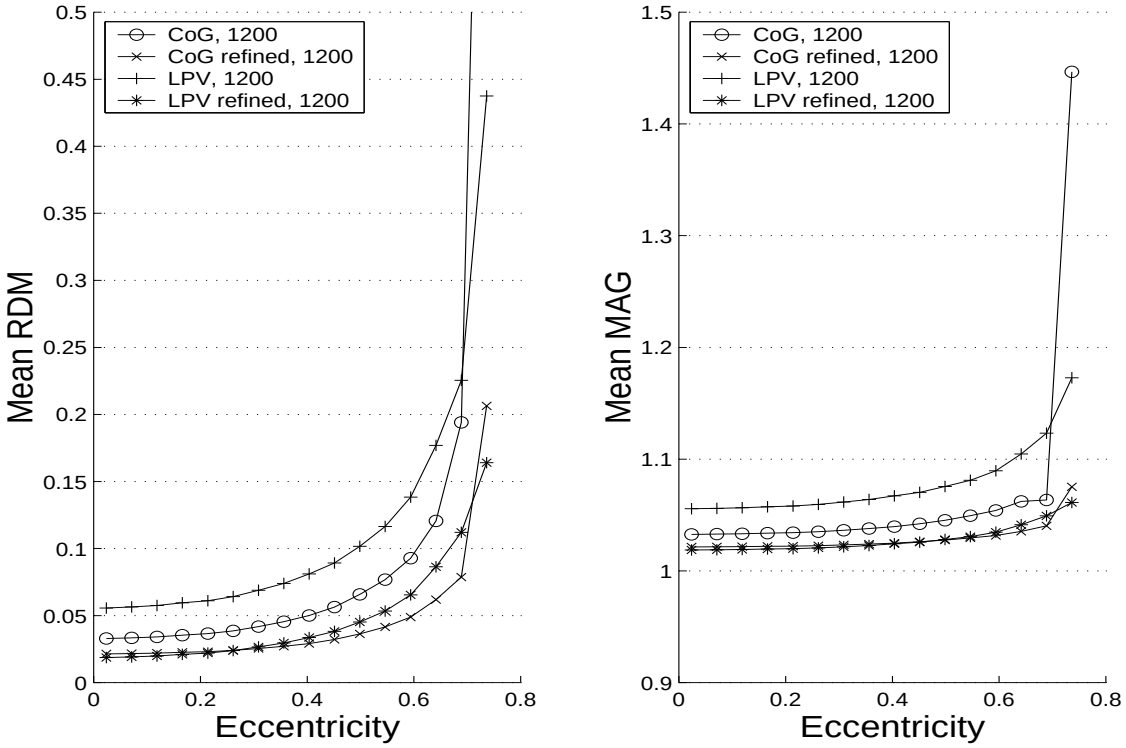

Figure 4.4: Comparison between the CoG and LPV approximations with a refined and non-refined 1200 nodes head model: Mean RDM, left, and mean MAG, right, versus the eccentricity of the dipoles.

Table 4.2: Number of triangles, vertices and mean length of the edges of the triangles on the three tessellated surfaces in the realistic head model.

	Number of triangles	Number of vertices	mean length of an edge [mm]
brain	4559	9114	4.6270
skull	2015	4026	7.6932
scalp	2011	4018	8.9209

to the next when the CoG or CPV approximations are employed. 3. In a realistic head model based on a structural MR image of a patient's head, the surface will not be regular and, as the BEM formulation presented in this work is based on the assumption that the surfaces are smooth, a denser mesh, i.e. the LPV method, should be preferred.

4.4 Application to a realistic head model

In order to use the BEM solution, it is necessary to first establish the head model. The MR image used in this work to build the realistic head model was the template T1 weighted MR image of the SPM99 software package (Wellcome Department of Cognitive Neurology, 1999). This MRI is in the standardised Talairach stereotaxic space of Talairach & Tournoux (1988) and contains $181 \times 217 \times 182$ voxels of size $1 \times 1 \times 1$ mm^3. The image was segmented with the segmentation function of the SPM99 software package (Ashburner & Friston, 1997; Ashburner, 2000; Wellcome Department of Cognitive Neurology, 1999) to generate the outer surfaces of the three main volumes: brain, skull and scalp.

The inner structure of the head is very complicated and almost impossible to model under the eyes' level because of the various cavities and tissues encountered. Fortunately, on a T1 weighted MRI, the brain and scalp surfaces are still readily identifiable. Therefore the lower part of the skull surface was obtained by inflating the brain surface. A few transverse slices with the contour of the brain, skull and scalp volumes are presented in figure 4.5. The surfaces were then tessellated into sets of regular triangles. The number of vertices and triangles and the average length of a triangle's edge are summarised in table 4.2 and the three surfaces are displayed in figure 4.6.

With the head model described, the lead field matrix $\mathbf{L}$ was calculated with the BEM (LPV approximation) for a set of 61 approximately equidistant electrodes, shown on figure 4.7, and 12300 source locations arranged within the brain volume on a regular three-dimensional grid (inter-dipole distance of 4mm). The location and orientation of the dipoles will be defined in section 5.2.1. If the orientation and the amplitude of the sources is left free, three dipoles oriented according to the main axes are assumed at each location and the lead field matrix $\mathbf{L}_f$ obtained is of size 61×36900. Otherwise, if the orientation of the sources is fixed, only the amplitude is left free and the lead field $\mathbf{L}$ is a 61×12300 matrix.

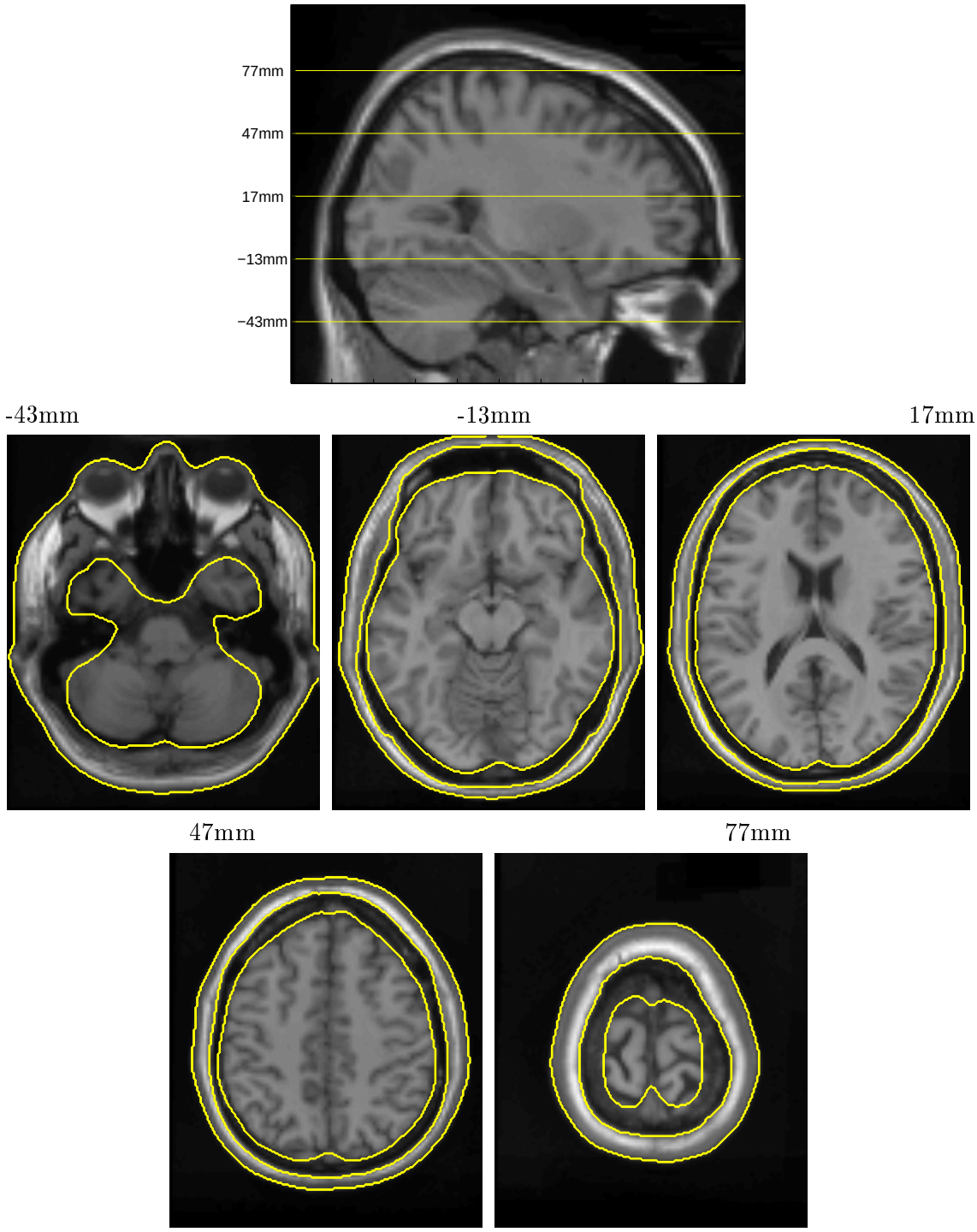

Figure 4.5: Transverse slices of a MR image with the contour of the brain, skull and scalp volumes, at a height of -43mm, -13mm, 17mm, 47mm and 77mm in Talairach space coordinates.

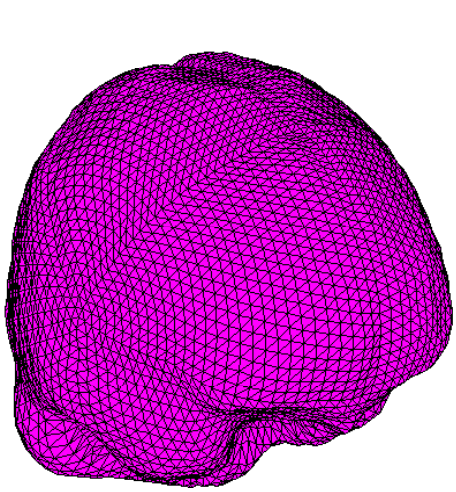

Outer surface of the brain

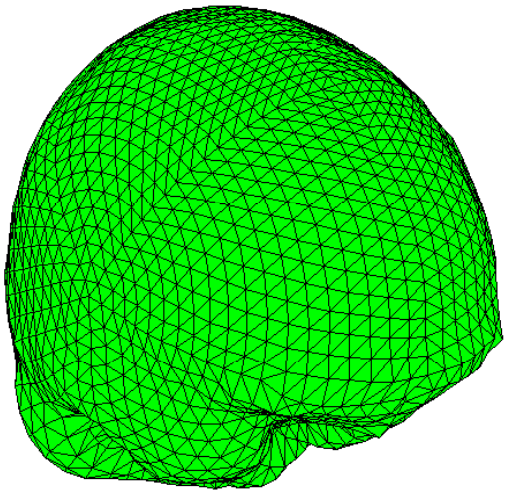

outer surface of the skull

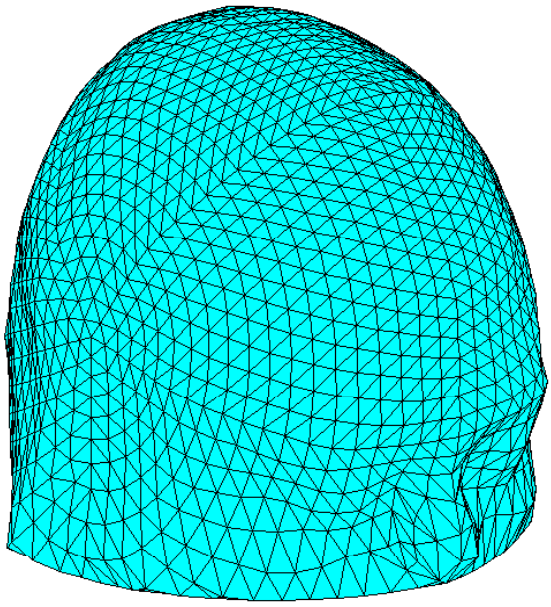

Outer surface of the scalp

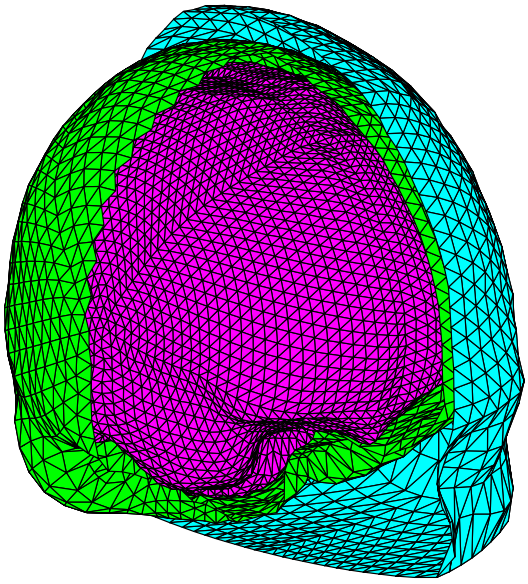

three concentric surfaces

Figure 4.6: Tessellated surface of the brain (top left), the skull (top right) and the scalp (bottom left), and an open view of the three concentric volumes (bottom right).

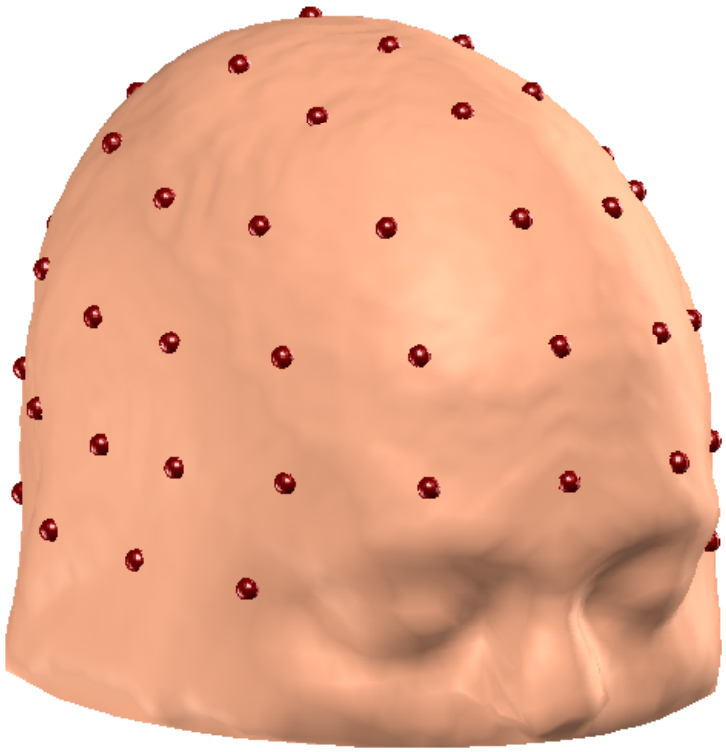

Figure 4.7: Realistic rendering of the scalp surface with the location of the approximately equidistant 61 electrodes.

Part II

Inverse problem

Chapter 5

Constrained minimum norm solution : Theory

Contents

5.1 General approach

In the absence of any *a priori* information, the sources of the EEG signal can be modelled by a fixed, uniform, three-dimensional distribution of current dipoles throughout the entire brain volume. Each current dipole represents the coherent electric activity of the brain over a small cubic volume. Three strong assumptions, based on neuroanatomy, are made about these dipoles : they are located in the the grey matter, their orientation is perpendicular

to the cortical sheet and they are spatially coherent. These constraints are implemented operationally using information extracted from the subject's structural MRI (see section 5.2).

For evoked response EEG (ERP EEG), the data recorded extend over some period of time. Recordings start typically from a few tens to a few hundred milliseconds before the triggering stimulus and last up to a few seconds after the stimulus. The brain activity evoked by the stimulus is thus usually limited to some window of activity. The activity recorded outside this window of activity is basically composed of noise and background activity, i.e. activity that is not elicited by the stimulus. It is therefore useful to estimate the variance-covariance matrix of the recorded noise at the electrode sites. Because of the high sampling rate of EEG, typically of the order of the millisecond, there exists some temporal coherence in the data: the activity at time $t+1$ cannot be completely different from the activity at time t or $t+2$. These three assumptions about the temporal behaviour of the EEG data (window of activity, noise covariance matrix and temporal coherence) are used to further constraints the solution of the inverse problem.

By fixing the orientation of each dipole, the source localisation problem is reduced from a vectorial problem, where both the orientation and the amplitude of the dipoles are unknown, to a scalar problem, where only the amplitudes of the dipoles are unknown. For instantaneous data, the distributed source localisation problem can be stated as:

$$\mathbf{v} + \boldsymbol{\varepsilon} = \mathbf{L}\,\mathbf{j} \tag{5.1}$$

where

- $\mathbf{v}$, the electric potential at the electrodes, is a vector of size $N_e \times 1$,
- $\boldsymbol{\varepsilon}$, the additive noise component, is a vector of size $N_e \times 1$,
- $\mathbf{j}$, the (unknown) amplitude of each current dipole, is a vector of size $N_j \times 1$,
- $\mathbf{L}$, the lead field linking the current sources to the electric potential, is a matrix of size $N_e \times N_j$.

and the orientation of the current dipoles is embodied in the lead field matrix $\mathbf{L}$, so that each element of the vector $\mathbf{j}$ represents only the amplitude of each dipole.

If non-instantaneous data, i.e. a time series of EEG recordings, are considered, the distributed source localisation problem can be stated as:

$$\mathbf{V} + \boldsymbol{\mathcal{E}} = \mathbf{L}\,\mathbf{J} \tag{5.2}$$

where

- $\mathbf{V}$, the electric potential at the electrodes over time, is a matrix of size $N_e \times N_t$,
- $\boldsymbol{\mathcal{E}}$, the additive noise component over time, is a matrix of size $N_e \times N_t$,
- $\mathbf{J}$, the (unknown) amplitude of each current dipole over time, is a matrix of size $N_j \times N_t$,

- **L**, the lead field linking the current sources to the electric potential, is a matrix of size $N_e \times N_j$.

Having fixed the orientation of the dipoles, the two other anatomical assumptions described above, spatial smoothness and location within the grey matter, are used to establish a spatial basis set that models the source distribution (see section 5.3.1). The two anatomical priors enter as constraints on the covariance structure of the source distribution and motivate the selection of the basis set. This set is calculated in a way that maximises the mutual information between the original (and full) source distribution space and the reduced solution space spanned by the basis set.

The inverse of the variance-covariance matrix of the noise is used to whiten the noise at the electrodes, giving more importance to electrodes with small noise variance, and to take into account the covariance between them. Similarly to the anatomical priors, the two other temporal assumptions, window of activity and temporal coherence, are used to establish a temporal basis function set that models the time course of the activity of the sources (see section 5.3.2). This set is motivated and calculated in a similar way to the spatial basis functions.

If other prior knowledge about the location of electric activity is available (e.g. from a functional MRI activation study), it may also help to solve the source localisation problem. This information can be regarded as a soft or probabilistic constraint (compared to the anatomical priors used to determine the spatial basis function set) and therefore enters during the second step of the method, i.e. when the solution (constrained by the basis functions) is actually sought by a weighted minimum L2-norm approach (see section 5.4).

5.2 Extracting the constraints

5.2.1 Grey matter density

First the MR brain image is segmented into its principal partitions: grey matter, white matter and cerebro-spinal fluid (Ashburner & Friston, 1997; Ashburner, 2000). A grey matter density coefficient is then determined from the smoothed grey matter image at each dipole location. The coefficient varies in value from 0, zero probability that the small cubic volume (i.e. voxel) surrounding the dipole is in grey matter, to 1, certainty that the dipole is embedded in grey matter. These coefficients constitute the leading diagonal of matrix $\mathbf{G}_s$ of size $N_j \times N_j$.

5.2.2 Dipole orientation

Here the orientation of the dipoles are fixed perpendicular to the interface between grey and white matter pointing towards the outside of the brain. This orientation is obtained from the three-dimensional gradient of the smoothed white matter volume: The gradient vector field is oriented, at each location, in the direction of the largest variation of smoothed white matter density. The smoothing is anisotropic using a diffusion process (Perona &

Malik, 1990) :

$$\frac{\delta u(\vec{r},t)}{\delta t} = \vec{\nabla}\left(c(\vec{r})\vec{\nabla}u(\vec{r},t)\right) \tag{5.3}$$

where

- $u(\vec{r},t)$ is the white matter density at location $\vec{r}$ for the virtual time instant t of the diffusion process (at time $t = 0$, $u(\vec{r},0)$ is the original unsmoothed white matter volume),
- $c(\vec{r})$, the anisotropic diffusion coefficient, is the grey matter density at location $\vec{r}$ (which remains constant throughout the diffusion process).
- the degree of smoothness is determined by the duration t of the diffusion process

The definition of $u(\vec{r},t)$ and $c(\vec{r})$ ensures that white matter is smoothed in the direction of the highest grey matter density. The gradient of the smoothed white matter image is thus oriented perpendicular to the grey and white matter interface. This ensures that the gradient of the smoothed white matter volume is appropriate for fixing the orientation of each dipole.

5.2.3 Spatial coherence

The spatial coherence of the dipoles is modelled on the basis of their "connectivity". The $N_j \times N_j$ matrix $\mathbf{D}_s$ represents this spatial coherence. As the dipoles are spread on a regular three-dimensional grid, each dipole has at most 26 nearest neighbours. Not all neighbour dipoles should be connected to the central one. Connectivity depends on brain anatomy, e.g. dipoles located on opposite sides of a sulcus should not be connected.

The connectivity of a (central) dipole located at $\vec{r}$ with its nearest neighbours located at $\vec{r} + \vec{dr}$ is determined by a first order approximation to the white matter gradient $\frac{\delta WM}{\delta \vec{r}}$ around the central dipole:

$$\frac{\delta WM}{\delta \vec{r}}(\vec{r} + \vec{dr}) = \frac{\delta WM}{\delta \vec{r}}(\vec{r}) + \vec{dr}\,\frac{\delta^2 WM}{\delta \vec{r}^{\,2}}(\vec{r}) \tag{5.4}$$

This estimated orientation is compared to the empirical white matter gradient at the neighbouring dipole locations. If the discrepancy is too large, the dipoles are considered disconnected, as for the case of dipoles on opposite sides of a sulcus. Otherwise the dipoles are considered to be connected. This gives a sparse connectivity matrix $\mathbf{\Delta}$ with element 1 for a connection or 0 otherwise. The spatial coherence can be derived from $\mathbf{\Delta}$ in a variety of ways. For example if we assume a simple spatial regressive model for the spread of activity from one dipole to another, we obtain

$$\mathbf{D}_s^t\mathbf{D}_s = (\mathbf{I}_{N_j} - \sigma\mathbf{\Delta})^{-1}(\mathbf{I}_{N_j} - \sigma\mathbf{\Delta})^{-t} \tag{5.5}$$

Alternatively we can assume some decreasing function of path length (e.g. Gaussian), where path length is the shortest path from one dipole to another based on $\mathbf{\Delta}$, to generate $\mathbf{D}_s$.

5.2.4 Temporal coherence and window of activity

The temporal constraints are directly based on our knowledge of the EEG signal and do not require an explicit extraction from the data. The window activity is modelled by the leading diagonal matrix $\mathbf{G}_t$ (size $N_t \times N_t$). The i^{th} diagonal element of $\mathbf{G}_t$ takes a value between 0, zero probability of evoked activity at the i^{th} time instant, and 1, certainty of evoked activity at the i^{th} time instant. The temporal coherence is modelled by the matrix $\mathbf{D}_t$ of size $N_t \times N_t$. The matrix $\mathbf{D}_t$ can be defined, for example, as a convolution matrix with a Gaussian kernel of known width.

5.3 Basis function sets

5.3.1 Spatial basis functions

From section 5.1, the instantaneous noise free problem is expressed by:

$$\mathbf{v} = \mathbf{L}\,\mathbf{j} \tag{5.6}$$

where $\mathbf{j}$ is unknown.

With the matrices $\mathbf{G}_s$, grey matter density at the dipole locations, and $\mathbf{D}_s$, spatial coherence among the dipoles, a set of spatial basis functions can be generated that will allow the source distribution to be spatially modelled with a substantial reduction in the uncertainty of the solution. Such an approach has already been applied in the analysis of fMRI activation studies by Kiebel *et al.* (2000). To reduce the size of the solution space from N_j to N_{k_s}, where $N_{k_s} < N_j$, the sources $\mathbf{j}$ can be modelled as:

$$\mathbf{j} = \mathbf{B}_s\,\mathbf{k}_s \qquad \Leftrightarrow \qquad \mathbf{B}_s^t\,\mathbf{j} = \mathbf{k}_s \tag{5.7}$$

where $\mathbf{B}_s$ is a $N_j \times N_{k_s}$ matrix that maximises the mutual information (MI) (Jones, 1979) between $\mathbf{j}$ and $\mathbf{k}_s$:

$$\mathrm{MI}(\mathbf{j}, \mathbf{k}_s) = \mathrm{H}(\mathbf{j}) + \mathrm{H}(\mathbf{k}_s) - \mathrm{H}(\mathbf{j} \cap \mathbf{k}_s) = \mathrm{H}(\mathbf{k}_s) \tag{5.8}$$

because $\mathrm{H}(\mathbf{j}) = \mathrm{H}(\mathbf{j} \cap \mathbf{k}_s)$ where $\mathrm{H}(\mathbf{j})$ represents the entropy of $\mathbf{j}$. If $\mathbf{k}_s$ is multinormal, then:

$$\mathrm{H}(\mathbf{k}_s) \propto \ln(|\mathbf{C}_{\mathbf{k}_s}|) = \sum_i \ln(\lambda_i) \tag{5.9}$$

where $\mathbf{C}_{\mathbf{k}_s} = \mathbf{k}_s\,\mathbf{k}_s^t = \mathbf{B}_s^t \mathbf{j}\,\mathbf{j}^t \mathbf{B}_s = \mathbf{B}_s^t \mathbf{C}_\mathbf{j} \mathbf{B}_s$ is the variance-covariance matrix of $\mathbf{k}_s$ and the λ_i are $\mathbf{C}_{\mathbf{k}_s}$'s eigenvalues. The expression to maximise is thus:

$$\ln|\mathbf{B}_s^t \mathbf{C}_\mathbf{j} \mathbf{B}_s| = \sum_i \ln(\lambda_i) \tag{5.10}$$

Therefore the matrix $\mathbf{B}_s$ should comprise the eigenvectors of the variance-covariance matrix $\mathbf{C}_\mathbf{j} = \mathbf{j}\,\mathbf{j}^t$ corresponding to the highest eigenvalues λ_i.

Prior knowledge about $\mathbf{j}$, embodied in $\mathbf{D}_s$ and $\mathbf{G}_s$, can be included by noting:

$$\mathbf{C}_\mathbf{j} = \mathbf{G}_s^{t/2} \mathbf{D}_s^t \mathbf{D}_s \mathbf{G}_s^{1/2} \tag{5.11}$$

$\mathbf{B}_s$ is obtained from the eigenvector solution of $\mathbf{G}_s^{t/2}\mathbf{D}_s^t\mathbf{D}_s\mathbf{G}_s^{1/2}$ or equivalently by using the singular value decomposition of $\mathbf{D}_s\mathbf{G}_s^{1/2}$:

$$\mathbf{U}_s\mathbf{S}_s\mathbf{W}_s^t = \mathrm{svd}(\mathbf{D}_s\mathbf{G}_s^{1/2}) \tag{5.12}$$

Columns of $\mathbf{W}_s$ corresponding to the highest singular values $\mathbf{S}_s$, are used to define $\mathbf{B}_s$ (see section 6.1.1).

5.3.2 Temporal basis functions

From equation 5.2, the full noise free problem is :

$$\mathbf{V} = \mathbf{L}\,\mathbf{J} \tag{5.13}$$

The spatial basis function set $\mathbf{B}_s$ obtained in section 5.3.1 can be used to reduce the size of the problem in space :

$$\mathbf{V} = \mathbf{L}\,\mathbf{J} = \mathbf{L}\,\mathbf{B}_s\,\mathbf{K}_s = \mathbf{L}_{\mathbf{B}_s}\,\mathbf{K}_s \tag{5.14}$$

where $\mathbf{K}_s$ is a $N_{k_s} \times N_t$ matrix.

With the matrices $\mathbf{G}_t$, window of activity, and $\mathbf{D}_t$, temporal coherence, a set of temporal basis functions can be generated that will model the time course of the sources activity. To reduce the size of the "temporal space" from N_t to N_{k_t}, the $N_j \times N_t$ source matrix $\mathbf{J}$ can be modelled as :

$$\mathbf{J} = \mathbf{K}_t\,\mathbf{B}_t^t = \mathbf{B}_s\,\mathbf{K}_{st}\,\mathbf{B}_t^t \quad \Leftrightarrow \quad \mathbf{B}_s^t\,\mathbf{J}\,\mathbf{B}_t = \mathbf{K}_{st} \tag{5.15}$$

where $\mathbf{K}_{st}$ is a $N_{k_s} \times N_{k_t}$ matrix and $\mathbf{B}_t$ is a $N_t \times N_{k_t}$ matrix obtained, in a similar way to $\mathbf{B}_s$, from the singular value decomposition of $\mathbf{D}_t\mathbf{G}_t^{1/2}$:

$$\mathbf{U}_t\mathbf{S}_t\mathbf{W}_t^t = \mathrm{svd}(\mathbf{D}_t\mathbf{G}_t^{1/2}) \tag{5.16}$$

The first columns of $\mathbf{W}_t$, corresponding to the highest singular values $\mathbf{S}_t$, are used to define $\mathbf{B}_t$.

5.4 Constrained minimum norm solution

5.4.1 Instantaneous problem

Given the spatial basis function set $\mathbf{B}_s$, the instantaneous source localisation problem 5.1 can be reformulated as :

$$\mathbf{v} + \boldsymbol{\varepsilon} = \mathbf{L}\,\mathbf{B}_s\,\mathbf{k}_s = \mathbf{L}_{\mathbf{B}_s}\,\mathbf{k}_s \tag{5.17}$$

To solve this reduced problem, a simple pseudo-inverse, e.g. Moore-Penrose pseudo-inverse, could be applied on $\mathbf{L}_{\mathbf{B}_s}$ but because of the ill-posedness[1] of the source localisation problem, this unconstrained solution is generally inadequate (Gençer & Williamson, 1998).

[1] a linear problem is said to be "ill-posed" if any of the three following conditions is not satisfied : there exists a solution, the solution is unique and it depends continuously on the data.

A regularisation constraint on the solution can be applied to minimise some weighted norm $\|\mathbf{H}\,\mathbf{j}\|$ of the current density $\mathbf{j} = \mathbf{B}_s\,\mathbf{k}_s$ or some weighted norm $\|\mathbf{H}_{\mathbf{B}_s}\,\mathbf{k}_s\|$ of the basis functions coefficients $\mathbf{k}_s$. Assuming the noise $\boldsymbol{\varepsilon}$ is characterised by the covariance matrix $\mathrm{cov}(\boldsymbol{\varepsilon}) = \mathbf{C}_{\boldsymbol{\varepsilon}}$, the weighted minimum norm problem or "Tikhonov regularisation" (Tikhonov & Arsenin, 1977) is expressed as:

$$\hat{\mathbf{j}} = \arg\min_{\mathbf{j}} \left\{ \|\mathbf{C}_{\boldsymbol{\varepsilon}}^{-1/2}(\mathbf{L}\,\mathbf{j} - \mathbf{v}_{\boldsymbol{\varepsilon}})\|^2 + \lambda^2 \|\mathbf{H}\,\mathbf{j}\|^2 \right\} \tag{5.18}$$

and, incorporating the basis function coefficients $\mathbf{k}_s$,

$$\hat{\mathbf{k}}_s = \arg\min_{\mathbf{k}_s} \left\{ \|\mathbf{C}_{\boldsymbol{\varepsilon}}^{-1/2}(\mathbf{L}_{\mathbf{B}_s}\,\mathbf{k}_s - \mathbf{v}_{\boldsymbol{\varepsilon}})\|^2 + \lambda^2 \|\mathbf{H}_{\mathbf{B}_s}\,\mathbf{k}_s\|^2 \right\} \tag{5.19}$$

where $\mathbf{v}_{\boldsymbol{\varepsilon}} = \mathbf{v} + \boldsymbol{\varepsilon}$ represents underlying signal with noise. Here λ is a hyperparameter that controls the influence of the constraints relative to minimising the error of the fit. Its estimation will be discussed in section 5.5. There exists a direct mathematical relation between the Moore-Penrose pseudo-inverse and the Tikhonov regularisation, see appendix C.

The weighted minimum norm problem could also be expressed like a "Least Square" problem:

$$\begin{bmatrix} \mathbf{C}_{\boldsymbol{\varepsilon}}^{-1/2}\mathbf{L}_{\mathbf{B}_s} \\ \lambda\,\mathbf{H}_{\mathbf{B}_s} \end{bmatrix} \mathbf{k}_s = \begin{bmatrix} \mathbf{C}_{\boldsymbol{\varepsilon}}^{-1/2}\mathbf{v} \\ 0 \end{bmatrix} + \begin{bmatrix} \boldsymbol{\varepsilon}_1 \\ \boldsymbol{\varepsilon}_2 \end{bmatrix} \tag{5.20}$$

where $\boldsymbol{\varepsilon}_1 = \mathbf{C}_{\boldsymbol{\varepsilon}}^{-1/2}\boldsymbol{\varepsilon}$. This problem is solved by minimising, in a least square sense, the norm of the residuals $[\boldsymbol{\varepsilon}_1^t\ \boldsymbol{\varepsilon}_2^t]^t$:

$$\hat{\mathbf{k}}_s = \arg\min_{\mathbf{k}_s} \left\| \begin{bmatrix} \mathbf{C}_{\boldsymbol{\varepsilon}}^{-1/2}\mathbf{L}_{\mathbf{B}_s} \\ \lambda\,\mathbf{H}_{\mathbf{B}_s} \end{bmatrix} \mathbf{k}_s - \begin{bmatrix} \mathbf{C}_{\boldsymbol{\varepsilon}}^{-1/2}\mathbf{v}_{\boldsymbol{\varepsilon}} \\ 0 \end{bmatrix} \right\|^2 \tag{5.21}$$

Equations 5.19 and 5.21 are obviously equivalent.

The solution of 5.19 should provide the best fit to the data while minimising the constraint $\|\mathbf{H}_{\mathbf{B}_s}\,\mathbf{k}_s\|^2$. Such a solution has the form:

$$\hat{\mathbf{k}}_s = \mathbf{T}_{\mathbf{B}_s}\,\mathbf{v}_{\boldsymbol{\varepsilon}} \quad \Rightarrow \quad \hat{\mathbf{j}} = \mathbf{B}_s\,\mathbf{T}_{\mathbf{B}_s}\,\mathbf{v}_{\boldsymbol{\varepsilon}} = \mathbf{T}\,\mathbf{v}_{\boldsymbol{\varepsilon}} \tag{5.22}$$

and

$$\mathbf{T}_{\mathbf{B}_s} = \left[\mathbf{L}_{\mathbf{B}_s}^t\,\mathbf{C}_{\boldsymbol{\varepsilon}}^{-1}\mathbf{L}_{\mathbf{B}_s} + \lambda^2\left(\mathbf{H}_{\mathbf{B}_s}^t\,\mathbf{H}_{\mathbf{B}_s}\right)\right]^{-1}\mathbf{L}_{\mathbf{B}_s}^t\,\mathbf{C}_{\boldsymbol{\varepsilon}}^{-1} \tag{5.23a}$$

$$= \left(\mathbf{H}_{\mathbf{B}_s}^t\,\mathbf{H}_{\mathbf{B}_s}\right)^{-1}\mathbf{L}_{\mathbf{B}_s}^t\left[\mathbf{L}_{\mathbf{B}_s}\left(\mathbf{H}_{\mathbf{B}_s}^t\,\mathbf{H}_{\mathbf{B}_s}\right)^{-1}\mathbf{L}_{\mathbf{B}_s}^t + \lambda^2\mathbf{C}_{\boldsymbol{\varepsilon}}\right]^{-1} \tag{5.23b}$$

using the matrix inversion Lemma.

There is an important and useful connection with Bayesian estimates of the sources here, where under Gaussian assumptions, the conditional expectation or posterior mean of the sources $\mathbf{k}_s$ is given by:

$$E(\mathbf{k}_s|\mathbf{v}_{\boldsymbol{\varepsilon}}) = \left[\mathbf{L}_{\mathbf{B}_s}^t\,\mathbf{C}_{\boldsymbol{\varepsilon}}^{-1}\mathbf{L}_{\mathbf{B}_s} + \mathbf{C}_{\mathbf{k}_s}^{-1}\right]^{-1}\mathbf{L}_{\mathbf{B}_s}^t\,\mathbf{C}_{\boldsymbol{\varepsilon}}^{-1}\mathbf{v}_{\boldsymbol{\varepsilon}} \tag{5.24a}$$

$$= \mathbf{C}_{\mathbf{k}_s}\mathbf{L}_{\mathbf{B}_s}^t\left[\mathbf{L}_{\mathbf{B}_s}\mathbf{C}_{\mathbf{k}_s}\mathbf{L}_{\mathbf{B}_s}^t + \mathbf{C}_{\boldsymbol{\varepsilon}}\right]^{-1}\mathbf{v}_{\boldsymbol{\varepsilon}} \tag{5.24b}$$

where $\mathbf{C}_{\mathbf{k}_s}$ is the prior spatial covariance of the sources. Comparing 5.24 with 5.23 provides the motivation for choosing forms of $\mathbf{H}_{\mathbf{B}_s}$ such that:

$$\mathbf{H}_{\mathbf{B}_s} \propto \mathbf{C}_{\mathbf{k}_s}^{-1/2} \tag{5.25}$$

In the particular and theoretical case where the measurements are noise-free (or supposedly so), i.e $\mathbf{v}_{\boldsymbol{\mathcal{E}}} = \mathbf{v}$, the solution of 5.19 is obtained from 5.23b by taking the limit $\lambda \to 0$ (Rao & Mitra, 1973), i.e. minimising the constraint $\|\mathbf{H}_{\mathbf{B}_s}\,\mathbf{k}_s\|^2$ **after** fitting the model perfectly:

$$\mathbf{T}_{\mathbf{B}_s} = \left(\mathbf{H}_{\mathbf{B}_s}^t\,\mathbf{H}_{\mathbf{B}_s}\right)^{-1}\mathbf{L}_{\mathbf{B}_s}^t\left[\mathbf{L}_{\mathbf{B}_s}\left(\mathbf{H}_{\mathbf{B}_s}^t\,\mathbf{H}_{\mathbf{B}_s}\right)^{-1}\mathbf{L}_{\mathbf{B}_s}^t\right]^{-1} \tag{5.26}$$

When noise free simulated data will be employed to assess the solutions developed (sections 7.2 and 7.3), these solutions will be based on equation 5.26 and it will not be necessary to estimate λ. In the other cases, where some noise is added in the simulated data (section 7.4), the solutions will be computed using equation 5.23 and λ will have to be estimated every time.

5.4.2 Non-instantaneous problem

For non-instantaneous data, the sources $\mathbf{J}$ can be modelled by the spatial and temporal basis function sets $\mathbf{B}_s$ and $\mathbf{B}_t$, such that the problem 5.2 can be reformulated as

$$\mathbf{V} + \boldsymbol{\mathcal{E}} = \mathbf{L}\,\mathbf{B}_s\,\mathbf{K}_{st}\,\mathbf{B}_t^t \tag{5.27}$$

which becomes

$$(\mathbf{V} + \boldsymbol{\mathcal{E}})\,\mathbf{B}_t = \mathbf{L}\,\mathbf{B}_s\,\mathbf{K}_{st} \quad \Leftrightarrow \quad \mathbf{V}_{\mathbf{B}_t} + \boldsymbol{\mathcal{E}}_{\mathbf{B}_t} = \mathbf{L}_{\mathbf{B}_s}\,\mathbf{K}_{st} \tag{5.28}$$

The weighted minimum norm can be expressed like this

$$\begin{bmatrix} \mathbf{C}_{\boldsymbol{\mathcal{E}}}^{-1/2}\mathbf{L}_{\mathbf{B}_s} \\ \lambda\,\mathbf{H}_{\mathbf{B}_s} \end{bmatrix}\mathbf{K}_{st} = \begin{bmatrix} \mathbf{C}_{\boldsymbol{\mathcal{E}}}^{-1/2}\mathbf{V}_{\mathbf{B}_t} \\ 0 \end{bmatrix} + \begin{bmatrix} \boldsymbol{\mathcal{E}}_1 \\ \boldsymbol{\mathcal{E}}_2 \end{bmatrix} \tag{5.29}$$

with $\boldsymbol{\mathcal{E}}_1 = \mathbf{C}_{\boldsymbol{\mathcal{E}}}^{-1/2}\boldsymbol{\mathcal{E}}_{\mathbf{B}_t}$. This reduced problem can be solved for each temporal basis function coefficient separately, i.e. each column of $\mathbf{K}_{st}$ at a time using equations 5.22 and 5.23, see appendix D for justification.

5.5 Hyperparameter λ evaluation

The accuracy of the Tikhonov regularisation method, presented in section 5.4, depends strongly on the choice of the hyperparameter λ. The hyperparameter λ balances the confidence between the fitting of the model $\mathbf{C}_{\boldsymbol{\mathcal{E}}}^{-1/2}(\mathbf{L}_{\mathbf{B}_s}\,\mathbf{k}_s - \mathbf{v}_{\boldsymbol{\mathcal{E}}})$ and the priors on the solution $\mathbf{H}_{\mathbf{B}_s}\,\mathbf{k}_s$ but, as λ varies, the regularised solution $\mathbf{k}_{s,\lambda}$ has properties that depend on λ. Therefore the choice of λ is crucial. As a general rule, the degree of regularisation

(λ) should increase with the noise level of the data, i.e. the importance of the priors should be increased relative to the model, but this rule is not sufficient by itself to explicitely estimate λ.

A convenient way to display and understand the properties of $\mathbf{k}_{s,\lambda}$ is to plot the (weighted) norm of the regularised solution $\|\mathbf{H}_{\mathbf{B}_s}\,\mathbf{k}_{s,\lambda}\|^2$, versus the norm of the residual vector $\|\mathbf{C}_{\boldsymbol{\varepsilon}}^{-1/2}(\mathbf{L}_{\mathbf{B}_s}\,\mathbf{k}_{s,\lambda}-\mathbf{v}_{\boldsymbol{\varepsilon}})\|^2$ for different values of λ. The curve obtained usually has an L shape (in ordinary or double logarithmic scale), hence its name of "L-curve". A satisfactory λ would be found close to the inflection of the plot (Hansen, 1992). But Engl & Grever (1994) showed that hyperparameter choice strategies based on this plot alone, e.g. on the corner of the L-curve, have the property of being independent of the norm of the residuals $\|\mathbf{C}_{\boldsymbol{\varepsilon}}^{-1/2}(\mathbf{L}_{\mathbf{B}_s}\,\mathbf{k}_s-\mathbf{v}_{\boldsymbol{\varepsilon}})\|$. Another disadvantage of this L-curve approach is that the solution must be calculated for a large number of values of λ to find the proper regularisation level.

Fortunately there may be other ways to simultaneously estimate the hyperparameter λ and its associated solution $\mathbf{k}_{s,\lambda}$ in an optimal way.

5.5.1 Maximum likelihood (ML) solution

Consider the linear stochastic model of the form

$$\mathbf{b}=\mathbf{A}\mathbf{x}+\mathbf{r} \tag{5.30}$$

where $\mathbf{A}$, the model or design matrix, is of size $m\times n$; $\mathbf{x}$, the unknown vector, is of size $n\times 1$; $\mathbf{b}$, the data vector, and $\mathbf{r}$, the residual or error vector, are of size $m\times 1$ and $\mathbf{C}$, the covariance matrix of $\mathbf{r}=\mathcal{N}(0,\mathbf{C})$, is of size $m\times m$. The normal equations of this model are:

$$(\mathbf{A}^t\mathbf{C}^{-1}\mathbf{A})\mathbf{x}=\mathbf{A}^t\mathbf{C}^{-1}\mathbf{b} \tag{5.31}$$

By solving the normal equations, the "Best Linear Unbiased Estimate" (BLUE) is obtained:

$$\hat{\mathbf{x}}=(\mathbf{A}^t\mathbf{C}^{-1}\mathbf{A})^-\mathbf{A}^t\mathbf{C}^{-1}\mathbf{b} \tag{5.32}$$

where, for any matrix B, B^- denotes an arbitrary generalised inverse of B, i.e., any solution to $BB^-B=B$.

This is equivalent to maximising the following objective likelihood function (Patterson & Thompson, 1971):

$$p(\mathbf{b}|\mathbf{x})\propto|\mathbf{C}|^{-1/2}e^{-\frac{1}{2}(\mathbf{b}-\mathbf{A}\mathbf{x})^t\mathbf{C}^{-1}(\mathbf{b}-\mathbf{A}\mathbf{x})} \tag{5.33}$$

which is also equivalent to minimising the function

$$F(\mathbf{b};\mathbf{x})=-2\log(p(\mathbf{b}|\mathbf{x}))=\log|\mathbf{C}|+(\mathbf{b}-\mathbf{A}\mathbf{x})^t\mathbf{C}^{-1}(\mathbf{b}-\mathbf{A}\mathbf{x})+\text{const} \tag{5.34}$$

The variance-covariance matrix $\mathbf{C}$ is necessary to weight the observations $\mathbf{b}$ differently according to their variance and to account for their covariance. There may be a model for this matrix, depending on hyperparameters $\boldsymbol{\theta}=[\theta_1\ \theta_2\ldots]$, but its exact value is not necessarily known *a priori* and needs to be estimated as well as $\mathbf{x}$.

5.5.2 Restricted maximum likelihood (ReML) solution

Assume that the variance-covariance matrix $\mathbf{C}$ is a function of the unknown hyperparameters θ_i, $\mathbf{C} = \mathbf{C}(\boldsymbol{\theta})$ and $\boldsymbol{\theta} = [\theta_1\ \theta_2 \ldots]$. There is a scheme that allows the simultaneous estimation of $\mathbf{x}$ and $\mathbf{C}(\boldsymbol{\theta})$, that properly takes into account the loss of degrees of freedom in the model incured from estimating $\mathbf{x}$ (Patterson & Thompson, 1971) when $\mathbf{C}(\boldsymbol{\theta})$ is calculated.

Starting estimates are initially assigned to $\boldsymbol{\theta}$. With the current estimate $\hat{\boldsymbol{\theta}}$, $\hat{\mathbf{x}}$ is estimated by maximising the first likelihood function 5.33. Then an updated estimate of $\boldsymbol{\theta}$ is calculated from the current value $\hat{\mathbf{x}}$. The procedure is repeated until convergence of both $\hat{\mathbf{x}}$ and $\hat{\boldsymbol{\theta}}$.

Harville (1974) showed that this iterative procedure maximises the following function which has subsequently been named "Restricted Maximum Likelihood" (ReML) objective function:

$$p(\mathbf{b}|\mathbf{x},\boldsymbol{\theta}) = \sqrt{\frac{|\mathbf{A}^t\mathbf{A}|}{(2\pi)^{m-n}|\mathbf{C}(\boldsymbol{\theta})|\ |\mathbf{A}^t\mathbf{C}(\boldsymbol{\theta})^{-1}\mathbf{A}|}}\ e^{-\frac{1}{2}(\mathbf{b}-\mathbf{A}\mathbf{x})^t\mathbf{C}(\boldsymbol{\theta})^{-1}(\mathbf{b}-\mathbf{A}\mathbf{x})} \tag{5.35}$$

Maximising 5.35 is equivalent to minimising:

$$\begin{aligned} F(\mathbf{b};\mathbf{x},\boldsymbol{\theta}) &= -2\log(p(\mathbf{b}|\mathbf{x},\boldsymbol{\theta})) \\ &= \log|\mathbf{A}^t\mathbf{C}(\boldsymbol{\theta})^{-1}\mathbf{A}| + \log|\mathbf{C}(\boldsymbol{\theta})| + (\mathbf{b}-\mathbf{A}\mathbf{x})^t\mathbf{C}(\boldsymbol{\theta})^{-1}(\mathbf{b}-\mathbf{A}\mathbf{x}) + \text{const} \end{aligned} \tag{5.36}$$

There exists a general iterative approach for estimating $\mathbf{x}$ and $\boldsymbol{\theta}$ but a linear parameterisation of $\mathbf{C}$, i.e. $\mathbf{C}(\boldsymbol{\theta}) = \sum \theta_i\mathbf{G}_i$ where $\mathbf{G}_i$ are $n \times n$ symmetric matrices whose elements are known, leads to a much simpler and less computationally demanding approach (Harville, 1977).

5.5.3 Simple ReML solution

One such case of linear parameterisation of $\mathbf{C}$ involves a diagonal covariance matrix with each element parameterised by only one element[2] of $\boldsymbol{\theta}$. With only two hyperparameters $\boldsymbol{\theta} = [\theta_1^2\ \theta_2^2]$, the matrices and vectors of 5.30 can be separated into two parts:

$$\begin{bmatrix} \mathbf{b}_1 \\ \mathbf{b}_2 \end{bmatrix} = \begin{bmatrix} \mathbf{A}_1 \\ \mathbf{A}_2 \end{bmatrix} \mathbf{x} + \begin{bmatrix} \mathbf{r}_1 \\ \mathbf{r}_2 \end{bmatrix} \tag{5.37}$$

and

$$\text{var}\left(\begin{bmatrix} \mathbf{r}_1 \\ \mathbf{r}_2 \end{bmatrix}\right) = \begin{bmatrix} \theta_1^2\mathbf{I}_{m_1} & 0 \\ 0 & \theta_2^2\mathbf{I}_{m_2} \end{bmatrix} = \mathbf{C}(\boldsymbol{\theta}) \tag{5.38}$$

with m_1, the number of rows in $\mathbf{A}_1$ and $\mathbf{b}_1$ and m_2, the number of rows in $\mathbf{A}_2$ and $\mathbf{b}_2$ such that $m_1 + m_2 = m$.

The iterative scheme involves assigning (non-zero) starting estimates for $\boldsymbol{\theta}$ and estimating $\mathbf{x}$ with relation 5.32:

$$\hat{\mathbf{x}} = (\theta_1^{-2}\mathbf{A}_1^t\mathbf{A}_1 + \theta_2^{-2}\mathbf{A}_2^t\mathbf{A}_2)^{-1}(\theta_1^{-2}\mathbf{A}_1^t\mathbf{b}_1 + \theta_2^{-2}\mathbf{A}_2^t\mathbf{b}_2) \tag{5.39}$$

[2] because θ_1 and θ_2 will be modelling variances, and by notational convention, the elements of $\boldsymbol{\theta}$ are squared. $\mathbf{C}$ will thus be linearly parameterised by θ_1^2 and θ_2^2, i.e. $\mathbf{C}(\boldsymbol{\theta}) = \sum \theta_i^2\mathbf{G}_i$.

Updated values of the hyperparameters are then obtained from the residuals

$$\mathbf{r} = \begin{bmatrix} \mathbf{r}_1 \\ \mathbf{r}_2 \end{bmatrix} = \mathbf{b} - \mathbf{A}\hat{\mathbf{x}} \tag{5.40}$$

and take into account the loss of degrees of freedom resulting from the estimation of $\hat{\mathbf{x}}$:

$$p_1 = \text{trace}\left((\theta_1^{-2}\mathbf{A}_1^t\mathbf{A}_1 + \theta_2^{-2}\mathbf{A}_2^t\mathbf{A}_2)^{-1}\theta_1^{-2}\mathbf{A}_1^t\mathbf{A}_1\right) \tag{5.41a}$$

$$p_2 = \text{trace}\left((\theta_1^{-2}\mathbf{A}_1^t\mathbf{A}_1 + \theta_2^{-2}\mathbf{A}_2^t\mathbf{A}_2)^{-1}\theta_2^{-2}\mathbf{A}_2^t\mathbf{A}_2\right) = n - p_1 \tag{5.41b}$$

The new estimates of $\boldsymbol{\theta}$ are:

$$\hat{\theta}_1^2 = \frac{\mathbf{r}_1^t\mathbf{r}_1}{m_1 - p_1} \tag{5.42a}$$

$$\hat{\theta}_2^2 = \frac{\mathbf{r}_2^t\mathbf{r}_2}{m_2 - p_2} \tag{5.42b}$$

The iterative procedure continues by using these new hyperparameter estimates to re-estimate $\mathbf{x}$, then from the updated $\hat{\mathbf{x}}$, a new set of $\boldsymbol{\theta}$. Eventually the algorithm converges to a stable solution.

The hyperparameters θ_1^2 and θ_2^2 are the variance components of each subproblem. If the algorithm is started with strictly positive values, then at no point can the values of $\boldsymbol{\theta}$ ever become negative and, in fact, will never reach zero. Obviously the algorithm should not be started with zero or negative starting estimates.

5.5.4 Simple ReML solution in a non-instantaneous problem

Consider the case of the linear stochastic model 5.30 with non-instantaneous data, i.e. the $m \times 1$ data vector $\mathbf{b}$ (resp. residual vector $\mathbf{r}$) is replaced by a $m \times q$ matrix $\mathbf{B}$ (resp. $\mathbf{R}$) and the $n \times 1$ vector $\mathbf{x}$, by a $n \times q$ matrix $\mathbf{X}$:

$$\mathbf{B} = \mathbf{A}\mathbf{X} + \mathbf{R} \quad \Leftrightarrow \quad \begin{bmatrix} \mathbf{B}_1 \\ \mathbf{B}_2 \end{bmatrix} = \begin{bmatrix} \mathbf{A}_1 \\ \mathbf{A}_2 \end{bmatrix} \mathbf{X} + \begin{bmatrix} \mathbf{R}_1 \\ \mathbf{R}_2 \end{bmatrix} \tag{5.43}$$

If the covariance matrix $\mathbf{C}$ of the residuals $\mathbf{R}$ still depends linearly on two hyperparameters $\boldsymbol{\theta} = [\theta_1^2\ \theta_2^2]$ as in 5.38, then a similar iterative scheme can be applied to estimate both $\mathbf{X}$ and $\boldsymbol{\theta}$. With starting estimates for $\boldsymbol{\theta}$, a first solution for $\mathbf{X}$ is calculated with equation 5.39:

$$\hat{\mathbf{X}} = (\theta_1^{-2}\mathbf{A}_1^t\mathbf{A}_1 + \theta_2^{-2}\mathbf{A}_2^t\mathbf{A}_2)^{-1}(\theta_1^{-2}\mathbf{A}_1^t\mathbf{B}_1 + \theta_2^{-2}\mathbf{A}_2^t\mathbf{B}_2) \tag{5.44}$$

The values of $\boldsymbol{\theta}$ are then updated from the residuals:

$$\mathbf{R} = \begin{bmatrix} \mathbf{R}_1 \\ \mathbf{R}_2 \end{bmatrix} = \begin{bmatrix} \mathbf{r}_{1,1} & \mathbf{r}_{1,2} & \dots & \mathbf{r}_{1,q} \\ \mathbf{r}_{2,1} & \mathbf{r}_{2,2} & \dots & \mathbf{r}_{2,q} \end{bmatrix} = \mathbf{B} - \mathbf{A}\hat{\mathbf{X}} \tag{5.45}$$

using relations similar to 5.42 :

$$\hat{\theta}_1^2 = \frac{\sum_{i=1}^{q} \mathbf{r}_{1,i}^t \mathbf{r}_{1,i}}{q\,(m_1 - p_1)} \tag{5.46a}$$

$$\hat{\theta}_2^2 = \frac{\sum_{i=1}^{q} \mathbf{r}_{2,i}^t \mathbf{r}_{2,i}}{q\,(m_2 - p_2)} \tag{5.46b}$$

where p_1 and p_2 are calculated with equations 5.41, see appendix D for the justification. The iterative procedure continues, as in section 5.5.3, by re-estimating $\mathbf{X}$ with these new values of $\boldsymbol{\theta}$. The process is repeated until convergence of the values of $\mathbf{X}$ and $\boldsymbol{\theta}$

5.5.5 ReML and constrained minimum norm solution

Clearly equations 5.37 and 5.43 are similar to equations 5.20 and 5.29 with

$$\mathbf{A}_1 = \mathbf{C}_{\boldsymbol{\mathcal{E}}}^{-1/2} \mathbf{L}_{\mathbf{B}_s} \tag{5.47a}$$

$$\mathbf{A}_2 = \mathbf{H}_{\mathbf{B}_s} \tag{5.47b}$$

$$\mathbf{x} = \mathbf{k}_s \quad (\text{or } \mathbf{X} = \mathbf{K}_{st}) \tag{5.47c}$$

$$\mathbf{b}_1 = \mathbf{C}_{\boldsymbol{\mathcal{E}}}^{-1/2} \mathbf{v}_{\boldsymbol{\mathcal{E}}} \quad (\text{or } \mathbf{B}_1 = \mathbf{C}_{\boldsymbol{\mathcal{E}}}^{-1/2} \mathbf{V}_{\mathbf{B}_t}) \tag{5.47d}$$

$$\mathbf{b}_2 = 0 \quad (\text{or } \mathbf{B}_2 = 0) \tag{5.47e}$$

By considering λ as the ratio between the variance θ_1^2 of the residuals of the model $\mathbf{C}_{\boldsymbol{\mathcal{E}}}^{-1/2}(\mathbf{L}_{\mathbf{B}_s}\mathbf{k}_s - \mathbf{v}_{\boldsymbol{\mathcal{E}}})$ and the variance θ_2^2 of the weighted solution $\mathbf{H}_{\mathbf{B}_s}\mathbf{k}_s$, then it is possible to apply the ReML iterative procedure described in sections 5.5.3 and 5.5.4 to estimate both $\mathbf{k}_s$ and $\lambda = \theta_1/\theta_2$ in

$$\hat{\mathbf{k}}_s = \arg\min_{\mathbf{k}_s} \left\| \begin{bmatrix} \theta_1^{-1}\,\mathbf{I}_{N_e} & 0 \\ 0 & \theta_2^{-1}\,\mathbf{I}_{N_j} \end{bmatrix} \left(\begin{bmatrix} \mathbf{C}_{\boldsymbol{\mathcal{E}}}^{-1/2}\mathbf{L}_{\mathbf{B}_s} \\ \mathbf{H}_{\mathbf{B}_s} \end{bmatrix} \mathbf{k}_s - \begin{bmatrix} \mathbf{C}_{\boldsymbol{\mathcal{E}}}^{-1/2}\mathbf{v}_{\boldsymbol{\mathcal{E}}} \\ 0 \end{bmatrix} \right) \right\|^2 \tag{5.48}$$

The use of a constant variance θ_1^2 for the residuals of the model and θ_2^2 for the residuals of the constraint is realistic. Indeed, the residuals of the model $\mathbf{L}_{\mathbf{B}_s}\,\mathbf{k}_s - \mathbf{v}_{\boldsymbol{\mathcal{E}}}$ is premultiplied by $\mathbf{C}_{\boldsymbol{\mathcal{E}}}^{-1/2}$, the inverse of the square root of its covariance (or its best estimator at least), therefore the residuals are "whitened" and the remaining variance can be approximated by a scaled identity matrix $\theta_1^2\,\mathbf{I}_{N_e}$. Similarly, the matrix $\mathbf{H}_{\mathbf{B}_s}$ can be interpreted as the inverse of the square root of the *a priori* covariance of the sources, as shown in equation 5.25, thus the variance of the weighted solution $\mathbf{H}_{\mathbf{B}_s}\mathbf{k}_s$ can be modelled by $\theta_2^2\,\mathbf{I}_{N_j}$.

Chapter 6

Constrained minimum norm solution : Application

Contents

6.1 Step 1 : Estimating the spatio-temporal basis function sets

In this section, the theoretical approach presented in sections 5.3.1 and 5.3.2 to extract the spatial and temporal basis functions is applied to a realistic head model and recorded free brain EEG activity (and measurement noise).

6.1.1 Spatial basis functions

The MR image used in section 4.4 to generate the realistic head model, was segmented with the segmentation function of the SPM99 software package (Wellcome Department of Cognitive Neurology, 1999), and the grey matter image was averaged over each dipole cubic volume to provide the grey matter coefficient for the matrix $\mathbf{G}_s$. The 12300 dipoles noted in section 4.4 for which the lead field was calculated are the dipoles, from the original full grid, located in voxels with a grey matter density greater than 0.4 (i.e. 40% of the voxel was grey matter or the probability of all the voxel being grey matter was 0.4 or

more). This density value ensured that each dipole represented the electric activity of a small volume of the brain containing a sufficient amount of grey matter. Selecting this subset of all potential dipoles represents a compromise between considering all the dipoles and those that potentially contribute a substantial signal (i.e. it is pointless to retain dipoles located in the white matter or the cerebro-spinal fluid). Using the BEM solution described in chapter 3, the lead field matrix $\mathbf{L}$ between the 12300 dipole locations and the 61 electrode sites was calculated as decribed in section 4.4.

The following numerical approximation of equation 5.3 was used to smooth the white matter anisotropically:

$$u^{t+1}_{(i,j,k)} = u^{t}_{(i,j,k)} + \lambda \left[c_N \, \delta_N u + c_S \, \delta_S u + c_E \, \delta_E u + c_W \, \delta_W u + c_U \, \delta_U u + c_A \, \delta_A u \right]^{t}_{(i,j,k)} \tag{6.1}$$

where $c_{(i,j,k)}$ is the grey matter density at voxel (i,j,k), $u^{t}_{(i,j,k)}$ is the white matter density at voxel (i,j,k) and iteration t, and

$$\delta_N u = u_{(i+1,j,k)} - u_{(i,j,k)} \qquad c_N = \frac{c_{(i+1,j,k)} + c_{(i,j,k)}}{2} \tag{6.2a}$$

$$\delta_S u = u_{(i-1,j,k)} - u_{(i,j,k)} \qquad c_S = \frac{c_{(i-1,j,k)} + c_{(i,j,k)}}{2} \tag{6.2b}$$

$$\delta_E u = u_{(i,j+1,k)} - u_{(i,j,k)} \qquad c_E = \frac{c_{(i,j+1,k)} + c_{(i,j,k)}}{2} \tag{6.2c}$$

$$\delta_W u = u_{(i,j-1,k)} - u_{(i,j,k)} \qquad c_W = \frac{c_{(i,j-1,k)} + c_{(i,j,k)}}{2} \tag{6.2d}$$

$$\delta_U u = u_{(i,j,k+1)} - u_{(i,j,k)} \qquad c_U = \frac{c_{(i,j,k+1)} + c_{(i,j,k)}}{2} \tag{6.2e}$$

$$\delta_A u = u_{(i,j,k-1)} - u_{(i,j,k)} \qquad c_A = \frac{c_{(i,j,k-1)} + c_{(i,j,k)}}{2} \tag{6.2f}$$

To ensure that the smoothing process is stable, it is necessary to select λ such that $0 < \lambda < 1/8$. An isotropic diffusion process, i.e. with $c_{(i,j,k)} = 1$ everywhere, approximates a Gaussian function of kernel $\sigma = \sqrt{2\lambda t}$. By choosing σ to be equal to the inter-dipole distance and taking $\lambda = 1/10$, the number t of iterations is specified to give the required smoothing. Starting with u^0, the segmented white matter volume, equation 6.1 was applied iteratively until the desired smoothing was achieved. The gradient of the smoothed white matter was then calculated and sampled at the location of the dipoles. The successive steps of the MRI processing are summarised in figure 6.1.

Equation 5.4 was used to determine the connectivity of neighbouring dipoles. The estimated orientation of neighbouring dipoles was compared with their real orientation and if the angle between the orientations was greater than $\pi/2$, the dipoles were considered disconnected. Instead of using equation 5.5, a Gaussian function of path length was used. This allowed to model spatial coherence more directly than in 5.5. The path length was calculated as follows: For each pair of connected dipoles, a parabolic curve joining the dipoles and fitting their orientation was calculated. The length of this curve was used as "path-length". The distance between two dipoles that were not directly connected was obtained by looking for the shortest path (within an upper limit of 30mm) composed of connected dipoles.

Two degrees of spatial coherence were studied by using two different Gaussians, $\sigma =$ 10mm, and $\sigma =$ 5mm. For each of the two $\mathbf{D}$ matrices obtained, the eigenvectors of

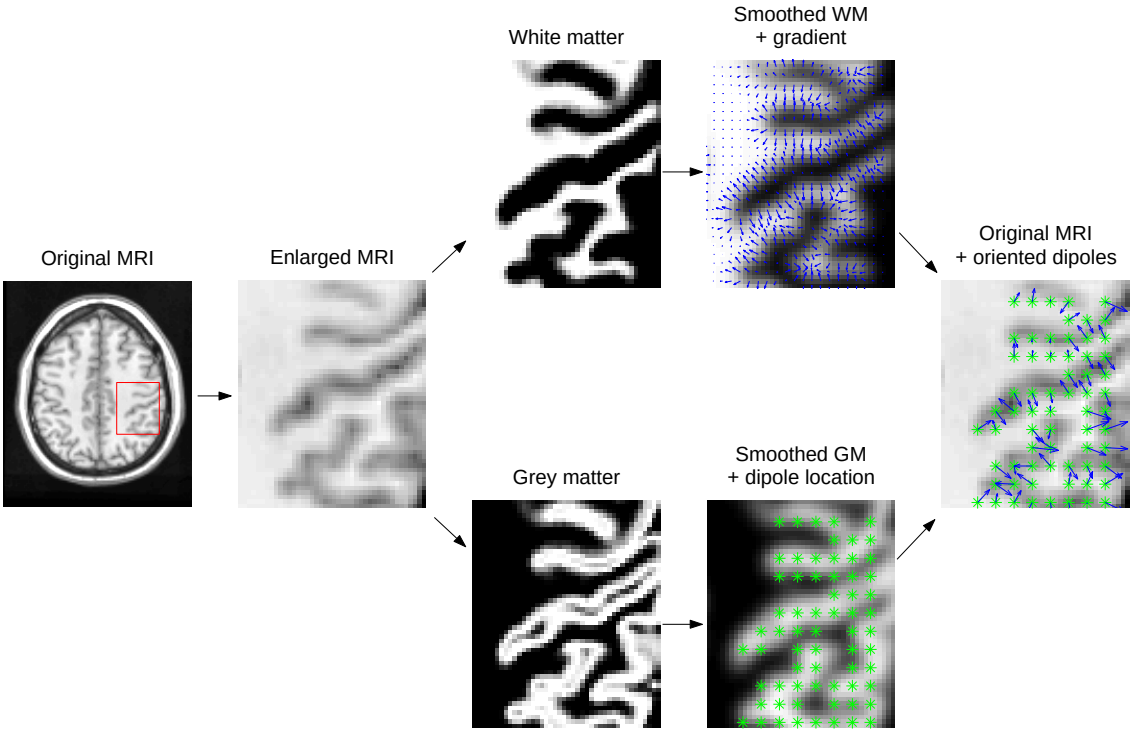

Figure 6.1: Successive steps of MRI processing. The structural MR image is segmented into the white and grey matter volumes. The dipoles are placed within the smoothed grey matter volume and the gradient of the anisotropically smoothed white matter volume is sampled at the dipole locations, providing a distribution of oriented dipoles

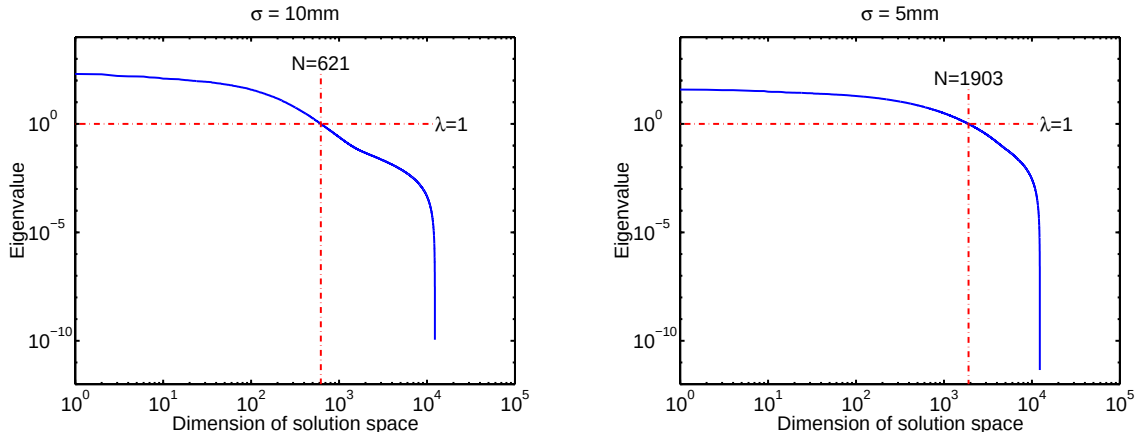

Figure 6.2: Spectrum, on a logarithmic scale, of the normalised eigenvalues of the spatial variance-covariance matrix $\mathbf{C_j} = \mathbf{G}_s^{t/2}\mathbf{D}_s^t\mathbf{D}_s\mathbf{G}_s^{1/2}$, for the two different spatial coherences considered: $\sigma_s = 10$mm (left) and $\sigma_s = 5$mm (right).

$\mathbf{G}_s^{t/2}\mathbf{D}_s^t\mathbf{D}_s\mathbf{G}_s^{1/2}$ with normalised eigenvalues greater than unity were retained to form the basis set $\mathbf{B}_s$. The ensuing spectrum of singular values is shown in figure 6.2.

The original solution space $\mathbf{j}$ of 12300 dimensions was reduced to a space $\mathbf{k}_s$ of 621 and 1903 dimensions for the large ($\sigma_s = 10$mm) and small ($\sigma_s = 5$mm) coherences respectively (a reduction of about 95% and 85%). The dimension of the reduced space corresponds to the number of orthonormal basis functions in $\mathbf{B}_s$. The solutions based on $\mathbf{T}_{\mathbf{B}_s}$ obtained using equation (5.26), will be referred as the "Informed Basis Function" (IBF) solutions of kernel 5mm (**IBF5**) or 10mm (**IBF10**).

6.1.2 Temporal basis functions

In order to assess the solutions with realistically noisy data, as described in section 7.4, free brain activity was recorded on a volunteer. The 61 electrodes were distributed over the scalp according to the head model adopted in section 4.4. The EEG background activity (and noise) was sampled at 250 Hz over epochs of 2 seconds, thus containing $N_t = 500$ time samples. Each epoch was bandpass filtered between 0.05 and 20 Hz by a third order digital Chebychev filter (Rabiner & Gold, 1975). Eventually 150 epochs were averaged to produce a realistic noise time series at each electrode site. The 61×500 matrix $\boldsymbol{\mathcal{E}}$ represents this additive noise.

The prestimulus period was chosen to last 400 ms from -400 ms to 0 ms (100 time samples), thus the window of activity spreads from 0 ms to 1600 ms (400 time samples). The rise and fall periods, 40 ms each, at the extremities of the window of activity were modelled as the ascending and descending part of a Hanning window. The window of activity, defining the diagonal of $\mathbf{G}_t$, is shown on the left of figure 6.4. The temporal coherence matrix $\mathbf{D}_t$ was modelled by a Gaussian convolution matrix, the kernel of the Gaussian function was $\sigma_t = 16$ ms wide (4 points) and is kept constant during the epoch. The coherence around one time instant (600 ms) is shown on the right of figure 6.3. By chosing kernels of different size during the epoch, it would be possible, for example, to

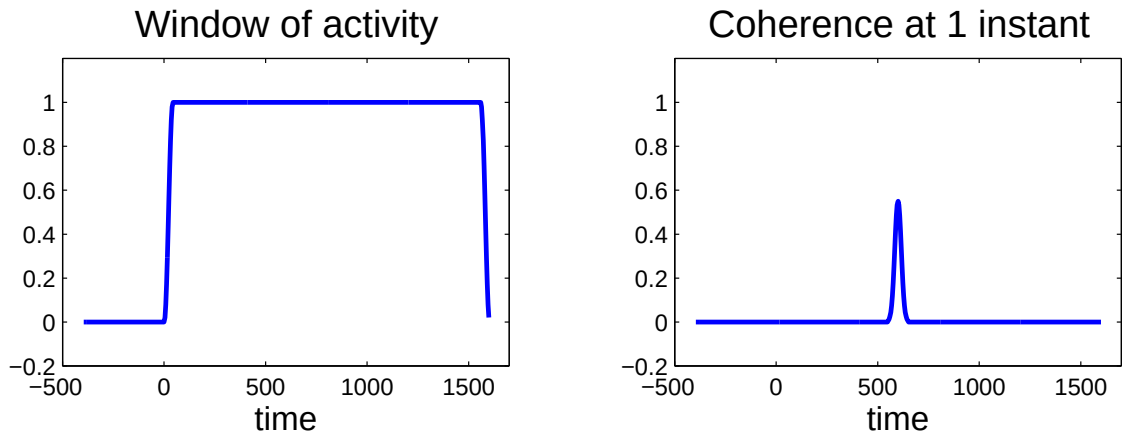

Figure 6.3: Window of activity and temporal coherence used to define the temporal basis functions: The assumed window of activity (left), i.e. the leading diagonal of matrix $\mathbf{G}_t$, spreads from 0 to 1600ms with the prestimulus interval starting at -400ms. The temporal coherence at one time instant (right), here $t = 600$ ms, is a Gaussian function with a kernel of 16 ms.

allow higher frequencies at the beginning of the epoch than at the end of it.

As for the spatial basis function set $\mathbf{B}_s$, the eigenvectors of $\mathbf{G}_t^{1/2}\mathbf{D}_t^t\mathbf{D}_t\mathbf{G}_t^{1/2}$ corresponding to normalised eigenvalues greater than unity were retained to form the basis set $\mathbf{B}_t$. The original 2 seconds epoch composed of 500 samples is reduced to 54 (orthogonal) temporal basis functions as shown in figure 6.4

The covariance matrix $\mathbf{C}_\varepsilon$ of the noise component ε is assumed to be constant throughout the whole epoch. Considering $\mathbf{C}_\varepsilon = \mathrm{cov}(\boldsymbol{\mathcal{E}})$ gives the most efficient estimator before projecting onto the temporal basis set $\mathbf{B}_t$. The most efficient estimator after projecting would be $\mathrm{cov}(\boldsymbol{\mathcal{E}}\mathbf{B}_t)$ but this basis set is very suboptimal for estimating the error (which determines efficiency). Therefore, the covariance matrix of the noise component was calculated as $\mathbf{C}_\varepsilon = \mathrm{cov}(\boldsymbol{\mathcal{E}})$.

6.2 Step 2: Minimum norm solution

6.2.1 Definition of the soft constraints

The (weighted) minimum norm solution depends on the specification of the constraints $\mathbf{H}_{\mathbf{B}_s}$ that enter into equation 5.19. As noted in section 5.4, $\mathbf{H}_{\mathbf{B}_s} \propto \mathbf{C}_{\mathbf{k}_s}^{-1/2}$. Because the solution space has been reduced using the eigenvectors of $\mathbf{C}_\mathbf{j}$, the source prior covariance matrix $\mathbf{C}_{\mathbf{k}_s}$ could simply be its eigenvalues $\mathbf{C}_{\mathbf{k}_s}^{-1/2} = \mathbf{S}_s^{-1}$, where $\mathbf{S}_s$ is the leading diagonal matrix of singular values from 5.12. This simple form for the constraints could be used directly.

However, further "soft" priors on the covariance of the sources can be included by specifying linearly separable components of the prior source covariance matrix, in addition

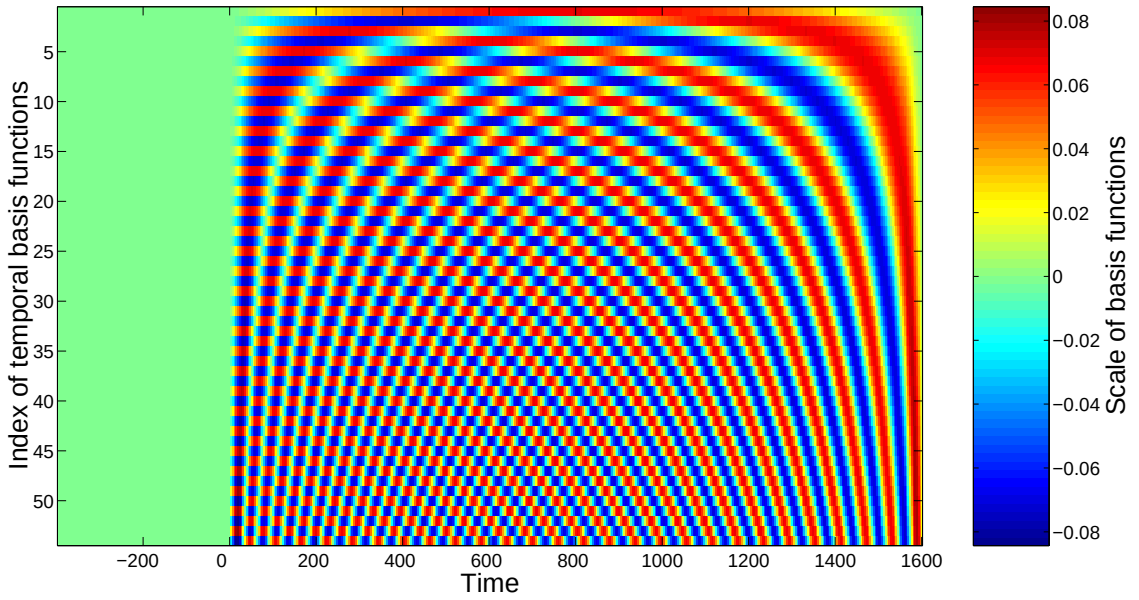

Figure 6.4: Temporal basis function: From 500 time samples, the epoch is modelled by only 54 (orthogonal) basis functions.

to the "hard" constraints used to determine the spatial basis set. Each of these covariance components is controlled by its own hyperparameter. There are two additional constraints considered here.

First, because superficial sources produce a stronger (and more focal) scalp electric potential than deeper sources, shallow sources are "penalised" to ensure that sources are more likely to influence the electric potential equally at the electrodes irrespective of depth (Pascual-Marqui *et al.*, 1994; Pascual-Marqui, 1999; Grave de Peralta Menendez & Gonzalez Andino, 1998). This can be achieved by assuming deeper sources have a larger variance than superficial sources. The depth' is indexed by the norm of the source's lead field. Let the covariance component of this constraint be the diagonal matrix $\mathrm{diag}(\mathbf{L}^t\mathbf{L})^{-1}$. Using this diagonal matrix is equivalent to normalising the column of the lead field matrix.

A second important constraint may be derived from fMRI indices of activation that enter as the constraint $\boldsymbol{\alpha}$, a leading diagonal matrix with elements that reflect the prior probability of whether the source is active or not (here we only allow values of 0, the variance is left unchanged, or 1, the variance is increased according to the value of any hyperparameter). Combining these components, we obtain the following general expression:

$$\mathbf{H}_{\mathbf{B}_s}^t \mathbf{H}_{\mathbf{B}_s} = (\mathbf{B}_s^t \mathbf{C}_\mathbf{j} \mathbf{B}_s)^{-1} \tag{6.3}$$

$$\mathbf{C}_\mathbf{j} = \beta_1 \, \mathbf{G}_s^{t/2} \mathbf{D}_s^t \mathbf{D}_s \mathbf{G}_s^{1/2} + \beta_2 \, \mathrm{diag}(\mathbf{L}^t\mathbf{L})^{-1} + \beta_3 \, \boldsymbol{\alpha} + \ldots \tag{6.4}$$

This formulation, in which the prior covariance is some linear combination of covariance components (structural, depth and functional), is important because the hyperparameters β can be estimated using iterative techniques such as the EM algorithm (Dempster *et al.*, 1977; Harville, 1976).

In the present case, a slightly modified approach is followed and $\mathbf{C_j}$ is defined by:

$$\mathbf{C_j} = \beta_1 \, \mathbf{G}_s^{t/2} \mathbf{D}_s^t \mathbf{D}_s \mathbf{G}_s^{1/2} + \beta_2 \, \left\{ \mathrm{diag}(\mathbf{L}^t\mathbf{L})^{-1} \left(\mathbf{I}_{N_j} + \beta_3 \, \boldsymbol{\alpha} \right)^2 \right\} \tag{6.5}$$

separating clearly the "hard" constraints, used to define the basis functions, and the "soft" constraints.

To illustrate the role of the hyperparameters, a range of fixed values was assumed where $\beta_1 = 0$, $\beta_2 = 1$, and $\beta_3 = \beta$ takes three values, 0, 1 and 4, corresponding to no, weak and strong (fMRI) location priors. The ensuing solutions will be referred to as: "without priors" (or "wp0"), "with weak priors" (or "wp1") and "with strong priors" (or "wp4"). This simplification can easily be interpreted as defining the weighting matrix $\mathbf{H}$ that would be used to constraint the weighted norm of $\mathbf{j}$, see section 5.4, by:

$$(\mathbf{H}^t\mathbf{H})^{-1} = \mathrm{diag}(\mathbf{L}^t\mathbf{L})^{-1} \left(\mathbf{I}_{N_j} + \beta \, \boldsymbol{\alpha} \right)^2 \tag{6.6}$$

By taking β equal to 1 or 4, we are actually assuming that the variance σ^2 of the *a priori* active location (defined by $\boldsymbol{\alpha}$) is 4 or 25 times larger than that for the other locations (if the depth constraint was discounted).

6.2.2 Noise regularisation

The ReML iterative scheme to simultaneously estimate $\mathbf{k}_s$ (or $\mathbf{K}_{st}$) and $\lambda = \theta_1/\theta_2$ is directly implemented as presented in sections 5.5.3, 5.5.4 and 5.5.5. The starting estimate of $\boldsymbol{\theta}$ is taken as $\boldsymbol{\theta} = [1 \; 1]$ in all cases. The stopping criteria of the iterative procedure is based on the difference and relative difference between two successive estimates, λ_n and λ_{n-1}, of λ. The algorithm is stopped if

$$\left| \frac{\lambda_n - \lambda_{n-1}}{\lambda_n} \right| < 10^{-4} \tag{6.7a}$$

$$\text{or} \qquad |\lambda_n - \lambda_{n-1}| < 10^{-8} \tag{6.7b}$$

6.3 Other common solutions

The IBF approach described here was compared in the simulations presented in chapter 7 with two other commonly employed solutions: a Weighted Minimum Norm (WMN) solution and a Maximum Smoothness (MS) solution.

6.3.1 Direct weighted minimum norm solution

The Weighted Minimum Norm solution (WMN solution) is simply the solution of the problem formulated in equation 5.18 given by equations 5.22 and 5.23 or 5.26 where no spatial basis functions are used, i.e. $\mathbf{B}_s = \mathbf{I}_{N_j}$, and so $\mathbf{k}_s = \mathbf{j}$. In the version of the method employed here, the orientation of the dipoles was fixed as with the IBF method, so that

only the amplitude of the dipoles was unknown. The weighting matrix $\mathbf{H}$ was defined as in equation 6.6 and depended (or not) on prior knowledge of the location of active sources.

For the simulations with noise-free data, three different solutions were calculated from equation 5.26 with the same range of β: without priors ($\beta = 0$), with weak priors ($\beta = 1$) or with strong priors ($\beta = 4$). When data with realistic noise were employed, the WMN solution was also calculated from equation 5.23 with the same range of β. As for the IBF solution, the hyperparameter λ was estimated at the same time as the solution using the ReML procedure described in sections 5.5 and 6.2.2.

6.3.2 Maximum smoothness solution

The Maximum Smoothness solution (MS solution) is also a particular case of equation 5.18. The MS solution is thus calculated with the relations 5.22 and 5.23 or 5.26 where the matrix $\mathbf{B}_s$ is the identity matrix and so $\mathbf{k}_s = \mathbf{j}$. As in the original LORETA software (Pascual-Marqui *et al.*, 1994; Pascual-Marqui, 1995, 1999), the orientation of the dipoles was left free. Strength parameters were estimated for three independent and orthogonal dipoles, oriented along the three main axes $\vec{e}_x$, $\vec{e}_y$ and $\vec{e}_z$ and of amplitude $j_{x,i}$, $j_{y,i}$ and $j_{z,i}$, at each source location i such that $\vec{j}_i = [j_{x,i} \;\; j_{y,i} \;\; j_{z,i}]^t$ and $\mathbf{j} = [\vec{j}_1^{\,t} \;\; \vec{j}_2^{\,t} \;\; \dots \;\; \vec{j}_{N_{dip}}^{\,t}]^t$. A single value j_i for the amplitude of the electric activity at each source location i was then obtained by calculating the norm of the resulting dipole $j_i = |\vec{j}_i| = \sqrt{j_{x,i}^2 + j_{y,i}^2 + j_{z,i}^2}$. The source localisation problem is still stated as in equation 5.1 : $\mathbf{v} + \boldsymbol{\varepsilon} = \mathbf{L}_f \mathbf{j}$ but the lead field matrix $\mathbf{L}_f$ is now of size $N_e \times 3N_j$ to accommodate for the free orientations of the dipoles.

The constraint matrix $\mathbf{H}$ is defined as a weighted three-dimensional Laplacian $\mathbf{H} = \mathbf{MW}$. The weighting matrix $\mathbf{W}$ is a $3N_j \times 3N_j$ leading diagonal matrix whose diagonal elements are defined by $\mathbf{w} \otimes [1\ 1\ 1]^t$ where

$$\mathbf{w} = \Big[(\mathbf{I}_{N_j} \otimes [1\ 1\ 1]) \, \mathrm{diag}(\mathbf{L}_f^t \mathbf{L}_f) \Big]^{1/2} \tag{6.8}$$

The $3N_j \times 3N_j$ Laplacian matrix $\mathbf{M}$ is a regularised discrete three-dimensional second order derivative operator defined as in (Pascual-Marqui, 1999) :

$$\mathbf{M} = \frac{6}{d^2} \Big[(\mathbf{P} \otimes \mathbf{I}_3) - \mathbf{I}_{3N_j} \Big] \tag{6.9a}$$

$$\mathbf{P} = \frac{1}{2} \left(\mathbf{I}_{N_j} + \Big[\mathrm{diag}(\mathbf{Q}\, \mathbf{1}_{N_j}) \Big]^{-1} \right) \mathbf{Q} \tag{6.9b}$$

$$Q_{kl} = \begin{cases} \frac{1}{6} \text{ , if } |\vec{r}_k - \vec{r}_l| = d \\ 0 \text{ , otherwise} \end{cases} \tag{6.9c}$$

where d is the inter-grid-point distance, 4 mm here, and Q_{kl} is the element (k, l) of the matrix $\mathbf{Q}$.

This method does **not** provide a way to include prior information. A solution for (assumed) noise-free data was calculated using equation 5.26 and solutions for data with realistic noise were obtained from equation 5.23. As for the IBF and WMN solutions, the regularisation hyperparameter λ was estimated at the same time as the solution using the ReML procedure described in sections 5.5 and 6.2.2. Though, due to the definition of the constraint matrix $\mathbf{H}$, other starting estimates $[1\ 10^6]$ were chosen for $\boldsymbol{\theta}$.

Chapter 7

Simulations and validation

Contents

In this chapter, simulated data are employed to validate and compare the approaches presented in the previous chapter. The IBF solutions as well as the direct WMN and MS solutions were tested with various types of data : single or double simultaneously active sources, with or without location priors, and with noise-free or realistically noisy data. The location priors employed could be either accurate or mislocated (i.e. centred or not on the location of the active source), and of different levels, weak or strong. For the simulations with noisy data, two levels of signal-to-noise ratio were employed, low or high.

7.1 Criteria and simulated data

Two criteria were used to assess and compare the performance of the different methods presented in the previous sections (IBF5, IBF10, WMN and MS solutions).

1. "Localisation Error" (LE) is defined as the distance between the location $\vec{r}_r$ of the maximum (of the absolute value) of the reconstructed source distribution $\mathbf{j}_r$ and the location $\vec{r}_o$ of the original source set $\mathbf{j}_o$:

$$\mathrm{LE} = |\vec{r}_r - \vec{r}_o| \tag{7.1}$$

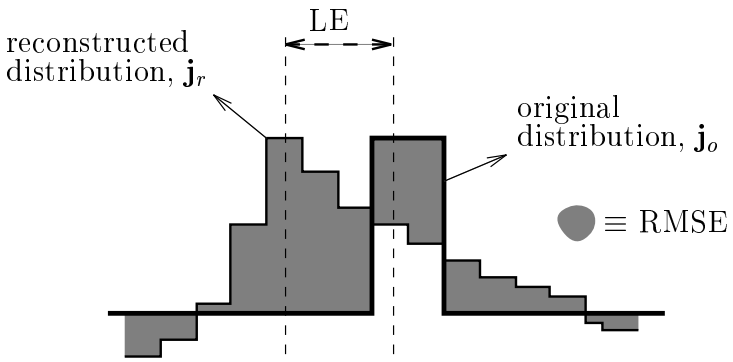

Figure 7.1: Two-dimensional example of Localisation Error (LE) and Root Mean Square Error (RMSE). LE is the distance between $\mathbf{j}_r$ and $\mathbf{j}_o$ maxima and RMSE is the integral of the difference between $\mathbf{j}_r$ and $\mathbf{j}_o$ (grey shade).

2. "Root Mean Square Error" (RMSE) is defined as the norm of the difference between the reconstructed source distribution $\mathbf{j}_r$ and the original source set $\mathbf{j}_o$:

$$\mathrm{RMSE} = \sqrt{\sum_{l=1}^{N_j} \left(\frac{j_{r,l}}{\max(|\mathbf{j}_r|)} - \frac{j_{o,l}}{\max(|\mathbf{j}_o|)} \right)^2} \tag{7.2}$$

where $j_{\bullet,l}$ is the l^{th} element of $\mathbf{j}_\bullet$.

The "Localisation Error" (LE) provides a measure of the localisation accuracy of the reconstruction method, as shown in figure 7.1. A small value of LE indicates that the location of the original source was well recovered. The "Root Mean Square Error" (RMSE) measures the "goodness of fit" of the reconstruction. Figure 7.1 shows that a small RMSE indicates a small discrepancy between the original and reconstructed source distributions. The RMSE is only useful to further compare two solutions that have approximately the same LE. Indeed, if both solutions have almost the same LE, the one with the smaller RMSE should be preferred as the reconstructed source is then more focal. A very focal reconstructed source with a large LE will have a smaller RMSE than a blurred reconstructed source with a small LE, but the latter solution, although over smoothed, provides at least some location information.

For the simulations employing instantaneous noise-free data, the sources $\mathbf{j}_o$ were generated at randomly selected locations within the head model described in section 4.4. Each source comprised a set of connected dipoles within a 7mm radius of a "central" dipole. For each source $\mathbf{j}_o$, the potential $\mathbf{v}_o$ at the electrodes was generated with the equation 5.6. Information about prior location was provided as a sphere of 12mm radius, and dipoles within this volume were defined as being *a priori* active sources, i.e. the corresponding diagonal elements of $\boldsymbol{\alpha}$ (see section 6.2) were set to 1.

For the data with realistic noise, instantaneous sources $\mathbf{j}_o$ were generated at randomly selected locations, then each source $\mathbf{j}_o$ was modulated over time to generate a time-extended $N_j \times N_t$ data set $\mathbf{J}_o$. The time course adopted for all the sources is shown in figure 7.2. The noise-free potential $\mathbf{V}$ at the electrodes was then generated with the equation 5.6. The data with realistic noise $\mathbf{V}_\varepsilon$ were eventually obtained by adding the

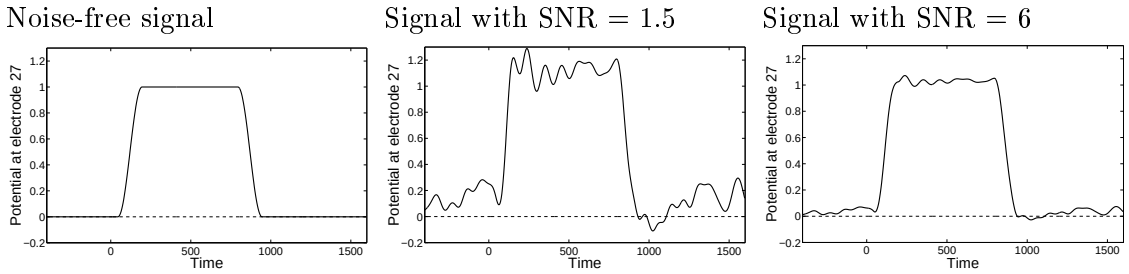

Figure 7.2: Time course of the sources and example of data with realistic noise. Free brain activity is added to the noise-free signal at one electrode (left), and all the sources have the same time course. The level of noise is scaled at two different levels in order to produce two data sets with two signal-to-noise ratio (SNR) : SNR=1.5 (middle) and SNR=6 (right).

averaged free brain activity $\boldsymbol{\mathcal{E}}$ to $\mathbf{V}$: $\mathbf{V}_{\boldsymbol{\mathcal{E}}} = \mathbf{V} + \boldsymbol{\mathcal{E}}$. The averaged free brain activity $\boldsymbol{\mathcal{E}}$ was scaled to achieved two different levels of signal-to-noise ratio (SNR). The SNR was defined as the ratio between the power of the potential $\mathbf{V}$ over the scalp, i.e. at the electrodes, and the average (over time) power of the free brain activity $\boldsymbol{\mathcal{E}}$ over the scalp. In one case, the SNR was kept low at 1.5 and, in the other case, it was set high at 6. The potential at one electrode over time with these two SNR is shown in figure 7.2. The location priors were produced as for the instantaneous noise-free simulations.

7.2 Simulations with a single active source, noise free

The case of single active sources is considered first. For each source set, LE and RMSE were calculated for the IBF5, IBF10 and WMN methods in each of the following cases : 1. without priors, 2. with priors (weak and strong) centred on the original source (accurate priors), 3. with priors (weak and strong) placed anywhere in the volume (incorrect priors). As explained in section 6.3, no prior about the location of the sources can be included in the MS method, therefore the same solution was used for all the simulations. The results of a typical simulation are shown in figure 7.3.

7.2.1 Solution without location priors

The whole solution space was evaluated by generating a source set around each of the 12300 dipoles in the model. The results obtained for LE and RMSE are summarised in figure 7.4.

The IBF10, IBF5 and MS solutions have approximately the same localisation ability, with about 80% of the sources recovered within 20mm of their original location. The LE of the WMN solution is spread over a much larger range, and thus, although its RMSE is smaller than any other method, its poor localisation ability makes it a less efficient method.

The RMSE of the MS solution is on average larger than that of the IBF5 and IBF10

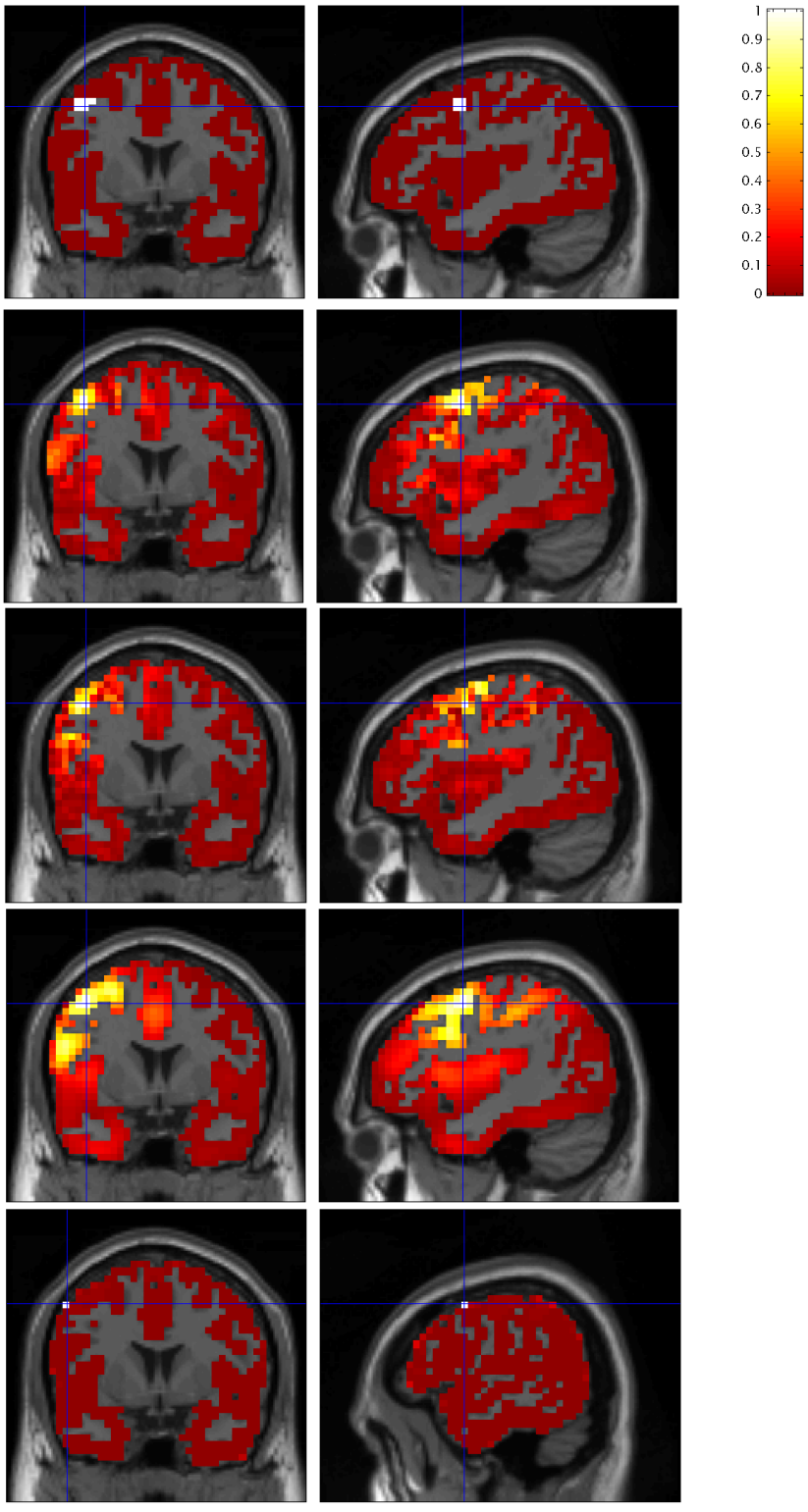

Figure 7.3: Example of a single active source reconstruction : The original source set is shown at the top. Below are the (absolute value of the) source reconstructions obtained with the four solutions presented (IBF10, IBF5, MS and MS) without priors. The amplitude of the sources was normalised between 0 and 1 for all the solutions.

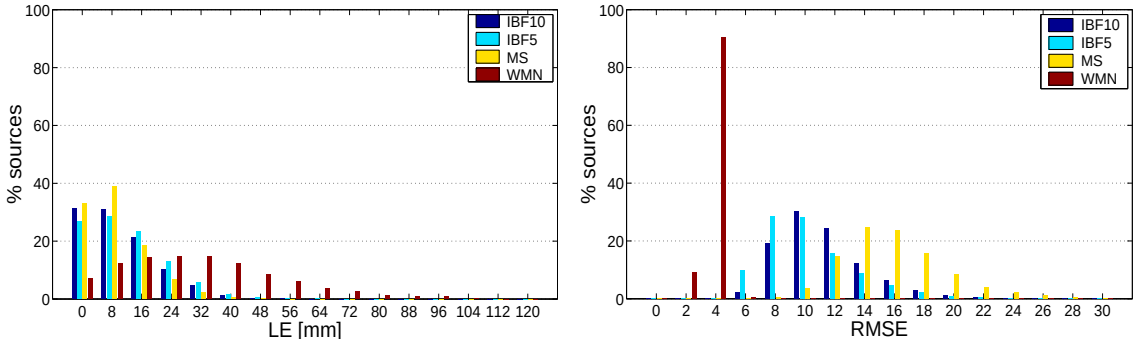

Figure 7.4: Localisation Error (LE), left, and Root Mean Square Error (RMSE), right, for the four solutions applied to the simple source simulated data: IBF10, IBF5, MS and WMN solutions, all without location priors.

solutions. This result reflects the fact that the MS solution is overly smoothed. Thus the IBF5 and IBF10 solutions are able to reconstruct focal activity more accurately. As less coherence is imposed on the IBF5 solution, it is less "blurred" and thus the IBF5 solution yelds somewhat smaller RMSE than does the IBF10 solution.

7.2.2 Solution with accurate location priors

Because of computational limits it was not possible to assess the entire solution space with *a priori* location information (a new solution must be calculated for every set of priors). Therefore a set of 100 randomly selected sources were employed in this section. (For this reason, the results obtained for the MS solution are slightly different from those obtained in the previous section). The results obtained for LE and RMSE with weak and strong priors are summarised in figure 7.5.

The inclusion of prior location information greatly improved the performance of the IBF5, IBF10 and WMN solutions, which all outperformed the MS solution. The IBF5 solution performed best of all, but both IBF solutions outperformed the WMN solution, particularly when the prior information was entered as a weak constraint only. With the IBF solutions, the reconstructed activity was more focal (smaller RMSE) and more than 80% of the sources were recovered within 4mm of their original location.

7.2.3 Solution with incorrect location priors

A set of 100 locations were randomly selected to provide prior location information. Corresponding IBF10, IBF5 and WMN solutions were then produced for the two levels of location constraint (weak and strong). Independently, 200 source sets $\mathbf{j}_o$ were randomly generated and their corresponding electrode potentials calculated. For every combination of prior location and original source $\mathbf{j}_o$, the source distribution $\mathbf{j}_r$ was then reconstructed and the LE and RMSE were calculated.

The prior mislocation was defined as the distance between the location of the original

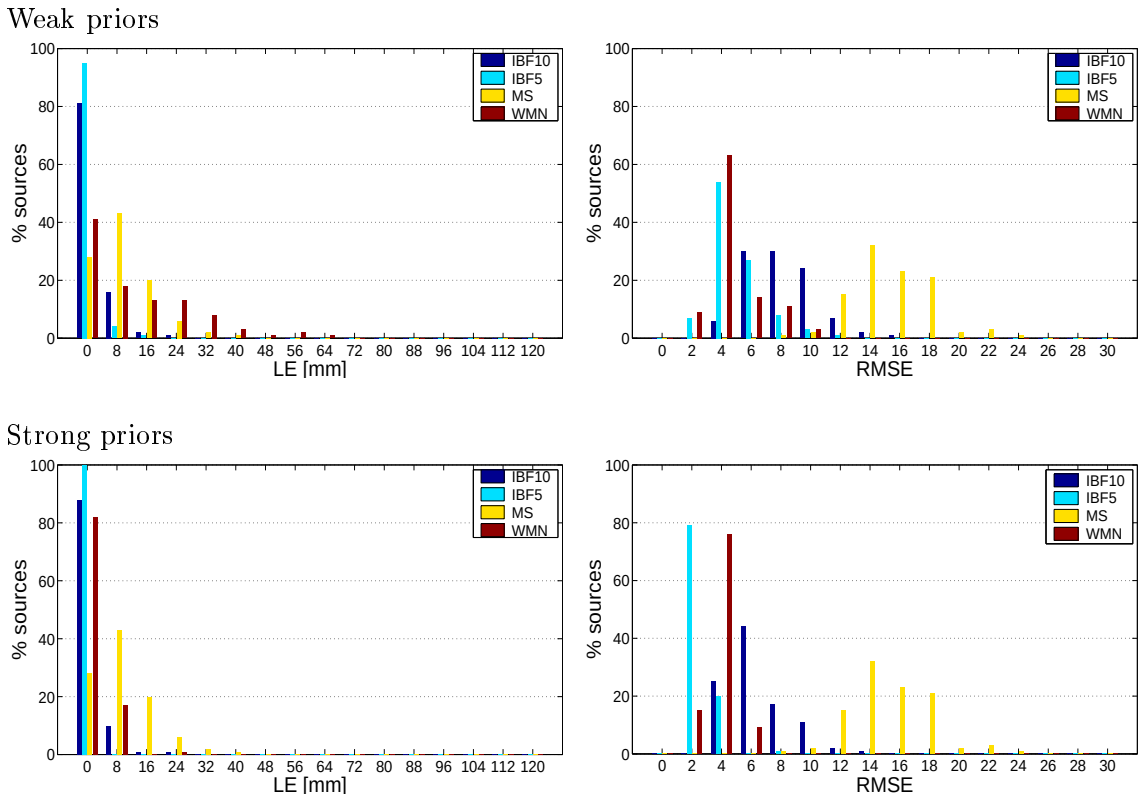

Figure 7.5: Localisation Error (LE), left, and Root Mean Square Error (RMSE), right, for the four solutions (IBF10, IBF5, MS and WMN) applied to the simple source simulated data, with location priors: weak (top) and strong (bottom). The MS solution does not incorporate prior location information.

source set and the corresponding prior information. The prior mislocation was divided into four "bands" of 30mm width: 1–30mm, 31–60mm, 61–90mm and 91-120mm. Within each band of prior mislocation, a "maximum LE" was calculated, such that at least 80% of the sources were recovered with this LE at most (for simplicity, the LE was also divided in bands: 0–4mm, 4–12mm, 12–20mm, etc). The mean RMSE for each band of prior mislocation was calculated as well. For reference, the results obtained in the two previous sections are included in the table. The results are presented in table 7.1.

With weak priors, the LE of both IBF10 and IBF5 solutions were similar to the case where no priors were employed. Thus the prior mislocation had rather little effect on the solution. By contrast, with strong priors, the IBF solutions were substantially affected by the incorrect prior location. This effect was more important for the IBF5 solution than the IBF10 with the difference being expressed mainly for the smaller prior mislocation. In general the WMN solution behaved poorly.

7.3 Simulations with two active sources, noise free

We consider in this section the case of two simultaneously active source sets of equal strength. Two factors influence the reconstruction of two sources: the distance between them and their relative power in measurement space (i.e. at the electrodes). The power of a source set (at the electrodes) is calculated from the sum of squares of the electric potential generated at the electrodes. The power of proximate sources is very similar because their lead fields are almost collinear (although the orientation of the sources can still have some influence on the power of the electric field at the electrodes) and they might be difficult to distinguish in the reconstruction because of their proximity. Distant sources should be more easily distinguishable but their relative power can vary widely depending on their relative depths in the brain and their orientation, rendering their localisation more difficult.

The methods presented in the previous sections (IBF5, IBF10, WMN and MS solutions) were applied to simulated data using different ranges of source separation and power. The separation was divided into five "bands" of 30mm width (as in section 7.2.3 for the prior mislocation): 1–30mm, 31–60mm, 61–90mm and 91-120mm. The ensuing relative power of source pairs was used to further stratify the source configurations into five "bands" according to a logarithmic scale: $10^{0.0}$–$10^{0.1}$, $10^{0.1}$–$10^{0.2}$, $10^{0.2}$–$10^{0.3}$, $10^{0.3}$–$10^{0.4}$ and $10^{0.4}$–$10^{0.5}$, i.e. 1.00–1.26, 1.26–1.58, 1.58–2.00, 2.00–2.51 and 2.51–3.16. Obviously all combinations of separation and relative power do not occur with equal source strengths, e.g. separation of 1-30mm and relative power 2.51–3.16 cannot be obtained, and in these cases no results are shown. For each of the remaining combinations, 100 pairs of sources were selected randomly, data generated and the activity reconstructed.

The RMSE was calculated with equation 7.2. As two sources were employed in these simulations, the LE was calculated as follows. For each pair of sources $\mathbf{j}_{o1}$ and $\mathbf{j}_{o2}$, centred at location $\mathbf{r}_1$ and $\mathbf{r}_2$, the original source set $\mathbf{j}_o$ was the sum of $\mathbf{j}_{o1}/\|\mathbf{j}_{o1}\|$ and $\mathbf{j}_{o2}/\|\mathbf{j}_{o2}\|$, and the potential at the electrodes was then generated using 5.6. The absolute value of the reconstructed activity $\mathbf{j}_r$ (for the MS solution, the 2-norm of the three components at each location was used instead of the absolute value) was thresholded at 50% of its maximum, leaving a set of suprathreshold clusters of active sources. The location $\mathbf{r}_b$ of the maximum

Table 7.1: Localisation Error (LE) and Root Mean Square Error (RMSE) for different degrees of mislocation of the location priors. Only the three solutions in which location priors can be incorporated (IBF10, IBF5 and WMN) are tested. The prior mislocation is defined as the distance between the location of the original source set and the corresponding prior. The prior mislocation was divided into four "bands" of 30mm width : 1–30mm, 31–60mm, 61–90mm and 91-120mm. The localisation error is expressed as the maximum LE required to recover at least 80% of the sources. (The actual percentage of sources recovered within this LE are given in brackets.) The RMSE is the mean RMSE within this band of mislocation. For comparison the values obtained for the MS solution are the following : within a LE of 20mm, 91% of the sources are recovered and the mean RMSE is 16.2.

	Priors mislocation	Priors strength	IBF10	IBF5	WMN
max LE [mm]	No mislocation	no	20 (86%)	20 (85%)	44 (85%)
		weak	4 (90%)	4 (95%)	28 (85%)
		strong	4 (97%)	4 (100%)	4 (82%)
	1–30mm	weak	20 (86.3%)	20 (80.2%)	44 (84.2%)
		strong	20 (81.8%)	28 (95.8%)	44 (85.5%)
	31–60mm	weak	20 (80.9%)	28 (85.7%)	52 (85.4%)
		strong	28 (88.0%)	44 (83.0%)	52 (85.1%)
	61-90mm	weak	20 (82.5%)	20 (81.5%)	52 (85.6%)
		strong	20 (82.4%)	28 (85.2%)	52 (83.9%)
	91–120mm	weak	20 (88.1%)	20 (87.0%)	44 (86.3%)
		strong	20 (88.1%)	20 (86.7%)	44 (85.9%)
mean RMSE	No mislocation	no	11.0	10.3	3.6
		weak	8.2	5.0	4.7
		strong	6.5	2.7	3.8
	1–30mm	weak	11.0	9.5	3.6
		strong	10.8	8.5	3.6
	31–60mm	weak	11.1	9.8	3.6
		strong	11.0	8.9	3.6
	61-90mm	weak	10.9	9.7	3.6
		strong	10.9	9.1	3.6
	91–120mm	weak	10.9	9.6	3.6
		strong	10.8	9.0	3.6

of each cluster (cluster peak) was compared to $\mathbf{r}_1$ and $\mathbf{r}_2$. According to the number and location of the maxima, three cases are possible:

- only one peak survived after thresholding. In this case only one value can be attributed to the LE, the number of original sources recovered (NRec) is 1 and the number of spurious reconstructed sources (NSpur) is 0.
- many peaks (≥ 2) but all closer to $\mathbf{r}_1$ than $\mathbf{r}_2$. Now only one value (the minimum distance between $\mathbf{r}_b$ and $\mathbf{r}_1$) can be attributed to the LE, NRec is 1 and NSpur is equal to the number of clusters minus 1.
- many peaks (≥ 2) that are spread around $\mathbf{r}_1$ and $\mathbf{r}_2$. Here two values (the minimum distance between the $\mathbf{r}_b$'s and $\mathbf{r}_1$ and $\mathbf{r}_2$) can be attributed to the LE, NRec is 2 and NSpur is equal to the number of clusters minus 2.

As well as the LE and the RMSE criteria, the number of original sources recovered (NRec) and the number of spurious reconstructed sources (NSpur) were assessed for each reconstruction method. Nrec provides us with the number of sources actually recovered while NSpur indicates how many spurious (and difficult to interpret) clusters were left after thresholding. An example of the reconstructed activities is presented in figure 7.6.

7.3.1 Solution without location priors

Here the solutions were calculated without prior knowledge about the location of active sources. The number of original sources recovered (NRec) varied considerably among the methods and for the different degrees of source separation and relative power. The values of NRec are summarised in table 7.2.

For every method and source separation, the risk of recovering only one source (NRec=1) increased with the difference of relative power of the sources. Over all, the two sources were recovered in only 48% 47% 40% and 56% of the cases for the IBF10, IBF5, MS and WMN solution respectively.

The values of LE, NSpur and RMSE seemed to depend mainly on the number of sources recovered (NRec = 1 or NRec = 2), and varied little according to the distance between sources or their relative power. Therefore, the values of NSpur and RMSE were averaged over all conditions, either for NRec=1 or NRec=2. The LE was also considered differently according to the value of NRec. As in section 7.2.3, a "maximum LE" was calculated such that at least 80% of the sources were recovered within this LE. When NRec=2, two values were available for LE, a "small" one and "large" one. As the order of the sources within each pair is arbitrary, two "maximum LE" were calculated, one for the "small LE" (best case) and one for the "large LE" (worst case). These results are summarised in table 7.3.

The maximum LE obtained were smaller than that observed for single sources, compare the first line of table 7.1 with table 7.3, especially for the cases of NRec=1 and NRec=2 (for the "small" LE). The difference is due to the way the LE is measured. Whereas previously (sections 7.2.1 and 7.2.2), only the maximum of the absolute value of the reconstructed activity was used, here maxima of lesser amplitude were also considered.

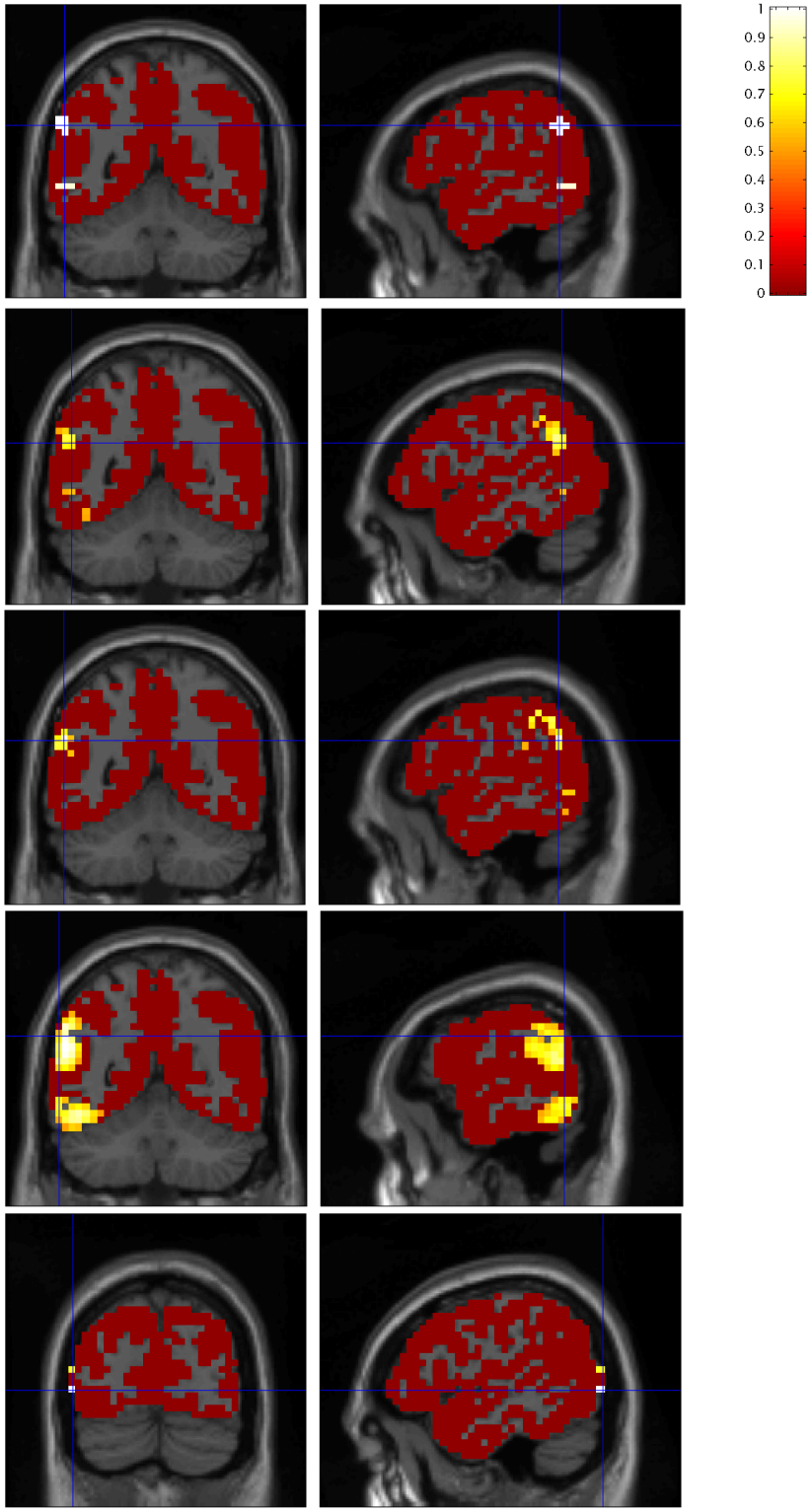

Figure 7.6: Example of reconstructions of two simultaneously active sources : The original source sets are shown at the top. Below are the source reconstructions (thresholded absolute value) obtained with the four solutions presented (IBF10, IBF5, MS and WMN) without location priors. The amplitude of the sources was normalised between 0 and 1 for all the solutions.

Table 7.2: Percentage of source reconstructions where both sources were recovered (NRec=2). The IBF10, IBF5, MS and WMN solutions, without priors, are tested for different degrees of source separation and relative power. In each cell of the table, the top two figures correspond to the IBF10 and IBF5 solutions and the bottom two figures, to the MS and WMN solutions respectively. When data could not be generated (see main text for justification), the values are replaced by "n.a.".

	Source separation							
Relative power	1-30mm		31-60mm		61-90mm		91-120mm	
$10^{0.0}$-$10^{0.1}$	78	84	62	56	56	50	65	58
	39	66	53	69	51	66	63	67
$10^{0.1}$-$10^{0.2}$	74	76	53	53	51	49	28	25
	36	68	51	62	51	68	37	42
$10^{0.2}$-$10^{0.3}$	72	75	46	39	40	41	33	39
	41	58	38	54	40	55	37	42
$10^{0.3}$-$10^{0.4}$	n.a.		35	36	30	24	18	18
			27	54	22	44	20	39
$10^{0.4}$-$10^{0.5}$	n.a.		n.a.		32	29	n.a.	
					30	47		

Solutions

IBF10	IBF5
MS	WMN

Table 7.3: Max LE and mean values of NSpur and RMSE when NRec=1 or NRec=2. The IBF10, IBF5, MS and WMN solutions, without priors, are tested. NSpur and RMSE were averaged over all the conditions. The LE is expressed as the maximum LE to recover at least 80% of the sources within this LE, the actual percentage of sources recovered within this "max LE" is in brackets. For NRec=2, two values were calculated, one for the smallest LE and one for the largest LE of the pair of sources.

		IBF10	IBF5	MS	WMN
max LE [mm]	NRec=1	12 (96%)	12 (98%)	12 (82%)	28 (82%)
	NRec=2	12 (98%)	12 (99%)	12 (92%)	28 (87%)
		20 (88%)	20 (90%)	20 (83%)	44 (81%)
mean NSpur	NRec=1	2.38	5.12	0.53	1.83
	NRec=2	5.50	10.83	1.25	4.39
mean RMSE	NRec=1	9.93	9.18	14.68	4.31
	NRec=2	12.94	12.01	18.51	4.65

As the smoothness of the IBF solutions is less than that of MS solution, close sources can be better distinguished with the former method. The IBF solutions were less likely to miss a source but at the cost of recovering more spuriously active sources than the MS solution. This renders the interpretation of the reconstructed activity more difficult (even if the clusters are generally spread around the location of the original sources) but a higher threshold could be used (with the risk of missing an original source). The small value of NSpur (< 1) for the MS solution when only one source is recovered shows that a single cluster was left after thresholding in many cases but there were still few cases where there was spurious reconstructed activity.

The figures obtained for the RMSE correspond to that observed for single sources (see top row of table 7.1). The RMSE is slightly larger but this could be explained by the fact that there were two active sources instead of one.

7.3.2 Solution with two location priors

In this section, the same set of sources as in section 7.3.1 was used but the solutions (IBF5, IBF10 and WMN only) were calculated with (weak and strong) prior knowledge about the location of both active sources. Similarly to the case without priors, section 7.3.1, the number of sources recovered (NRec) varied greatly between conditions (source separation and relative power) and type of solution. The values of NRec are summarised in table 7.4.

For the IBF5 solution with strong priors, the proportion of cases where only one source out of two was recovered was only slightly reduced, compared to the simulations without prior location (except for sources separated by less than 30mm). Otherwise the risk of recovering only one source (NRec=1) is larger when priors are included than without, as can be seen by comparing table 7.2 and 7.4. Nevertheless, the two sources are recovered more often with strong priors than weak priors, especially for distant sources. Over all, two sources are recovered in 42%, 38% and 34% of the cases with weak priors and in 43%, 50% and 45% of the cases with strong priors for the IBF10, IBF5 and WMN solutions respectively.

The values of LE, NSpur and RMSE vary little between conditions (source distance and relative power) but depend instead on the number of sources recovered (NRec=1 or NRec=2). Therefore, the values of LE, NSpur and RMSE were averaged and presented like in section 7.3.1. These results are summarised in table 7.5.

The inclusion of location priors greatly improved the LE, as was also the case in the simulations with only one active source described in section 7.2.2. With weak or strong priors, both IBF solutions reconstructed most of the sources within 4mm of their original locations, except in the "worst case" of the IBF10 solution with weak priors. The LE of the WMN solution was improved by the inclusion of weak priors but only reached the level of the IBF solutions with the use of strong priors. All these figures are in agreement with those obtained for the simulations with only one active source, see top row of table 7.1.

The number of spurious reconstructed sources (NSpur) was also greatly reduced by the introduction of location priors. There was still some spurious reconstructed activity but much less than when no priors were included, as can be seen by comparing table 7.3 and

Table 7.4: Percentage of reconstructed sources where both sources were recovered (NRec=2). The IBF10, IBF5 and WMN solutions, with location priors (weak and strong), were tested for different degrees of source separation and relative power. In each cell of the table, the figures in the top row corresponds to the IBF10 solution with weak (left) and strong (right) priors, in the middle row to the IBF5 solution with weak (left) and strong (right) priors, and in the the bottom row to the WMN solution with weak (left) and strong (right) priors respectively. When data could not be generated (see main text for justification), the values are replaced by "n.a.".

	Source separation							
Relative power	1-30mm		31-60mm		61-90mm		91-120mm	
$10^{0.0}$-$10^{0.1}$	61	52	53	56	54	55	63	64
	52	62	50	65	51	65	57	72
	55	55	38	52	33	47	44	58
$10^{0.1}$-$10^{0.2}$	54	49	43	50	52	53	27	31
	47	55	43	61	41	58	26	42
	51	49	34	50	34	53	26	38
$10^{0.2}$-$10^{0.3}$	52	43	32	34	39	39	41	43
	53	56	26	42	38	45	34	50
	49	42	27	32	29	43	37	53
$10^{0.3}$-$10^{0.4}$	n.a.		27	33	26	29	18	23
			29	32	20	35	21	31
			25	38	21	39	25	29
$10^{0.4}$-$10^{0.5}$	n.a.		n.a.		25	27	n.a.	
					20	27		
					21	33		

	priors	
IBF10	weak	strong
IBF5	weak	strong
WMN	weak	strong

Table 7.5: Max LE and mean values of NSpur and RMSE for NRec=1 and NRec=2. The IBF10, IBF5 and WMN solutions, with location priors (weak and strong), were tested. NSpur and RMSE were averaged for NRec=1 and NRec=2 separately. The LE is expressed as the maximum LE to recover at least 80% of the sources within this LE and the actual percentage of sources recovered. For NRec=2, two values were calculated, one for the smallest LE and one for the largest LE of the pair of sources.

	Priors	Nrec	IBF10	IBF5	WMN
max LE [mm]	weak	1	4 (92%)	4 (100%)	12 (86%)
		2	4 (97%) 12 (94%)	4 (100%) 4 (98%)	4 (94%) 28 (86%)
	strong	1	4 (98%)	4 (100%)	4 (98%)
		2	4 (100%) 4 (90%)	4 (100%) 4 (100%)	4 (99%) 4 (88%)
mean NSpur	weak	1	0.57	0.16	1.41
		2	2.22	0.72	3.34
	strong	1	0.161	0.01	0.76
		2	0.75	0.05	1.61
mean RMSE	weak	1	7.27	5.08	5.34
		2	9.97	6.45	6.16
	strong	1	5.95	3.33	4.40
		2	7.76	3.45	4.77

7.5. The largest benefit was enjoyed by the IBF5 solution. With strong priors, the IBF5 solution gave almost the ideal figures of NSpur=0 for NRec=1 (one source is missing but there is no spurious reconstructed activity) and NRec=2 (the two sources are recovered without spurious activity). The WMN solution showed significantly smaller NSpur only for the strong priors but these values were still worse than those of the IBF solution.

The RMSE values were also improved by the inclusion of priors and proved to be similar to those obtained with only one active source to reconstruct, as shown in table 7.1.

7.4 Simulations with a single source, with realistic noise

In this section the case of a single active source is considered but, contrary to sections 7.2 and 7.3, time extended data with realistic noise are used. The aim of this section is to study the influence of the level of noise in the data (signal-to-noise ratio or SNR) on the performance of the different source localisation methods. Even though the regularisation hyperparameter λ was optimally estimated, it can be expected that with low SNR the performances of the different methods will be reduced compared to the ideal noise-free case. A set of 100 locations were randomly selected to generate the original source sets $\mathbf{J}_o$ and corresponding data sets $\mathbf{V}_{\boldsymbol{\mathcal{E}}} = \mathbf{V} + \boldsymbol{\mathcal{E}}$.

The IBF10 and IBF5 solutions were calculated using the spatial and temporal basis functions calculated in sections 6.1.1 and 6.1.2. The hyperparameter λ was estimated for

each data set with the ReML iterative procedure. For the WMN and MS solutions no basis functions (even temporal) were employed but the hyperparameter λ was still obtained through the ReML algorithm. In the literature (Pascual-Marqui *et al.*, 1994; Pascual-Marqui, 1999), the MS solution is usually presented and implemented in the LORETA software (Pascual-Marqui, 1998) for the ideal noise-free case using equation 5.26. Although Pascual-Marqui (1995) suggested employing noise regularisation by taking $\lambda \neq 0$, no method for estimating λ was provided. The IBF10, IBF5 and WMN were tested without location priors and with weak and strong location priors.

The LE and RMSE cannot simply be calculated with the relations given in 7.1 and 7.2 but the same idea was adapted to compare the original source set $\mathbf{J}_o$ with the reconstructed source set $\mathbf{J}_r = [\mathbf{j}_{r,1}\ \mathbf{j}_{r,2}\ \ldots\ \mathbf{j}_{r,N_t}]$. In order to obtain a single value of LE for each pair of source sets $(\mathbf{J}_o, \mathbf{J}_r)$, the following procedure was adopted: Considering $j_{r,max}$, the amplitude of the largest (in absolute value) dipole in $\mathbf{J}_r$, only instantaneous reconstructed sources $\mathbf{j}_{r,i}$ including at least one dipole of amplitude (in absolute value) greater than 85% of $j_{r,max}$ are taken into account. For each of those selected instantaneous reconstructions $\mathbf{j}_{r,i}$, the LE_i is calculated as in 7.1. Finally the largest value of LE_i is kept as the "worst case LE" for the data set. Similarly to equation 7.2, the RMSE is defined as

$$\mathrm{RMSE} = \|\mathbf{J}_r^* - \mathbf{J}_o^*\| \tag{7.3}$$

where $\mathbf{J}_r^* = \mathbf{J}_r / j_{r,max}$ and $\mathbf{J}_o^* = \mathbf{J}_o / j_{o,max}$.

7.4.1 Solution without location priors

Here the solutions were calculated without prior knowledge about the location of active sources. For each source set, the hyperparameter λ was estimated for the two levels of noise (low and high SNR) and the LE and RMSE were calculated. The histograms of the values of LE and the estimated λ are shown in figure 7.7. As the values of λ vary on a large scale, its logarithm in base 10 ($\log_{10}\lambda$) was used. For some simulations, when the SNR was high, the value of λ tended to zero. Those solutions correspond to equation 5.26 used in the noise-free case, where the data minimises the constraint after perfectly fitting the model. Those values of λ were not considered for the histogram plot as $\lim_{\lambda\to 0} \log_{10}\lambda = -\infty$.

As in sections 7.2.3 and 7.3, a "maximum LE" (max LE) was calculated with the LE of all the simulations, such that at least 80% of the sources were recovered within this maxLE. The maxLE, mean value of RMSE and of $\log_{10}\lambda$ are summarised in table 7.6 for the two levels of SNR. When the value of λ tended to zero, those values were not included to calculate the mean of $\log_{10}\lambda$. In table 7.6, the percentage of cases where λ was different from zero is written under brackets after the mean value of $\log_{10}\lambda$.

Considering the LE, the IBF10, IBF5 and MS solutions with noise regularisation had results slightlyworse than in the noise-free case as can be seen by comparing figure 7.7 with figure 7.4 and table 7.6 with the first line of table 7.1. The noise component included in the data could thus be appropriately taken into account and accommodated. By contrast, the MS solution without regularisation was clearly inefficient for low SNR and only performed slightly better for high SNR. The WMN solution without location priors remained sensitive to noise even with the inclusion of noise regularisation and its performance was much worse than that in the noise-free simulations. The WMN solution without location priors was unable to localise the source of the signal.

Low SNR

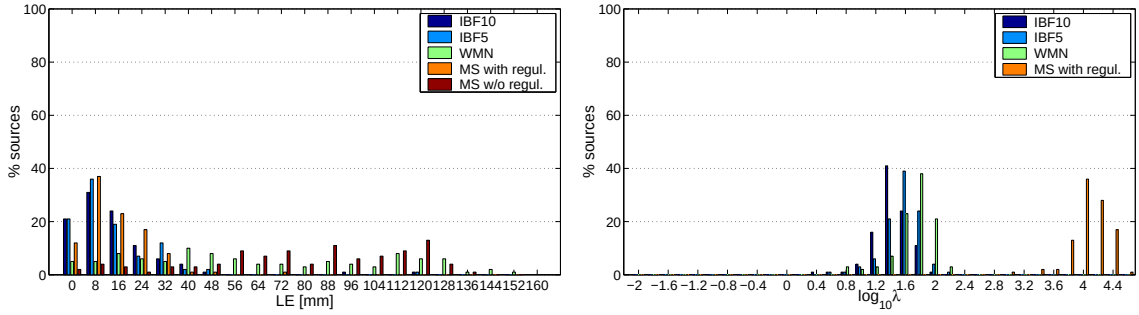

High SNR

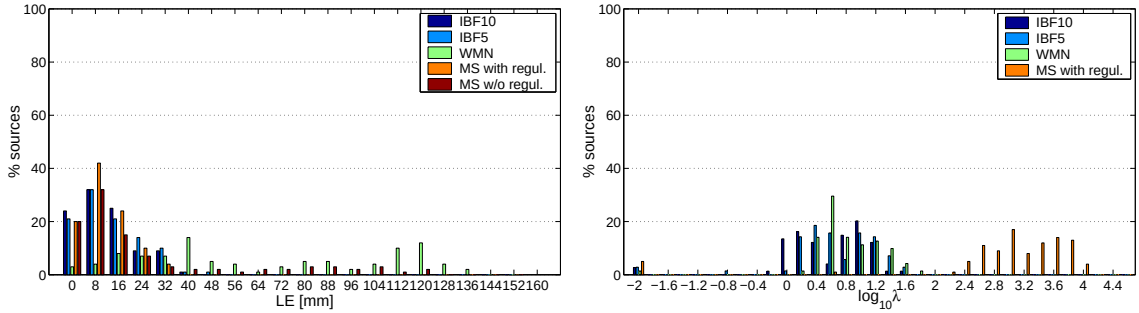

Figure 7.7: LE, left, and $\log_{10}\lambda$, right, for the four solutions (IBF10, IBF5, WMN and MS with and without noise regularisation) for two levels of signal-to-noise ratio (SNR), low SNR (top) and high SNR (bottom), applied to the simple source simulated data with realistic noise.

Table 7.6: Max LE and mean values of RMSE and $\log_{10}\lambda$. The IBF10, IBF5, WMN, MS (with and without noise regularisation) solutions were tested for two levels of signal-to-noise ratio (SNR), low and high. The LE is expressed as the maximum LE to recover at least 80% of the sources within this LE, the actual percentage of sources recovered within this "max LE" is in brackets. The mean of $\log_{10}\lambda$ only takes into account values of λ different from 0, the percentage of cases where $\lambda \neq 0$ is in brackets.

	SNR	IBF10	IBF5	WMN	MS with regul.	MS w/o regul.
max LE [mm]	low	28 (87%)	28 (83%)	116 (84%)	28 (89%)	116 (82%)
	high	20 (81%)	28 (88%)	116 (82%)	20 (86%)	52 (81%)
mean $\log_{10}\lambda$	low	1.43 (100%)	1.57 (100%)	1.71 (100%)	4.08 (100%)	n.a
	high	0.53 (74%)	0.65 (70%)	0.81 (71%)	2.75 (100%)	n.a
mean RMSE	low	191.6	177.3	62.7	284.9	288.4
	high	167.9	150.0	54.3	241.8	250.9

The hyperparameter λ was on average smaller for the high SNR than the low SNR. As would be expected, with higher SNR, the model could be more confidently fitted and the constraints had less influence on the solution. For the high SNR, there were 26 to 30% of cases where no noise regularisation was required ($\lambda \to 0$) and the data were treated as noise-free. The main difference between the IBF10, IBF5 and WMN solutions is the relative level of intrinsic smoothing imposed *a priori*, respectively large, small and none. On average the estimated hyperparameter λ was smaller for the IBF5 solution than for the WMN solution and smaller for the IBF10 solution than for the IBF5 solution. With its larger level of smoothing, the IBF10 is more constrained and less sensitive to noise, therefore less noise regularisation was required. The values of λ obtained for the MS solution cannot be directly compared to those of the IBF and WMN solutions because the constraints imposed on the solutions are defined in completely different ways.

The mean RMSE was larger for the low SNR than the high SNR, indicating a more accurate reconstruction with higher SNR. As for the noise-free case, the RMSE was proportional to the level of smoothing imposed on the solution. In the present simulations the values of RMSE were much larger than for the noise-free cases but this was due to the way the RMSE is calculated: on only one time frame for the noise-free simulations, as shown by equation 7.2, and over the entire epoch length in here, as shown by equation 7.3.

7.4.2 Solution with accurate location priors

In this section, the solutions were calculated with accurate priors about the location of active sources, as was done for the noise-free case in section 7.2.2. The IBF10, IBF5 and WMN solutions were assessed for two levels of noise, low and high SNR, and two level of priors, weak and strong priors. The values obtained for LE and $\log_{10}\lambda$ are shown in figure 7.8. The maxLE, and mean RMSE and $\log_{10}\lambda$ for each solution and each condition are summarised in table 7.7.

The inclusion of location priors improved greatly the accuracy of the reconstruction, compare figures 7.7 and 7.8, and tables 7.6 and 7.7. With the strong priors, the LE of the IBF10, IBF5 and WMN solutions was approximately equivalent to the LE observed with the noise-free simulations (compare figure 7.8 with figure 7.5 and table 7.7 with the three first lines of table 7.1). However with weak priors, only the IBF5 solution performed as well as in the noise-free simulations. With weak priors, the LE of the IBF10 solution was reduced compared to the results obtained without priors but remained larger than that of the noise-free case. In the case of the WMN solution, the inclusion of the weak priors did not improve the accuracy of the solution.

The values of the hyperparameter λ were on average similar to (or slightly larger than) those obtained without priors. They followed the same proportions as well: larger values for small level of *a priori* smoothing and/or low SNR and smaller valuse with large amounts of *a priori* smoothing and/or high SNR. The percentage of cases where the data were treated as noise free ($\lambda \to 0$) was reduced by the introduction of priors. This indicates that, even at high SNR, when location priors are included the constraint has a stronger influence on the solution than when no location priors are employed: when location priors are included, a larger part of the data $\mathbf{V}_{\boldsymbol{\varepsilon}}$ can be considered as noise and is not accomodated by the model ($\lambda \neq 0$), thus the solution relies more on the constraints

Low SNR and weak priors

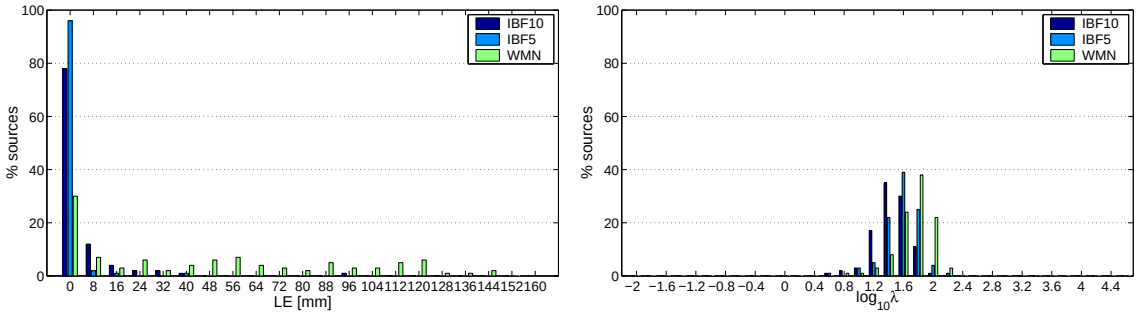

High SNR and weak priors

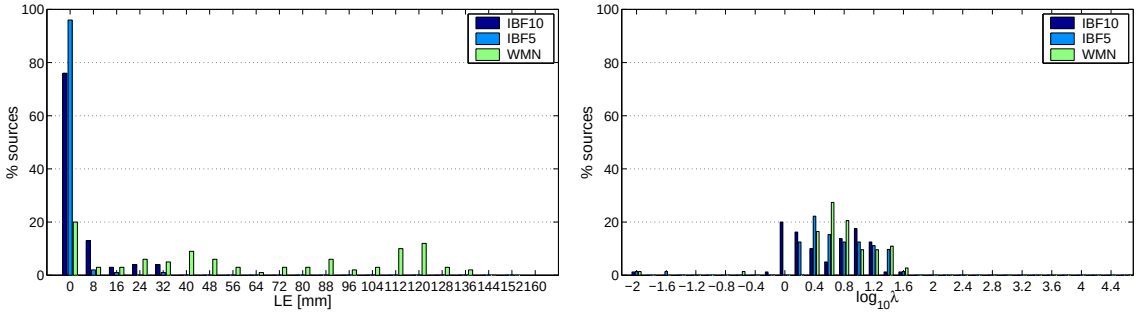

Low SNR and strong priors

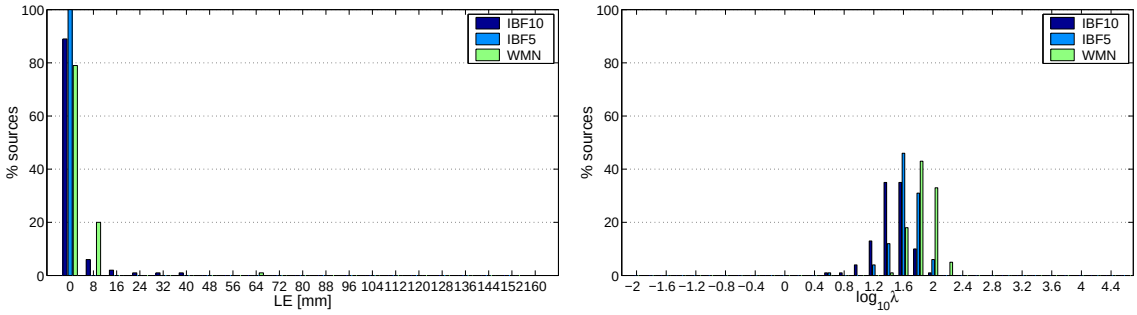

High SNR and strong priors

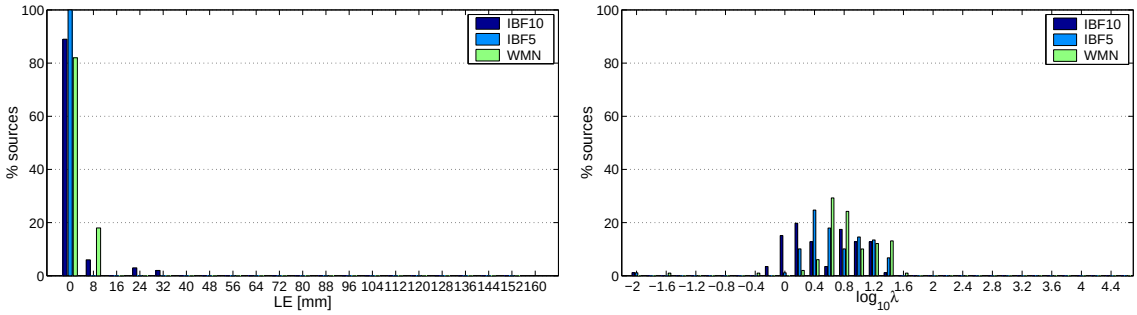

Figure 7.8: LE and $\log_{10}\lambda$ for the three solutions in which location priors can be incorporated (IBF10, IBF5, WMN) for two levels of SNR and two levels of location priors, applied to the simple source simulated data with realistic noise.

Table 7.7: Max LE and mean values of RMSE and $\log_{10}\lambda$. The IBF10, IBF5 and WMN solutions were tested for two levels of SNR (low and high) and two levels of priors (weak and strong). The LE is expressed as the maximum LE to recover at least 80% of the sources within this LE, the actual percentage of sources recovered within this "max LE" is in brackets. The mean of $\log_{10}\lambda$ only takes into account values of λ different from 0, the percentage of cases where $\lambda \neq 0$ is in brackets.

	Priors	SNR	IBF10	IBF5	WMN
max LE [mm]	weak	low	12 (90%)	4 (96%)	100 (82%)
		high	12 (89%)	4 (96%)	116 (83%)
	strong	low	4 (89%)	4(100%)	12(99%)
		high	4 (89%)	4 (100%)	4 (82%)
mean RMSE	weak	low	133.6	85.7	60.1
		high	121.1	75.6	52.8
	strong	low	98.2	39.4	49.3
		high	93.4	37.9	48.9
mean $\log_{10}\lambda$	weak	low	1.44 (100%)	1.59 (100%)	1.73 (100%)
		high	0.54 (80%)	0.66 (72%)	0.76 (73%)
	strong	low	1.46 (100%)	1.64 (100%)	1.84 (100%)
		high	0.52 (86%)	0.69 (89%)	0.82 (99%)

imposed.

With the inclusion of priors, the RMSE was reduced in all cases. Nevertheless, the RMSE remained larger for the data with low SNR than with high SNR. The IBF5 solution with strong location priors and high SNR data provided the most accurate and focal solution.

7.5 Summary of results

With ideal noise-free data and in the absence of prior information about the location of active sources, the IBF solutions had approximately the same localisation ability as the MS solution but the IBF's RMSE was smaller. Because less smoothing is imposed on the IBF solutions than on the MS solution, the former allow solutions with higher spatial frequencies and therefore the reconstructed activity with the IBF solutions was more focal. When two sources were active, the IBF solutions were more likely to recover both sources but with the consequence that the number of spurious sources was much larger for the IBF than the MS solution, especially if little smoothing was imposed. The level of smoothing imposed on the solution is the key factor affecting the regularisation of the source localisation problem. Clearly the IBF approach lies somewhere between the overly smoothed MS solution and the overly focal and insufficiently constrained WMN solution.

When location priors were introduced, the LE was greatly reduced, even with a weak constraint for the IBF solutions, but the WMN solution required a strong constraint to

reach the level of performance shown by IBF solutions. When two sources were considered the number of spurious sources was also greatly reduced, especially with strong priors, rendering the reconstructed activity more easily interpretable. However, the risk of missing one source was increased somewhat, except for the IBF solution with little smoothing and strong priors. Nevertheless only the WMN solution with weak priors would miss more sources than the MS solution. When the priors were included, the IBF solutions provided better reconstructions than the WMN solution, and the MS solution was outperformed in every case by the three other solutions. The combination of smoothing and location priors offers the best regularisation of the source localisation problem but, contrary to the case without priors, less smoothing seems to be required.

The case of mislocated priors does not impinge on the MS solution. With incorrect location priors, the performance of the IBF solution depended on the amount of smoothing imposed. With a large smoothing constraint, the results were similar to the case where no location priors wer employed. By contrast the IBF solution with a small smoothing constraint was more affected by prior mislocation (especially when the prior location was strong). The larger smoothing constraint rendered the solution less sensitive to the bias produced by the mislocated prior. Therefore the constraint of greater smoothing and weak location priors may be preferred when there is risk that the location prior is inaccurate.

When realistic noise is included in the data, the performances of the IBF solutions were slightly diminished compared to the simulations with noise-free data. The noise regularisation was adapted to the SNR of the data, i.e. the hyperparameter λ was proportional to the noise level. Similarly to the noise-free simulations, when no location priors were provided the best localisation (on average) was achieved with a relatively large *a priori* smoothing. Less smoothing was required however if location priors were provided. With noise regularisation the MS solution behaved like the IBF solutions without location priors: its performance was slightly reduced by the noise component and the noise regularisation was adapted to the SNR. On the other hand, if no noise regularisation was applied, the LE of the MS solution was increased dramatically, even for a high SNR. The WMN was also strongly affected by the noise and only capable of some localisation when strong priors were imposed on the solution.

In conclusion, the possibility of controlling and limiting the smoothness imposed on the solution, while being able at the same time to include location priors, ensured that overall the IBF solution outperformed the MS and WMN solutions. When data with realistic noise were used, the ReML algorithm proved to be an efficient way to estimate the hyperparameter λ as this ensured that the noise regularisation adapted automatically to the level of noise in the data.

Chapter 8

Discussion and conclusion

The only way to overcome the intrinsic limitations (on temporal or spatial resolution) of individual brain imaging techniques is to combine data obtained from different techniques within the same mathematical framework. Such a combination should provide an optimal solution that harnesses the strengths of each individual technique.

In general, the advantages of a distributed linear approach to the source localisation problem, as presented in section 5.1, are the following: A non-iterative linear solution is readily available and calculable, as presented in section 5.4. Unlike ECD-oriented approaches, no assumptions are made about the number of active sources, and those sources can be relatively diffusely distributed. In the framework of a distributed linear solution, structural information extracted from MR images, such as source orientation and correlation, can be combined with the EEG data. It is also possible to include other sources of data, such as activation maps from functional MRI (or PET) studies, to refine the localisation without impairing the fine temporal resolution of EEG data.

Structural information is usually obtained by reconstructing the cortical surface from an MR image. This is a non-trivial and difficult process (Dale & Sereno, 1993; van Essen & Drury, 1997; Dale *et al.*, 1999; Fischl *et al.*, 1999; Fischl & Dale, 2000; Goebel & Max Planck Society, 2000) but, in the present work, the explicit reconstruction of the cortical surface is avoided by using a user-independent method to extract anatomical information from MR images. The sources are not constrained to lie on a folded surface but are spread on a fully three-dimensioinal grid. The orientation of each dipole is directly incorporated in the lead field matrix. Each oriented dipole can thus be viewed as a voxel in a three-dimensional volume, the amplitude of a dipole representing the activity in that voxel.

The approach adopted in this work does not strictly follow the scheme of a distributed linear reconstruction. The spatial IBF obtained from the anatomical information allows a two-step approach to imposing constraints on the source localisation problem. Firstly the size of the problem is reduced by projecting the solution space onto the sub-space spanned by the spatial IBF. Secondly the anatomically constrained problem is solved. In the present case, a linear solution was chosen because of its desirable properties and ease of use, but other methods could be employed to estimate the best combination of spatial basis functions.

The extraction of spatial IBFs is the key element in the approach presented here. Although systematic, it has the disadvantage of being time-consuming and computationally demanding. Fortunately, the spatial IBFs need only be calculated once for a specific head and source model. Afterwards, various hypotheses about prior location of activation and different data sets can be studied with the same spatial IBF set but different "soft" constraints. The introduction of the spatial IBF offers a clear separation between the "hard" constraints relying on anatomy and other more intuitive "soft" constraints.

In the absence of prior location information, the MS solution provides source reconstruction with an accuracy similar to that of the IBF solution. But as its name suggests, the reconstructed sources obtained with the MS solution are generally too smooth. With the MS solution it is not possible to make full use of anatomical information either : the sources are constrained to the grey matter but their orientation is left free and the smoothness constraint, a simple three-dimensional Laplacian, does not respect cerebral anatomy. Moreover, no functional information about the (possible) location of the activity within grey matter can be introduced.

The WMN solution as employed here uses only part of the structural information to constrain the solution : the orientations of the sources are fixed but no spatial correlation among them is imposed. In contrast to the MS solution, the WMN was inefficient without location priors but was capable of accurate localisation with strong location priors. The solution presented and tested by Liu *et al.* (1998), here termed "Surface WMN" (SWMN) solution, is equivalent to the WMN solution employed here. The difference between the two solutions lies in the source model : the sources are spread on the extracted cortical surface in Liu *et al.* (1998) instead of a three-dimensional grid as in the WMN employed in this work. In both WMN and SWMN solutions, no spatial correlation between the sources is assumed and *a priori* information about the location of the sources, obtained from (simulated) fMRI activation maps, was introduced to better constrain the problem. The SWMN solution was tested by Liu *et al.* (1998) for four values of the relative weighting of the prior location (fMRI activation) : 0%, 90%, 99% and 100% which corresponds, in equation 6.6, to values of β equal to : 0, 2.16, 9 and ∞. In my simulations, three levels were used ($\beta = 0$, 1 or 4), corresponding to relative weightings of 0%, 75% and 96%. By setting $\beta \to \infty$, one assumes an infinitely strong confidence in the location priors, effectively precluding any activity outside those priors. The conclusion of Liu *et al.* (1998) to use a compromise value of 90%, i.e. $\beta = 2.16$, for the weighting of the *a priori* source location is supported by the simulations in the present work. Interestingly, the introduction of some smoothness in the IBF solution means that a smaller bias or weighting towards the *a priori* location can be employed, as good localisation results are already obtained with the IBF solutions and $\beta = 1$, equivalent to a relative weighting of 75%.

The solutions used here were tested with two simultaneously active sources in an extreme case where both sources are perfectly synchronised in time and have exactly the same strength in the source space, but **not** in the measurement space. In those particular conditions and without location priors, the two sources were recovered efficiently (the WMN solution is not considered here) in less than 50% of the cases. Moreover there were always a few spurious reconstructed sources (according to the amplitude thresholding adopted). Contrary to what might have been expected, the introduction of location priors did not help in recovering the two sources in more cases. Nevertheless, the location priors improved the solution by greatly reducing the number of spurious sources. If the signals produced by two sources are almost collinear in the measurement space, or if the

amplitude of the signal generated by one source is larger than that generated by the other one, then one source will be "hidden" or "shadowed" by the other. Location priors cannot make the sources more visible but will help locating more sharply the sources.

The solutions employed here were also tested with data, generated by a single active source, contaminated by realistic noise and background brain activity. The ReML procedure was successfully applied to control the noise regularisation by systematically estimating the hyperparameter λ in equation 5.18 or 5.19. With noise regularisation, the IBF, MS and WMN solutions behaved almost as they did with ideal noise-free data. If no noise regularisation was applied, i.e. $\lambda \to 0$, the MS solution was strongly affected by the noise and was unable to provide any proper localisation, even for a high SNR. The maximum smoothing constraint alone is thus not enough to control the effect of the noise contained in the data. Even at constant SNR and for the same levels of location priors, the values of λ vary on a large scale, hence the use of a logarithmic scale to present the results. As the noise component $\boldsymbol{\mathcal{E}}$ was the same for all the simulations, the value of λ depends on the source configuration and the distribution of potential it generates over the scalp, therefore any *a priori* fixed value of λ can lead to sub-optimal solutions. An advantage of using the spatial and temporal IBF is that the iterative ReML algorithm is more tractable. Indeed, at each iteration a problem of size $N_{k_s} \times N_{k_t}$ is solved instead of $N_j \times N_t$, where $N_{k_s} \ll N_j$ and $N_{k_t} \ll N_t$, which requires much less memory and computational time.

The solutions presented here were not compared to ECD approaches. Apart for the moving ECD solution, where the iterative fitting procedure has to simultaneously optimise the location, orientation and amplitude of the ECDs, the fixed-ECD solutions are particular cases of the more general linear distributed solution. ECD-based attempts at localisation have used fMRI (or PET) activation maps as prior constraints on the inverse problem: a single ECD is placed (or "seeded") at the centre of gravity of fMRI (or PET) regions of activation, or at any location that seems useful, and then the orientation and amplitude of the ECDs are fitted to the EEG data, e.g. in Opitz *et al.* (1999). In the linear solution framework, the seeded ECD solution can be obtained by setting the fMRI weighting, parameter β in equation 6.6, to infinity or equivalently by setting the *a priori* variance of the sources outside the fMRI activations to 0.

The effect of errors in the solution of the forward problem on the accuracy of the reconstruction of the sources was not assessed here. There is no way to completely characterise this effect in a realistic head model as the synthetic data are generated with the same model (or lead field) used to solve the inverse problem.

In conclusion I have demonstrated that the combination of EEG-MRI-fMRI data in the same mathematical framework, controlled by a set of hyperparameters, results in more accurate and reliable solutions than two commonly used source localisation approaches. Ultimately the IBF solution proposed here will need to be applied and validated on real data sets. This will be the subject of future work.

Part III

Appendices

Appendix A

Green's theorem

A.1 Calculation of $\psi = 1/r$, $\vec{\nabla}\psi$ and $\nabla^2\psi$

If ψ is defined as the inverse of the distance r between the origin of space $\vec{o}$ and any point $\vec{r} = [x\ y\ z]^t$, then $\psi = 1/r = (x^2 + y^2 + z^2)^{-1/2}$ and

$$\vec{\nabla}\psi = -\frac{\vec{r}}{r^3} = -\frac{\vec{n}}{r^2} \tag{A.1a}$$

$$\nabla^2\psi = 0 \tag{A.1b}$$

where $\vec{n}$ is a unit vector oriented in the same direction as $\vec{r}$

This is easily shown by calculating

$$\vec{\nabla}\psi = \frac{\delta\psi}{\delta x}\,\vec{e}_x + \frac{\delta\psi}{\delta y}\,\vec{e}_y + \frac{\delta\psi}{\delta z}\,\vec{e}_z \tag{A.2}$$

where

$$\frac{\delta}{\delta x}\left(\frac{1}{r}\right) = -x(x^2 + y^2 + z^2)^{-3/2} \tag{A.3a}$$

$$\frac{\delta}{\delta y}\left(\frac{1}{r}\right) = -y(x^2 + y^2 + z^2)^{-3/2} \tag{A.3b}$$

$$\frac{\delta}{\delta z}\left(\frac{1}{r}\right) = -z(x^2 + y^2 + z^2)^{-3/2} \tag{A.3c}$$

so

$$\vec{\nabla}\psi = -\frac{x\,\vec{e}_x + y\,\vec{e}_y + z\,\vec{e}_z}{(x^2 + y^2 + z^2)^{3/2}} \tag{A.4}$$

Then

$$\nabla^2\psi = \vec{\nabla}(\vec{\nabla}\psi) = \frac{\delta^2\psi}{\delta x^2} + \frac{\delta^2\psi}{\delta y^2} + \frac{\delta^2\psi}{\delta z^2} \tag{A.5}$$

where

$$\frac{\delta^2\psi}{\delta x^2} = \frac{\delta}{\delta x}\left(-\frac{x}{(x^2 + y^2 + z^2)^{3/2}}\right) = \frac{2x^2 - y^2 - z^2}{(x^2 + y^2 + z^2)^{5/2}} \tag{A.6a}$$

$$\frac{\delta^2\psi}{\delta y^2} = \frac{-x^2+2y^2-z^2}{(x^2+y^2+z^2)^{5/2}} \tag{A.6b}$$

$$\frac{\delta^2\psi}{\delta z^2} = \frac{-x^2-y^2+2z^2}{(x^2+y^2+z^2)^{5/2}} \tag{A.6c}$$

therefore

$$\nabla^2\psi = 0 \tag{A.7}$$

A.2 Singularity point in Green's theorem

Green's theorem stated in 2.10 says:

$$\sum_l \int_{S_l} \left[\sigma^-(\psi^-\vec{\nabla}\phi^- - \phi^-\vec{\nabla}\psi^-) - \sigma^+(\psi^+\vec{\nabla}\phi^+ - \phi^+\vec{\nabla}\psi^+)\right] d\vec{S}_l = \sum_k \int_{v_k} \left[\psi\vec{\nabla}.\sigma\vec{\nabla}\phi - \phi\vec{\nabla}.\sigma\vec{\nabla}\psi\right] dv_k \tag{A.8}$$

and ψ is defined by $\psi = 1/r$ where r is the distance between the origin $\vec{o}$, an arbitrary point not on a surface, and any point on the surface S_l or in the volume v_k. One volume integral, say over v_m, is singular for $r = 0$, so a small homogeneous spherical volume v_ϵ of radius ϵ and surface S_ϵ around the origin $\vec{o}$ has to be excluded[1] from the volume integrals (and the corresponding surface S_ϵ added to the surface integrals).

For an homogeneous volume (like v_ϵ), and ψ and ϕ two well behaved functions, Green's theorem simplifies to:

$$\int_v \left[\psi\vec{\nabla}(\sigma\vec{\nabla}\phi) - \phi\vec{\nabla}(\sigma\vec{\nabla}\psi)\right] dv = \int_S \left[\psi\sigma\vec{\nabla}\phi - \phi\sigma\vec{\nabla}\psi\right] d\vec{S} \tag{A.9}$$

So by excluding v_ϵ from the volume v_m, adding S_ϵ to the surface integrals, and taking $\psi = 1/r$, equation A.8 becomes:

$$\begin{aligned}
&\sum_l \int_{S_l} \left[\sigma^- \left(\frac{1}{r}\vec{\nabla}\phi^- - \phi^-\vec{\nabla}\left(\frac{1}{r}\right)\right) - \sigma^+\left(\frac{1}{r}\vec{\nabla}\phi^+ - \phi^+\vec{\nabla}\left(\frac{1}{r}\right)\right)\right] d\vec{S}_l \\
&\qquad + \int_{S_\epsilon} \sigma\left(\frac{1}{\epsilon}\vec{\nabla}\phi - \phi\vec{\nabla}\left(\frac{1}{\epsilon}\right)\right) d\vec{S}_\epsilon \\
&= \sum_{k\neq m} \int_{v_k} \left[\frac{1}{r}\vec{\nabla}(\sigma\vec{\nabla}\phi) - \phi\vec{\nabla}\left(\sigma\vec{\nabla}\left(\frac{1}{r}\right)\right)\right] dv_k \\
&\qquad + \int_{v_m - v_\epsilon} \left[\frac{1}{r}\vec{\nabla}(\sigma\vec{\nabla}\phi) - \phi\vec{\nabla}\left(\sigma\vec{\nabla}\left(\frac{1}{r}\right)\right)\right] dv_m \qquad \text{(A.10a)} \\
&= \sum_{k\neq m} \int_{v_k} \left[\frac{1}{r}\vec{\nabla}(\sigma\vec{\nabla}\phi) - \phi\sigma\nabla^2\left(\frac{1}{r}\right)\right] dv_k \\
&\qquad + \int_{v_m - v_\epsilon} \left[\frac{1}{r}\vec{\nabla}(\sigma\vec{\nabla}\phi) - \phi\sigma\nabla^2\left(\frac{1}{r}\right)\right] dv_m \qquad \text{(A.10b)} \\
&= \sum_{k\neq m} \int_{v_k} \frac{1}{r}\vec{\nabla}(\sigma\vec{\nabla}\phi)\, dv_k \\
&\qquad + \int_{v_m - v_\epsilon} \frac{1}{r}\vec{\nabla}(\sigma\vec{\nabla}\phi)\, dv_m \qquad \text{(A.10c)}
\end{aligned}$$

[1] This is possible because $\vec{o}$ is not on any surface and ϵ is sufficiently small.

The integral over S_ϵ can be calculated explicitly for we know that $r = \epsilon$ and $\vec{\nabla}(1/r) = -\vec{n}/r^2$, where $\vec{n}$ is oriented from **inside** the sphere S_ϵ toward **outside** S_ϵ. From the sign convention used up to now for the surface integral, we have $d\vec{S}_\epsilon = -\vec{n}dS_\epsilon$: $d\vec{S}_\epsilon$ is by definition oriented from inside the volume $v_m - v_\epsilon$ towards outside, i.e. from **outside** S_ϵ towards **inside** S_ϵ relative to $\vec{o}$, so $d\vec{S}_\epsilon$ is oriented along $-\vec{n}$.

In spherical coordinate, the surface integral over $d\vec{S}_\epsilon$ is expressed by :

$$\int_{S_\epsilon} \sigma \left(\frac{1}{\epsilon}\vec{\nabla}\phi - \phi\vec{\nabla}\left(\frac{1}{\epsilon}\right)\right) d\vec{S}_\epsilon = -\int_0^\pi \sigma \left(\frac{1}{\epsilon}(\vec{n}\vec{\nabla}\phi) + \phi\frac{1}{\epsilon^2}\right) 2\pi\epsilon^2 \sin\alpha\, d\alpha \quad \text{(A.11a)}$$

$$= -2\pi \int_0^\pi \sigma \left(\epsilon(\vec{n}\vec{\nabla}\phi) - \phi\right) \sin\alpha\, d\alpha \quad \text{(A.11b)}$$

and if ϵ tends to 0 then,

$$\lim_{\epsilon\to 0} \int_{S_\epsilon} \sigma \left(\frac{1}{\epsilon}\vec{\nabla}\phi - \phi\vec{\nabla}\left(\frac{1}{\epsilon}\right)\right) d\vec{S}_\epsilon = -2\pi\sigma\phi \int_0^\pi \sin\alpha\, d\alpha \quad \text{(A.12a)}$$

$$= -4\pi\sigma\phi \quad \text{(A.12b)}$$

where σ and ϕ are evaluated at the origin ($\vec{r} = \vec{o}$).

With $\epsilon \to 0$, v_ϵ vanishes and equation A.10 becomes :

$$\sum_l \int_{S_l} \left[(\sigma^-\vec{\nabla}\phi^- - \sigma^+\vec{\nabla}\phi^+)\frac{1}{r} - (\sigma^-\phi^- - \sigma^+\phi^+)\vec{\nabla}\left(\frac{1}{r}\right)\right] d\vec{S}_l$$

$$= 4\pi\sigma\phi + \sum_k \int_{v_k} \frac{1}{r}\vec{\nabla}(\sigma\vec{\nabla}\phi)\, dv_k \quad \text{(A.13)}$$

which is similar to equation 2.11.

Appendix B

Analytical solution of Maxwell's equations in a three sphere shell model

The analytical solution of the simplified Maxwell's equation 2.7 is possible for particular volume model. One such model, commonly used in the field of EEG source localisation, is the three sphere shell model described in section 4.1 and figure 4.1. It consists of three concentric spheres of radius r_1, r_2 and r_3, with $r_1 < r_2 < r_3$: The innermost spherical volume represents the brain volume. The volume comprised between the spheres of radius r_1 and r_2 models the skull layer. The outer layer volume, between radii r_2 and r_3, corresponds to the scalp layer.

Let's assume that the brain and scalp volumes have the same conductivity σ, and that the skull volume has a conductivity σ_{sk}. A current source dipole $\vec{m}$, located at a height z on the axis $\vec{e}_z$, generates a potential distribution $V(\vec{s})$ on the surface of the outer sphere. In spherical coordinates, i.e. $\vec{s} = \vec{s}(\theta, \varphi)$ as shown in figure B.1, this potential is calculated by the following formula from Ary *et al.* (1981) :

$$\begin{aligned} V(\vec{s}) &= V(\theta, \varphi) \\ &= \frac{1}{4\pi\sigma R^2} \sum_{n=1}^{\infty} \frac{2n+1}{n} b^{n-1} \left[\frac{\xi(2n+1)^2}{d_n(n+1)} \right] \\ &\qquad \Big[n\, m_z P_n(\cos\theta) + (m_x \cos\varphi + m_y \sin\varphi) P_n^1(\cos\theta) \Big] \end{aligned} \tag{B.1}$$

where

- $b = z/r_3$ is the eccentricity of the dipole,
- m_x, m_y and m_z are the components of the dipole $\vec{m} = [m_x\, m_y\, m_z]^t$ along the main axes,
- $\xi = \sigma_{sk}/\sigma$ is the relative conductivity of the skull volume to the conductivity of the brain and scalp volumes,

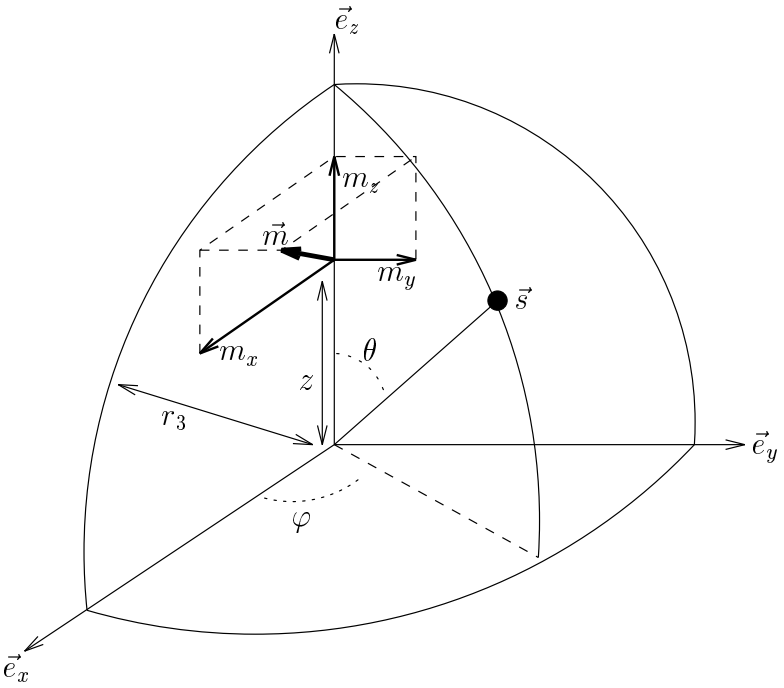

Figure B.1: Current source dipole in a three sphere shell model: The dipole $\vec{m} = [m_x\, m_y\, m_z]^t$, located at a height z on the axe $\vec{e}_z$,generates a potential distribution $V(\vec{s})$, with $\vec{s} = \vec{s}(\theta, \varphi)$, on the surface of the outer sphere.

- $P_n(\cos\theta)$ and $P_n^1(\cos\theta)$ are Legendre and associated Legendre polynomials,
- d_n is defined by:

$$\begin{aligned} d_n &= [(n+1)\xi + n]\left[\frac{n\xi}{n+1} + 1\right] \\ &\quad +(1-\xi)[(n+1)\xi + n](f_1^{2n+1} - f_2^{2n+1}) - n(1-\xi)^2\left(\frac{f_1}{f_2}\right)^{2n+1} \end{aligned} \tag{B.2}$$

with $f_1 = r_1/r_3$ and $f_2 = r_2/r_3$.

Even though the potential $V(\vec{s})$ is expressed as an infinite sum of terms, it is only necessary to calculate a few tens of them, as for n increasing the corresponding terms rapidly converge to zero. There also exists a closed-form approximation that requires less computational effort (at the cost of some minor error) as shown by Sun (1997) but this approximate solution was not used here.

The analytical expression of the potential for more complicated layouts can be found in the literature: four spheres with different conductivity (Arthur & Geselowitz, 1970; Cuffin & Cohen, 1979), cylindrical volume (Lambin & Troquet, 1983; Kleinermann *et al.*, 2000) or cubic volume (Ferguson & Stroink, 1994).

Appendix C

Tikhonov regularisation and Moore-Penrose pseudo-inverse

There exists a direct relationship between the Tikhonov regularisation and the Moore-Penrose (MP) pseudo-inverse, the MP pseudo-inverse is infact a particular case of the Tikhonov regularisation. From the relation 5.17, the problem to solve is :

$$\mathbf{v} + \boldsymbol{\varepsilon} = \mathbf{L}_{\mathbf{B}_s}\, \mathbf{k}_s \tag{C.1}$$

The Moore-Penrose pseudo-inverse $\mathbf{L}^{+}_{\mathbf{B}_s}$ of the matrix $\mathbf{L}_{\mathbf{B}_s}$ is obtained through its singular value decomposition (SVD) :

$$\mathbf{L}_{\mathbf{B}_s} = \mathbf{U}\,\mathbf{S}\,\mathbf{W}^t \Rightarrow \mathbf{L}^{+}_{\mathbf{B}_s} = \mathbf{W}\,\mathbf{S}^{+}\,\mathbf{U}^t \tag{C.2}$$

where $\mathbf{U}^t\mathbf{U} = \mathbf{I}_{N_e}$, $\mathbf{W}^t\mathbf{W} = \mathbf{I}_{N_{k_s}}$ and the singular values s_i of the diagonal matrix $\mathbf{S}$ are "filtered" into s_i^{+} to create $\mathbf{S}^{+}$. The filter applied on the singular values s_i can be expressed by the following function $F(s_i)$:

$$s_i^{+} = F(s_i) = \begin{cases} 1/s_i & \text{if } s_i \neq 0 \\ 0 & \text{if } s_i = 0 \end{cases} \tag{C.3}$$

So, if $\mathbf{u}_i$ and $\mathbf{w}_i$ represent the i^{th} column of $\mathbf{U}$ and $\mathbf{V}$ respectively, solving the problem C.1 with the MP pseudo-inverse is equivalent to

$$\hat{\mathbf{k}}_s = \mathbf{L}^{+}_{\mathbf{B}_s}\mathbf{v}_{\boldsymbol{\varepsilon}} = \sum_{i=1}^{N} \frac{(\mathbf{u}_i^t\,\mathbf{v}_{\boldsymbol{\varepsilon}})}{s_i}\,\mathbf{w}_i \tag{C.4}$$

Problems arise when some singular values are very small : these singular values (and respective left and right singular vectors) have a strong influence on the solution of C.1 because their inverse is very large and may amplify noise or error components in C.4.

The "Truncated SVD" is a possible solution : only the singular values above some threshold ζ are considered. The filter applied on the singular values s_i is then expressed by the following function $F_\zeta(s_i)$:

$$s_i^{+} = F_\zeta(s_i) = \begin{cases} 1/s_i & \text{if } s_i > \zeta \\ 0 & \text{otherwise} \end{cases} \tag{C.5}$$

The truncation of the series of singular values ensures the rejection of the smallest singular values, but this rejection is rather abrupt and this may not be the best solution if the spectrum of singular values is decreasing smoothly.

If we consider the weighted minimum norm problem 5.19 with $\mathbf{C}_{\boldsymbol{\varepsilon}} = \mathbf{I}_{N_e}$ and $\mathbf{H}_{\mathbf{B}_s} = \mathbf{I}_{N_{k_s}}$,

$$\hat{\mathbf{k}}_s = \arg \min_{\mathbf{k}_s} \left\{ \|\mathbf{L}_{\mathbf{B}_s}\, \mathbf{k}_s - \mathbf{v}_{\boldsymbol{\varepsilon}}\|^2 + \lambda^2 \|\mathbf{k}_s\|^2 \right\} \tag{C.6}$$

the "zero order"[1] Tikhonov regularised solution can also been expressed from the singular value decomposition of $\mathbf{L}_{\mathbf{B}_s}$ (Varah, 1979). The filter $F(s_i)$ applied to the singular values s_i depends on the hyperparameter λ:

$$s_i^+ = F_\lambda(s_i) = \left(\frac{1}{1 + \lambda^2/s_i^2} \right) \frac{1}{s_i} = \frac{s_i}{s_i^2 + \lambda^2} \tag{C.7}$$

Therefore the solution of C.6 has the form:

$$\hat{\mathbf{k}}_s = \sum_{i=1}^{N_e} \left(\frac{1}{1 + \lambda^2/s_i^2} \right) \frac{(\mathbf{u}_i^t\, \mathbf{v}_{\boldsymbol{\varepsilon}})}{s_i} \mathbf{w}_i = \sum_{i=1}^{n} \frac{s_i}{s_i^2 + \lambda^2} \left(\mathbf{u}_i^t\, \mathbf{v}_{\boldsymbol{\varepsilon}}\right) \mathbf{w}_i \tag{C.8}$$

The filtering $F_\lambda(s_i)$ of the singular values in the Tikhonov regularisation ensures that

- for large s_i compared to λ, Tikhonov solution is similar to the pseudo-inverse,
- for small s_i compared to λ the solution is regularised: the singular value s_i and its associated singular vectors $\mathbf{u}_i$ and $\mathbf{v}_i$ do not influence the solution $\mathbf{k}_s$.

The value of λ fixes the level at which the influence of the smaller singular values is reduced, and this is achieved **smoothly** over the spectrum of singular values.

A similar relation can be obtained for the general case where $\mathbf{C}_{\boldsymbol{\varepsilon}} \neq \mathbf{I}_{N_e}$ and $\mathbf{H}_{\mathbf{B}_s} \neq \mathbf{I}_{N_{k_s}}$ by the generalised singular value decomposition (GSVD) of the pair of matrices $(\mathbf{C}_{\boldsymbol{\varepsilon}}^{-1/2}\mathbf{L}_{\mathbf{B}_s}, \mathbf{H}_{\mathbf{B}_s})$, as shown in (Varah, 1979).

[1] "zero order" because $\mathbf{H}_{\mathbf{B}_s} = \mathbf{I}_{N_{k_s}}$ is a "zero" order derivative operator and the norm of the solution $\|\mathbf{k}_s\|^2$ is minimised. A "first order" (resp. "second order") Tikhonov regularisation minimises the norm of the first (resp. second) derivative of the solution by defining $\mathbf{H}_{\mathbf{B}_s}$ as a first (resp. second) derivative operator.

Appendix D

Non-instantaneous problem and ReML solution

The non-instantaneous problem 5.28 ($\mathbf{V}_{\mathbf{B}_t} + \boldsymbol{\mathcal{E}}_{\mathbf{B}_t} = \mathbf{L}_{\mathbf{B}_s}\,\mathbf{K}_{st}$) has the same form as equation 5.43 :

$$\mathbf{B} = \mathbf{A}\mathbf{X} + \mathbf{R} \quad \Leftrightarrow \quad \begin{bmatrix} \mathbf{B}_1 \\ \mathbf{B}_2 \end{bmatrix} = \begin{bmatrix} \mathbf{A}_1 \\ \mathbf{A}_2 \end{bmatrix} \mathbf{X} + \begin{bmatrix} \mathbf{R}_1 \\ \mathbf{R}_2 \end{bmatrix} \tag{D.1}$$

where $\mathrm{Var}(\mathbf{R}) = \mathbf{C}(\theta_1, \theta_2) = \begin{bmatrix} \theta_1^2\mathbf{I}_{m_1} & 0 \\ 0 & \theta_2^2\mathbf{I}_{m_2} \end{bmatrix}$.
This equation can be rewritten like equation 5.30 (or 5.20, with $\lambda = \theta_1/\theta_2$) :

$$\mathbf{b}^* = \mathbf{A}^*\mathbf{x}^* + \mathbf{r}^* \quad \Leftrightarrow \quad \begin{bmatrix} \mathbf{b}_{1,1} \\ \vdots \\ \mathbf{b}_{1,q} \\ \mathbf{b}_{2,1} \\ \vdots \\ \mathbf{b}_{2,q} \end{bmatrix} = \begin{bmatrix} \mathbf{A}_1 & 0 & 0 \\ 0 & \ddots & 0 \\ 0 & 0 & \mathbf{A}_1 \\ \mathbf{A}_2 & 0 & 0 \\ 0 & \ddots & 0 \\ 0 & 0 & \mathbf{A}_2 \end{bmatrix} \begin{bmatrix} \mathbf{x}_1 \\ \vdots \\ \mathbf{x}_q \end{bmatrix} + \begin{bmatrix} \mathbf{r}_{1,1} \\ \vdots \\ \mathbf{r}_{1,q} \\ \mathbf{r}_{2,1} \\ \vdots \\ \mathbf{r}_{2,q} \end{bmatrix} \tag{D.2}$$

where $\mathbf{A}^*$ is a $qm \times qn$ matrix, $\mathbf{x}^*$ is a $qn \times 1$ vector, $\mathbf{b}^*$ and $\mathbf{r}^*$ are $qm \times 1$ vectors, and with $\mathbf{x}_i$, the i^{th} column of $\mathbf{X}$, $\mathbf{b}_{1,i}$ (resp. $\mathbf{r}_{1,i}$) the m_1 first rows of the i^{th} column of $\mathbf{B}$ (resp. $\mathbf{R}$) and $\mathbf{b}_{2,i}$ (resp. $\mathbf{r}_{2,i}$) the m_2 last rows of the i^{th} column of $\mathbf{B}$ (resp. $\mathbf{R}$). The covariance matrix $\mathbf{C}^*$ of $\mathbf{r}^*$ is still linearly parameterised by θ_1 and θ_2 :

$$\mathbf{C}^* = \begin{bmatrix} \theta_1^2\mathbf{I}_{qm_1} & 0 \\ 0 & \theta_2^2\mathbf{I}_{qm_2} \end{bmatrix} = \begin{bmatrix} \theta_1^2\mathbf{I}_{m_1} & 0 & 0 & & & \\ 0 & \ddots & 0 & & 0 & \\ 0 & 0 & \theta_1^2\mathbf{I}_{m_1} & & & \\ & & & \theta_2^2\mathbf{I}_{m_2} & 0 & 0 \\ & 0 & & 0 & \ddots & 0 \\ & & & 0 & 0 & \theta_2^2\mathbf{I}_{m_2} \end{bmatrix} \tag{D.3}$$

Solving directly equation D.2 and updating the hyperparameters is unpractical for large q. By considering $\mathbf{E}^* = \mathbf{A}^{*t}\mathbf{C}^{*-1}\mathbf{A}^*$:

$$\mathbf{E}^* = \begin{bmatrix} \theta_1^{-2}\mathbf{A}_1^t\mathbf{A}_1 + \theta_2^{-2}\mathbf{A}_2^t\mathbf{A}_2 & 0 & 0 \\ 0 & \ddots & 0 \\ 0 & 0 & \theta_1^{-2}\mathbf{A}_1^t\mathbf{A}_1 + \theta_2^{-2}\mathbf{A}_2^t\mathbf{A}_2 \end{bmatrix} = \begin{bmatrix} \mathbf{E} & 0 & 0 \\ 0 & \ddots & 0 \\ 0 & 0 & \mathbf{E} \end{bmatrix} \tag{D.4}$$

such that

$$\hat{\mathbf{x}}^* = \mathbf{E}^{*-1}\mathbf{A}^*\mathbf{C}^{*-1}\mathbf{b}^* = \mathbf{E}^{*-1} \begin{bmatrix} \theta_1^{-2}\mathbf{A}_1^t\mathbf{b}_{1,1} + \theta_2^{-2}\mathbf{A}_2^t\mathbf{b}_{2,1} \\ \vdots \\ \theta_1^{-2}\mathbf{A}_1^t\mathbf{b}_{1,q} + \theta_2^{-2}\mathbf{A}_2^t\mathbf{b}_{2,q} \end{bmatrix} \tag{D.5}$$

and each $\mathbf{x}_i$ is, of course, computed as in 5.39 (or 5.23).

In order to update the hyperparameters, the residuals $\mathbf{r}^* = \mathbf{b}^* - \mathbf{A}^*\hat{\mathbf{x}}^*$ and the loss of degrees of freedom have to be estimated. Similarly to equation 5.41, p_1^* and p_2^* are estimated by

$$p_1^* = \text{trace}\left(\theta_1^{-2}\mathbf{E}^{*-1}\mathbf{A}_1^{*t}\mathbf{A}_1^*\right) = q\ \text{trace}\left(\theta_1^{-2}\mathbf{E}^{-1}\mathbf{A}_1^t\mathbf{A}_1\right) = q\,p_1 \tag{D.6a}$$

$$p_2^* = \text{trace}\left(\theta_2^{-2}\mathbf{E}^{*-1}\mathbf{A}_2^{*t}\mathbf{A}_2^*\right) = q\ \text{trace}\left(\theta_2^{-2}\mathbf{E}^{-1}\mathbf{A}_2^t\mathbf{A}_2\right) = q\,p_2 = q\,(n - p1) \tag{D.6b}$$

where p_1 and p_2 are calculated like in 5.41.

Therefore the updated values of $\boldsymbol{\theta}$ should be

$$\hat{\theta}_1^2 = \frac{\mathbf{r}_1^{*t}\mathbf{r}_1^*}{q\,m_1 - p_1^*} = \frac{\sum_{i=1}^{q}\mathbf{r}_{1,i}^t\mathbf{r}_{1,i}}{q\,(m_1 - p_1)} \tag{D.7a}$$

$$\hat{\theta}_2^2 = \frac{\mathbf{r}_2^{*t}\mathbf{r}_2^*}{q\,m_2 - p_2^*} = \frac{\sum_{i=1}^{q}\mathbf{r}_{2,i}^t\mathbf{r}_{2,i}}{q\,(m_2 - p_2)} \tag{D.7b}$$

which is similar to 5.42.

Bibliography

Aine, C., Huang, M., Stephen, J., & Christner, R. 2000. Multistart Algorithms for MEG Empirical Data Analysis Reliably Characterize Locations and Time Courses of Multiple Sources. *NeuroImage*, **12**(2), 159–172.

Arthur, R. Martin, & Geselowitz, David B. 1970. Effect of Inhomogeneities on the Apparent Location and Magnitude of a Cardiac Current Dipole Source. *IEEE Transactions on Biomedical Engineering*, **17**(2), 141–146.

Ary, James P., Klein, Stanley A., & Fender, Derek H. 1981. Location of Sources of Evoked Scalp Potentials: Corrections for Skull and Scalp Thickness. *IEEE Transactions on Biomedical Engineering*, **28**(6), 447–452.

Ashburner, John, & Friston, Karl J. 1997. Multimodal Image Coregistration and Partitioning — A Unified Framework. *NeuroImage*, **6**, 209–217.

Ashburner, John, & Friston, Karl J. 1999. Nonlinear Spatial Normalization using Basis Functions. *Human Brain Mapping*, **7**(4), 254–266.

Ashburner, John T. 2000 (July). *Computational Neuroanatomy.* Ph.D. thesis, The Wellcome Department of Cognitive Neurology, Institute of Neurology, University College London, London, UK.

Awada, Kassem A., Jackson, David R., Williams, Jeffery T., Wilton, Donald R., Baumann, Stephen B., & Papanicolaou, Andrew C. 1997. Computational Aspects of Finite Element Modeling in EEG Source Localization. *IEEE Transactions on Biomedical Engineering*, **44**(8), 736–752.

Backus, G.E., & Gilbert, J.F. 1970. Uniqueness in the Inversion of Inacurate Gross Earth Data. *Philosophical Transactions of the Royal Society*, **266**, 123–192.

Baillet, Sylvain. 1998 (July). *Toward Functional Brain Imaging of Cortical Electrophysiology. Markovian Models for Magneto and Electroencephalogram Source Estimation and Experimental Assessments.* Ph.D. thesis, University of Paris XI, Orsay, France.

Baillet, Sylvain, & Garnero, Line. 1997. A Bayesian Approach to Introducing Anatomo-functional Priors in the EEG/MEG Inverse Problem. *IEEE Transactions on Biomedical Engineering*, **44**(5), 374–385.

Baillet, Sylvain, Garnero, Line, Marin, Gildas, & Hugonin, Jean-Paul. 1999. Combined MEG and EEG Source Imaging by Minimization of Mutual Information. *IEEE Transactions on Biomedical Engineering*, **46**(5), 522–534.

Becker, A.A. 1992. *The Boundary Element Method in Engineering. A complete course.* London: McGraw-Hill Book Company.

Brooks, D.H., Ahmad, G.F., MacLeod, R.S., & Maratos, G.M. 1999. Inverse Electrocardiography by Simultaneous Imposition of Multiple Constraints. *IEEE Transactions on Biomedical Engineering*, **46**, 3–17.

Buchner, Helmut, Knoll, Gunter, Fuchs, Manfred, Rienäcker, Adrian, Beckmann, Rainer, Wagner, Michael, Silny, Jiri, & Pesch, Jörg. 1997. Inverse Localization of Electric Dipole Current Sources in Finite Element Models of the Human Head. *Electroencephalography and Clinical Neurophysiology*, **102**, 267–278.

Chan, Tony F. 1984. Deflated Decomposition of Solutions of nearly Singular Systems. *SIAM Journal of Numerical Analysis*, **21**, 738–754.

Chari, M.V.K., & Silvester, P.P. 1980. *Finite Elements in Electrical and Magnetic Field Problems.* John Wiley & Sons.

Cuffin, B. Neil, & Cohen, David. 1979. Comparison of the Magnetoencephalogram and Electroencephalogram. *Electroencephalography and Clinical Neurophysiology*, **47**, 132–146.

Dale, Anders M., & Sereno, Martin I. 1993. Improved Localisation of Cortical Activity by Combining EEG and MEG with MRI Cortical Surface Reconstuction: a Linear Approach. *Journal of Cognitive Neuroscience*, **5**, 162–176.

Dale, Anders M., Fischl, Bruce, & Sereno, Martin I. 1999. Cortical Surface-Based Analysis I: Segmentation and Surface Reconstruction. *NeuroImage*, **9**(2), 179–194.

Dale, Anders M., Liu, Arthur K., Fischl, Bruce R., Buckner, Randy L., Belliveau, John W., Lewine, Jeffrey D., & Halgren, Eric. 2000. Dynamic Statistical Parametric Mapping: Combining fMRI and MEG for High-Resolution Imaging of Cortical Activity. *Neurone*, **26**(April), 55–67.

de Munck, J. C. 1992. A Linear Discretization of the Volume Conductor Boundary Integral Equation using Analytically Integrated Elements. *IEEE Transactions on Biomedical Engineering*, **39**, 986–990.

Dempster, A.P., Laird, N.M., & Rubin, D.B. 1977. Maximum Likelihood Estimation from Incomplete Data via the EM Algorithm. *Journal of the Royal Statistical Society, Series B*, **39**, 1–38.

Engl, H.W., & Grever, W. 1994. Using the L-curve for termining Optimal Regularization Parameters. *Numerische Mathematik*, **69**, 25–31.

Ferguson, A. Stewart, & Stroink, Gerhard. 1994. The Potential Generated by Current Sources Located in an Insulated Rectangular Volume Conductor. *Journal of Applied Physics*, **76**, 7671–7676.

Ferguson, A.S., & Stroink, G. 1997. Factors Affecting the Accuracy of the Boundary Element Method in the Forward Problem — I: Calculating Surface Potential. *IEEE Transactions on Biomedical Engineering*, **44**, 1139–1155.

Fischl, Bruce, & Dale, Anders M. 2000. Mesuring the Thickness of the Human Cerebral Cortex from Magnetic Resonance Images. *Proceedings of the National Academy of Sciences USA*, **97**, 11050–11055.

Fischl, Bruce, Sereno, Martin I., & Dale, Anders M. 1999. Cortical Surface-Based Analysis II : Inflation, Flattening, and a Surface-Based Coordinate System. *NeuroImage*, **9**(2), 195–207.

Frackowiak, Richard, Friston, Karl J., Frith, Chris D., Dolan, Raymond, & Mazziotta, John C. 1997. *Human Brain Function*. Academic Press.

Friston, Karl J., & Worsley, Keith J. 1995. Analysis of fMRI Time-Series Revisited — Again. *NeuroImage*, **2**, 173–181.

Friston, Karl J., Ashburner, John, Poline, Jean-Baptiste, Frith, Christopher D., Heather, J.D., & Frackowiak, Richard S.J. 1995a. Spatial Registration and Normalization of Images. *Human Brain Mapping*, **2**, 165–189.

Friston, Karl J., Holmes, Andrew P., Worsley, Keith J., Poline, Jean-Baptiste, Frith, Christopher D., & Frackowiak, Richard S.J. 1995b. Statistical Parametric Maps in Functional Imaging : A General Linear Approach. *Human Brain Mapping*, **2**, 189–210.

Fuchs, Manfred, Wagner, Michael, Wischmann, Hans-Aloys, Köhler, Thomas, Tiessen, Annette, Drenckhahn, Ralf, & Buchner, Helmut. 1998. Improving Source Reconstructions by Combining Bioelectric and Biomagnetic Data. *Electroencephalography and Clinical Neurophysiology*, **107**, 93–111.

Gençer, Nevzat G., & Williamson, Samuel J. 1998. Differential Characterization of Neural Sources with the Bimodal Truncated SVD Pseudo-Inverse for EEG and MEG Measurements. *IEEE Transactions on Biomedical Engineering*, **45**(7), 827–837.

Geselowitz, David B. 1967. On Bioelectric Potentials in an Inhomogeneous Volume Conductor. *Biophysical Journal*, **7**, 1–11.

Goebel, Rainer, & Max Planck Society. 2000. *BrainVoyager 2000, Version 4.2*. http://www.brainvoyager.de.

Grave de Peralta Menendez, Rolando, & Gonzalez Andino, Sara. 1998. A Critical Analysis of Linear Inverse Solutions to the Neuroelectromagnetic Inverse Problem. *IEEE Transactions on Biomedical Engineering*, **45**(4), 440–448.

Grave de Peralta Menendez, Rolando, & Gonzalez Andino, Sara. 1999. Backus and Gilbert Method for Vector Fields. *Human Brain Mapping*, **7**, 161–165.

Grave de Peralta Menendez, Rolando, Hauk, Olaf, Gonzalez Andino, Sara, Vogt, Hermann, & Michel, Christophe. 1997. Linear Inverse Solutions with Optimal Resolution Kernels Applied to Electromagnetic Tomography. *Human Brain Mapping*, **5**, 454–467.

Greenblatt, Richard E. 1993. Probabilistic Reconstruction of Multiple Sources in the Bioelectromagnetic Inverse Problem. *Inverse Problems*, **9**, 271–284.

Hämäläinen, Matti S., & Ilmoniemi, Riisto J. 1994. Interpreting Magnetic Fields of the Brain : Minimum Norm Estimates. *Medical and Biological Engineering and Computing*, **32**, 35–42.

Hämäläinen, Matti S., & Sarvas, Jukka. 1989. Realistic Conductivity Geometry Model of the Human Head for Interpretation of Neuromagnetic Data. *IEEE Transactions on Biomedical Engineering*, **36**, 165–171.

Hämäläinen, Matti S., Hari, Riita, Ilmoniemi, Riisto J., Knuutila, Jukka, & Lounasmaa, Olli V. 1993. Magentoencephalography — Theory, Instrumentation, and Applications to Noninvasive Studies of the Working Human Brain. *Reviews of Modern Physics*, **65**(2), 413–497.

Hansen, P.C. 1992. Analysis of Discrete Ill-Posed Problems by Means of the L-Curve. *SIAM review*, **34**, 561–580.

Harville, D.A. 1974. Bayesian Inference for Variance Components using only Error Contrasts. *Biometrika*, **61**, 383–385.

Harville, D.A. 1976. Extension of the Gauss-Markov Theorem to Include the Estimation of Random Effects. *The Annals of Statistics*, **4**, 384–395.

Harville, D.A. 1977. Maximum Likelihood Approaches to Variance Component Estimation and to Related Problems. *Journal of the American Statistical Association*, **72**(June), 320–338.

He, Sailing. 1998. Frequency Series Expansion of an Explicit Solution for a Dipole inside a Conducting Sphere at Low Frequency. *IEEE Transactions on Biomedical Engineering*, **45**, 1249–1258.

Heller, Leon. 1990. Computation of the Return Current in Encephalography : the Auto Solid Angle. *SPIE Digital Image Synthesis and Inverse Optics*, **1351**, 376–390.

Huang, M., Aaron, R., & Shiffman, C. A. 1997. Maximum Entropy Method for Magnetoencephalography. *IEEE Transactions on Biomedical Engineering*, **44**(1), 98–102.

Huang, M., Aine, C. J., Best, S. Supek E., Ranken, D., & Flynn, E. R. 1998. Multi-Start Downhill Simplex Method for Spatio-Temporal Source Localization in Magnetoencephalography. *Electroencephalography and Clinical Neurophysiology*, **108**, 32–44.

Huiskamp, Geertjan, Vroeijenstijn, Maurice, van Dijk, René, Wieneke, George, & van Huffelen, Alexander C. 1999. The Need for Correct Realistic Geometry in the Inverse EEG Problem. *IEEE Transactions on Biomedical Engineering*, **46**(11), 1281–1287.

Jones, D.S. 1979. *Elementary Information Theory*. Oxford: Carendon Press.

Kiebel, Stefan J., Goebel, Rainer, & Friston, Karl J. 2000. Anatomically Informed Basis Functions. *NeuroImage*, **11**, 656–667.

Kleinermann, F., Avis, N.J., & Alhargan, F.A. 2000. Analytical Solution to the Three-Dimensional Electrical Forward Problem for a Circular Cylinder. *Inverse Problems*, **16**, 461–468.

Klepfer, Ruthe Nicholson, Johnson, Chritopher R., & Macleod, Robert S. 1997. The Effect of Inhomogeneities and Anisotropies on Electrocardiographic Fields : a 3-D Finite-Element Study. *IEEE Transactions on Biomedical Engineering*, **44**(8), 706–719.

Lambin, Ph., & Troquet, J. 1983. Complete Calculation of the Electric Potential Produced by a Pair of Current Source and Sink Energizing a Circular Finite-Length Cylinder. *Journal of Applied Physics*, **54**, 4174–7184.

Liu, Arthur K., Belliveau, John W., & Dale, Anders M. 1998. Spatiotemporal Imaging of Human Brain Activity using Functional MRI Constrained Magentoencephalography Data : Monte Carlo Simulations. *Proceedings of the National Academy of Sciences USA*, **95**(July), 8945–8950.

Lynn, M. Stuart, & Timlake, William P. 1968a. The Numerical Solution of Singular Integral Equation of Potential Theory. *Numerische Mathematik*, **11**, 77–98.

Lynn, M. Stuart, & Timlake, William P. 1968b. The Use of Multiple Deflations in the Numerical Solution of Singular Systems of Equations, with Application to Potential Theory. *SIAM Journal of Numerical Analysis*, **5**, 303–322.

Malmivuo, Jaakko, & Plonsey, Robert. 1995. *Bioelectromagnetism : Principles and Applications of Bioelectric and Biomagnetic Fields.* Oxford University press.

Marin, Gildas, Guerin, Christophe, Baillet, Sylvain, Garnero, Line, & Meunier, Gérard. 1998. Influence of Skull Anisotropy for the Forward and Inverse Problem in EEG : Simulations Studies using FEM on Realistic Head Models. *Human Brain Mapping*, **6**, 250–269.

Meijs, Jan W. H., Weier, Onno W., Peters, Maria J., & van Oosterom, Adriaan. 1989. On the Numerical Accuracy of the Boundary Element Method. *IEEE Transactions on Biomedical Engineering*, **36**, 1038–1049.

Miltner, W., Braun, C., Johnson, R., Simpson, G.V., & Ruchkni, D.S. 1994. A Test of Brain Electrical Source Analysis (BESA) : a Simulation Study. *Electroencephalography and Clinical Neurophysiology*, **91**, 295–310.

Mosher, John C., Lewis, Paul S., & Leahy, Richard M. 1992. Multiple Dipole Modelling and Localization from Spatio-Temporal MEG Data. *IEEE Transactions on Biomedical Engineering*, **39**(6), 541–557.

Mosher, John C., Leahy, Richard M., & Lewis, Paul S. 1999. EEG and MEG : Forward Solutions for Inverse Methods. *IEEE Transactions on Biomedical Engineering*, **46**, 245–259.

Nunez, P. L. 1981. *Electric Fields of the Brain : the Neurophysics of EEG.* New York: Oxford University Press.

Opitz, B., Mecklinger, A., Friederici, A.D., & von Cramon, D.Y. 1999. The Functional Neuroanatomy of Novelty Processing : Integrating ERP and fMRI Results. *Cerebral Cortex*, **9**, 379–391.

Pascual-Marqui, Roberto D. 1995. Reply to Comments by M. Hämäläinen, R. Ilmoniemi and P. Nunez. *Pages 16–28 of:* Skrandies, W. (ed), *Source Localization : Continuing Discussion of the Inverse Prolem.* ISBET Newsletter, no. 6.

Pascual-Marqui, Roberto D. 1998. *Low Resolution Brain Electromagnetic Tomography (LORETA).* http://www.unizh.ch/keyinst/NewLORETA/LORETA01.htm.

Pascual-Marqui, Roberto D. 1999. Review of Methods for Solving the EEG Inverse Problem. *International Journal of Bioelectromagnetism*, **1**(1), 75–86.

Pascual-Marqui, Roberto D., Michel, Christophe M., & Lehmann, Dietrich. 1994. Low Resolution Electromagnetic Tomography : a New Method for Localizing Electrical Activity in the Brain. *International Journal of Psychophysiology*, **18**, 49–65.

Patterson, H.D., & Thompson, R. 1971. Recovery of Inter-Block Information when Block Sizes are Unequal. *Biometrika*, **58**, 545–554.

Perona, P., & Malik, J. 1990. Scale-Space and Edge Detection using Anisotropic Diffusion. *IEEE Transactions on Pattern Analysis and Machine Intelligence*, **12**, 629–639.

Picton, T.W., Bentin, S., Berg, P., Donchin, E., Johnson, S.A. Hillyard R., Miller, G.A., Ritter, W., Ruchkin, D.S., Rugg, M.D., & Taylor, M.J. 2000. Guidelines for Using Human Event-Related Potentials to Study Cognition : Recording Standards and Publication Criteria. *Psychophysiology*, **37**, 127–152.

Rabiner, Lawrence R., & Gold, Bernard. 1975. *Theory and Application of Digital Signal Processing*. London: Prentice-Hall.

Ramo, Simon, Whinnery, John R., & van Duzer, Theodore. 1984. *Fields and Waves in Communication Electronics*. John Wiley & Sons.

Rao, C. Radhakrishna, & Mitra, Sujit Kumar. 1973. Theory and Application of Constrained Inverse of Matrices. *SIAM Journal of Applied Mathematics*, **24**(4), 473–488.

Rosenfeld, Moshe, Tanami, Ronen, & Abboud, Shimon. 1996. Numerical Solution of the Potential Due to Dipole Sources in Volume Conductors with Arbitrary Geometry and Conductivity. *IEEE Transactions on Biomedical Engineering*, **43**(7), 679–689.

Rugg, Michael D. 1998. Convergent Approaches to Electrophysiological and Hæmodynamics Investigations of Memory. *Human Brain Mapping*, **6**, 394–398.

Rugg, Michael D. 1999. Functional Neuroimaging in Cognitive Neuroscience. *Chap. 2, pages 15–36 of:* Brown, Colin M., & Hagoort, Peter (eds), *The Neurocognition of Language*. Oxford: Oxford University Press.

Rugg, Michael D., & Coles, Michael G.H. 1995. *Electrophysiology of Mind : Event Related Brain Potentials and Cognition*. Oxford Psychology Series, no. 25. Oxford University Press.

Saleheen, Hasan I., & Ng, Kwong T. 1997. New Finite Difference Formulations for General Inhomogeneous Anisotropic Bioelectric Problems. *IEEE Transactions on Biomedical Engineering*, **44**(9), 800–809.

Saleheen, Hasan I., & Ng, Kwong T. 1998. A new Three-Dimensional Finite-Difference Bidomain Formulation for Inhomogeneous Anisotropic Cardiac Tissues. *IEEE Transactions on Biomedical Engineering*, **45**(1), 15–25.

Sarvas, Jukka. 1987. Basic Mathematical and Electromagnetic Concepts of the Biomagnetic Inverse Problem. *Physics in Medicine and Biology*, **32**, 11–22.

Scherg, Michael, & Ebersole, J.S. 1994. Brain source Imaging of Focal and Multifocal Epileptiform EEG Activity. *Clinical Neurophysiology*, **24**, 51–60.

Scherg, Michael, Bast, Thomas, & Berg, Patrick. 1999. Multiple Source Analysis of Interictal Spikes: Goals, Requirements, and Clinical Value. *Journal of Clinical Neurophysiology*, **16**(3), 214–224.

Schlitt, Heidi A., Heller, Leon, Aaron, Ronald, Best, Elaine, & Ranken, Douglas M. 1995. Evaluation of Boundary Element Methods for the EEG Forward Problem: Effect of Linear Interpolation. *IEEE Transactions on Biomedical Engineering*, **42**, 52–58.

Smythe, W. R. 1950. *Static and Dynamic Electricity.* New York: Mac Graw Hill.

Sun, Mingui. 1997. An Efficient Algorithm for Computing Multishell Spherical Volume Conductor Models in EEG Dipole Source Localization. *IEEE Transactions on Biomedical Engineering*, **44**, 1243–1252.

Talairach, Jean, & Tournoux, Pierre. 1988. *Co-Planar Stereotaxic Atlas of the Human Brain.* Stuttgart: Georg Thieme.

Tikhonov, A.N., & Arsenin, V.Y. 1977. *Solutions of Ill-Posed Problems.* New-York: John Wiley.

Uutela, K., Hämäläinen, Matti S., & Somersalo, E. 1999. Visualization of Magnetoencephalographic Data Using Minimum Current Estimates. *NeuroImage*, **10**, 173–180.

van den Broek, S.P., Zhou, H., & Peters, M.J. 1996. Computation of Neuromagnetic Fields using Finite-Element Method and Biot-Savart Law. *Medical & Biological Enineering & Computing*, **34**, 21–26.

van Essen, D.C., & Drury, H.A. 1997. Structural and Functional Analyses of Human Cerebral Cortex Using a Surface-Based Atlas. *Journal of Neuroscience*, **17**, 7079–7102.

van Oosterom, A., & Strackee, J. 1983. The Solid Angle of a Plane Triangle. *IEEE Transactions on Biomedical Engineering*, **30**, 125–126.

Varah, J.M. 1979. A Practical Examination of some Numerical Methods for Linear Discrete Ill-Posed Problems. *SIAM review*, **21**, 100–111.

Vladimirov, Vasiliy S. 1971. *Equations of Mathematical Physics.* New York: Marcel Dekker.

von Helmholtz, Hermann L.F. 1853. Ueber einige Gesetze der Vertheilung elektrischer Ströme in köperlichen Leitern mit Anwendung auf die thierisch-elektrischen Versuche. *Annalen der Physik und Chemie*, **89**, 211–233, 354–377.

Wellcome Department of Cognitive Neurology. 1999. *Statistical Parametric Mapping, SPM'99.* http://www.fil.ion.ucl.ac.uk/spm/spm99.html.

Worsley, Keith J. 1994. Local Maxima and the Expected Euler Characteristic of Excursion Sets of χ^2, F and t Fields. *Advances in Applied Probability*, **26**, 13–42.